UNIVERSIDAD DE CONCEPCIÓN

FACULTAD DE INGENIERÍA

Doctorado en Energías

IMPACTO DE LA VARIABILIDAD CLIMÁTICA Y EL CAMBIO CLIMÁTICO SOBRE EL POTENCIAL EÓLICO EN AMÉRICA DEL SUR

Tesis para optar al grado de Doctor en Energías

Por: Lic. Ovidio Llompart Blanco

Profesor Guía: Dr. Héctor H. Sepúlveda Allende

Profesor Co-guía: Dr. Martín Jacques Coper

Concepción, Chile. Noviembre de 2025

Universidad de Concepción
Dirección de Postgrado

La Tesis de Doctorado en Energías titulada “Impacto de la variabilidad climática y el cambio climático sobre el potencial eólico en América del Sur”, del Sr. Ovidio Llompart Blanco y realizada en la Facultad de Ingeniería, Universidad de Concepción, ha sido aprobada por la siguiente Comisión de Evaluación:

Dr. Héctor H. Sepúlveda
Profesor Guía
Universidad de Concepción

Dr. Martín Jacques Coper
Profesor Co-guía
Universidad de Concepción

Dr. Mauricio Aguayo
Miembro Comité de Evaluación
Universidad de Concepción

Dr. Octavio Rojas
Miembro Comité de Evaluación
Universidad de Concepción

Dr. Cristian Mattar
Miembro Comité de Evaluación (Evaluador Externo)
Universidad de Chile

Dr. Alejandro Karelovic
Director Programa de Doctorado en Energías
Universidad de Concepción

A mi mamá, Magaly Blanco Quesada,

por todo su esfuerzo y dedicación.

AGRADECIMIENTOS

Agradezco al Dr. Andrés Sepúlveda, por haberme aceptado como su alumno y guiarme durante este proceso de investigación. Ha sido un camino largo y difícil pero su guía certera me ha permitido aprender y crecer como profesional de las ciencias. Muchas gracias por su cercanía y apoyo constante semana tras semana durante estos tres años.

Agradezco al Dr. Martín Jacques Coper, quien desde el primer momento ha sido una parte fundamental en este proyecto. Contar con su apoyo ha sido muy enriquecedor y esencial para juntar todas las piezas del rompecabezas. Muchas gracias por las horas de dedicación y por compartir sus conocimientos en el fascinante mundo de la Meteorología.

A la Dra. Marieta Hernández, mi amiga que me dio el primer impulso para empezar este doctorado y que ha sido mi compañera de estudios, de trámites y de tantos momentos de incertidumbre y de alegrías. Me alegro mucho por haber compartido este viaje contigo, sin duda alguna tu ejemplo y tu apoyo han sido fundamentales para mí.

A Daniel, quien me ha acompañado durante todo este tiempo en las buenas y en las malas y que ha sido una parte muy importante para poder llegar hasta aquí. Muchas gracias por tanta paciencia y por estar siempre presente alegrando cada momento.

A Laura, mi amiga incondicional, por su ayuda desde el primer momento para comenzar el doctorado y poder llegar a Chile en tiempos tan difíciles.

A mi amigo Yosvany, que me compartió los primeros códigos de programación para poner en marcha toda la maquinaria, y que ha sido siempre un gran apoyo.

A mi tía Lilliam, quien fue una parte fundamental en mi formación como meteorólogo, el primer escalón para poder llegar hasta donde me encuentro hoy.

A mis amigos Amanda, Yilian, Daily, Alejandro, Carlitos, Juan Carlos, Maibelín y Lázaro, muchas gracias a todos por su ayuda y por hacer que, aunque estemos lejos, me sienta más cerca de casa.

Finalmente, agradezco a la Agencia Nacional de Investigación y Desarrollo [ANID 21210309] y al Centro de Ciencia del Clima y la Resiliencia (CR)2 [FONDAP/ANID 1523A0002] por el financiamiento de este proyecto.

ABREVIATURAS

AO: Arctic Oscillation
AAO: Antarctic Oscillation
AEP: Annual Energy Production
CRM: Cumulative Raw Moment
EA: Eastern Atlantic Pattern
ENSO: El Niño/Southern Oscillation
EOF: Empirical Orthogonal Functions
GCM: Global Climate Model
NAO: North Atlantic Oscillation
ONI: Oceanic Niño Index
PAT: Patagonia - Antarctica Pattern
PC: Principal Component
PDO: Pacific Decadal Oscillation
R: Pearson Correlation Coefficient
RCM: Regional Climate Model
SAA: South Atlantic Anticyclone
SCA: Scandinavian Pattern
SLP: Sea Level Pressure
SPA: South Pacific Anticyclone
SST: Sea Surface Temperature
WPD: Wind Power Density
WS100: Wind Speed at 100 meters

CONTENIDO

ÍNDICE DE TABLAS

II. METODOLOGÍA

III. EVALUACIÓN DE LA VARIABILIDAD DE LA VELOCIDAD DEL VIENTO Y SUS MODULADORES CLIMÁTICOS EN AMÉRICA DEL SUR USANDO SIMULACIONES DE CMIP6 (1980 – 2014)

IV. EVALUACIÓN DE LOS MECANISMOS FUTUROS DE VARIABILIDAD DEL POTENCIAL EÓLICO Y SUS IMPLICACIONES PARA LA GENERACIÓN ENERGÉTICA EN AMÉRICA DEL SUR USANDO SIMULACIONES DE CMIP6

ÍNDICE DE ILUSTRACIONES

I. INTRODUCCIÓN

II. METODOLOGÍA

III. EVALUACIÓN DE LA VARIABILIDAD DE LA VELOCIDAD DEL VIENTO Y SUS MODULADORES CLIMÁTICOS EN AMÉRICA DEL SUR USANDO SIMULACIONES DE CMIP6 (1980 – 2014)

IV. EVALUACIÓN DE LOS MECANISMOS FUTUROS DE VARIABILIDAD DEL POTENCIAL EÓLICO Y SUS IMPLICACIONES PARA LA GENERACIÓN ENERGÉTICA EN AMÉRICA DEL SUR USANDO SIMULACIONES DE CMIP6

RESUMEN

La energía eólica terrestre es una de las fuentes renovables con mayor participación en la matriz energética global. Sin embargo, las redes eléctricas están cada vez más expuestas a su variabilidad intrínseca. Este trabajo evalúa la influencia de diferentes patrones atmosféricos de gran escala sobre la variabilidad de la velocidad viento a 100m (WS100) y la densidad del potencial eólico (WPD) en América del Sur, y su impacto sobre la producción anual de energía (AEP) en el futuro. Se utilizaron datos de 14 modelos climáticos globales de CMIP6 y de reanálisis del ERA5 para el período histórico 1980 - 2014 y los períodos futuros 2030 – 2069 y 2070 – 2099 bajo el escenario SSP2-4.5. Se aplicó un análisis de funciones ortogonales empíricas (EOF) sobre WS100 en regiones seleccionadas y se calcularon las correlaciones con los principales patrones atmosféricos que influyen sobre el clima de la región. Se calcularon las variaciones de WPD con respecto al período histórico y se estimaron las diferencias futuras de AEP en las regiones más impactadas.

Según nuestros resultados los principales cambios en WPD y AEP se concentran en dos regiones fundamentales: el nordeste de Brasil y la Patagonia. Encontramos que el Anticiclón del Atlántico Sur (SAA) es el principal modulador de WS100 sobre el nordeste de Brasil dado por una correlación positiva, por lo que el aumento en la intensidad del SAA provoca un aumento de WS100 en dicha región. Por otra parte, descubrimos un patrón al que denominamos Patrón Patagonia - Antártica (PAT), y que constituye el principal modulador de WS100 sobre la Patagonia, dado por una correlación negativa, por lo que la fase positiva del PAT provoca una disminución de WS100.

Se prevé un aumento significativo de WPD de más del 30% para 2099 en el nordeste de Brasil, asociado principalmente a una tendencia positiva del SAA, mientras que se proyecta una disminución de hasta un -20% en la Patagonia asociada a una tendencia positiva en el PAT. Estos cambios equivalen a un aumento de AEP de hasta un 18% para 2069 y un 37,6% para 2099 en el nordeste de Brasil, mientras que en la Patagonia se proyecta una disminución de hasta un -33,6% para 2069 y un -33,8% para 2099. La principal contribución de este trabajo es que permite comprender los mecanismos atmosféricos que influyen en las variaciones a largo plazo de WPD y AEP. Esto es de gran relevancia para la industria eólica en la planificación del sistema y la evaluación de riesgos en proyectos eólicos actuales y futuros en América del Sur.

ABSTRACT

On-shore wind energy is one of the renewable sources with the largest share in the global energy mix. However, electricity grids are increasingly exposed to their intrinsic variability. This work evaluates the influence of different large-scale atmospheric patterns on the variability of 100m wind speed (WS100) and wind power density (WPD) in South America, and their impact on future annual energy production (AEP). Data from 14 CMIP6 global climate models and ERA5 reanalysis were used for the historical period 1980–2014 and the future periods 2030–2069 and 2070–2099 under the SSP2-4.5 scenario. An empirical orthogonal function (EOF) analysis was applied to WS100 in selected regions, and correlations with the main atmospheric patterns influencing the region climate were calculated. WPD variations relating to the historical period were calculated, and future AEP differences were estimated in the most impacted regions.

According to our results, the main changes in WPD and AEP are concentrated in two key regions: northeast Brazil and Patagonia. We found that the South Atlantic Anticyclone (SAA) is the main modulator of WS100 over northeast Brazil, with a direct relationship, such that an increase in SAA intensity causes an increase in WS100 and vice versa. We discovered a pattern centered in the Drake Passage, which we named the Patagonia-Antarctica (PAT) pattern, which constitutes the main modulator of WS100 over Patagonia. The positive phase of the PAT causes a decrease in WS100 and vice versa.

A significant increase in WPD of more than 30% is projected by 2099 in northeast Brazil, mainly associated with a positive SAA trend, while a decrease of up to -20% is projected in Patagonia associated with a positive PAT trend. These changes are equivalent to an AEP increase up to 18% by 2069 and 37.6% by 2099 in Northeast Brazil, while in Patagonia a decrease up to -33.6% by 2069 and -33.8% by 2099 is projected. The main contribution of this work is that it allows an understanding of the atmospheric mechanisms influencing long-term variations in WPD and AEP. This is of great relevance to the wind industry in system planning and risk assessment for current and future wind projects in South America.

ESTRUCTURA DE LA TESIS

A continuación, el cuerpo de la tesis está estructurado de la siguiente forma:

Capítulo I. Introducción

En este capítulo se aborda el contexto científico y la relevancia del tema, se plantea el problema de investigación, la hipótesis y los objetivos específicos propuestos para darle solución.

Capítulo II. Metodología

En este capítulo se describen las principales características físico-geográficas del área de estudio, los datos utilizados y la metodología de investigación.

Capítulo III. Evaluación de la variabilidad de la velocidad del viento y sus moduladores climáticos en América del Sur usando simulaciones de CMIP6 (1980 – 2014)

En este capítulo se muestran y discuten los resultados correspondientes al objetivo específico 1.

Capítulo IV. Evaluación de los mecanismos futuros de variabilidad del potencial eólico y sus implicaciones para la generación energética en América del Sur usando simulaciones de CMIP6

En este capítulo se muestran y discuten los resultados correspondientes a los objetivos específicos 2 y 3.

Capítulo V. Discusión general

En este capítulo se discuten de forma general los resultados encontrados en la investigación y el cumplimiento de la hipótesis planteada.

Capítulo VI. Conclusiones generales

En este capítulo se presenta una síntesis de los principales resultados de la investigación en forma de conclusiones de la tesis.

I. INTRODUCCIÓN

I.1. Energía eólica a escala global

La energía eólica terrestre es una tecnología probada y madura con una extensa cadena de suministro global, según la Agencia Internacional de Energía (IEA) (*https://www.iea.org*). Al cierre de 2024 los países con mayor capacidad de energía eólica terrestre instalada son China (482,646 MW), Estados Unidos (152,981 MW), Alemania (63,608 MW), la India (48,163 MW) y Brasil (32,959 MW), seguidos de España (31,806 MW) y Francia (23,105 MW), lo cual representa cerca del 80% de la capacidad total instalada a nivel mundial según el reporte de IRENA (2025). En 2023 la generación de energía eólica aumentó en 216 TWh (un 10% más que el año anterior), alcanzando más de 2330 TWh, de acuerdo con la IEA. China fue responsable de dos tercios de las adiciones de capacidad de energía eólica mundial en 2023. Otros países y regiones que están logrando un progreso notable en esta tecnología incluyen: la Unión Europea, con 15 GW añadidos en 2023 y Estados Unidos que incluyó una nueva y generosa financiación para la energía eólica, según informa la IEA.

Para aumentar aún más la participación de la energía eólica en la matriz eléctrica y lograr el Escenario de Emisiones Netas Cero para 2050, propuesto por las Naciones Unidas a partir del Acuerdo de París (*https://www.un.org*), existe una gran necesidad de expansión de la energía eólica (IRENA, 2025). Sin embargo, la variabilidad espaciotemporal del recurso eólico aún complica la evaluación precisa de su disponibilidad (Correia et al., 2017; Jung & Schindler, 2020). Las condiciones atmosféricas y la geografía local intervienen en la generación eólica a través de su papel rector en el comportamiento del viento (Ohba et al., 2016), por lo tanto, de las cargas de las turbinas eólica. La energía eólica que potencialmente puede ser cosechada por los aerogeneradores se estima a través del potencial eólico (Koletsis et al., 2016). Dado que la densidad del potencial eólico depende directamente del cubo de la velocidad del viento (Manwell, 2009), un pequeño cambio en la velocidad del viento puede tener consecuencias sustanciales para la generación eólica (Li et al., 2022; Tian et al., 2019).

El potencial eólico depende en gran medida de la fuerza de los vientos cercanos a la superficie (Li et al., 2022), que están determinados por la variabilidad de la escala sinóptica y los procesos locales (Ohba et al., 2016), como los relacionados con la orografía. Por lo tanto, si el cambio climático altera no sólo el flujo a gran escala (Chen, 2020), sino además las condiciones locales (Jung & Schindler, 2020), también puede alterar los recursos eólicos disponibles y, de hecho, se ha demostrado que esto ya ha sucedido (Davy et al., 2018; Tian et al., 2019). En términos de la operación de un parque eólico y su integración en la red, la variabilidad de la velocidad del viento en una escala de tiempo breve, como la variabilidad diurna o sinóptica, es vital y, por lo tanto, debe pronosticarse (Brayshaw et al., 2011a). Sin embargo, cuando se trata de la selección de los sitios de emplazamiento de los parques eólicos en regiones con gran diversidad geográfica y climática, la variabilidad a escalas espaciotemporales mayores se convierte en una preocupación importante (Alonzo et al., 2017; Tian et al., 2019).

I.2. Influencia del cambio climático sobre el potencial eólico

El cambio climático supone un riesgo potencial para la producción de energía eólica, ya que un clima cambiante puede alterar la dinámica atmosférica y afectar los patrones de viento (Solaun & Cerdá, 2020). Una disminución en la velocidad del viento causará una reducción en la producción de energía, lo cual se refleja de forma más marcada en sitios con bajos valores de velocidad media del viento (Watts et al., 2017). En este contexto, es imperativo evaluar la susceptibilidad del potencial eólico considerando las perspectivas climáticas (Solaun & Cerdá, 2020). Esto tiene importantes implicaciones en la seguridad energética, la mejora de la sostenibilidad global y la economía (Zhang et al., 2019). Durante los últimos años y a raíz de esta problemática, se ha realizado un vasto número de estudios para evaluar el comportamiento del viento en décadas pasadas y analizar su evolución a largo plazo en el contexto del cambio climático.

A escala mundial se proyecta una futura reducción del potencial eólico en muchas regiones del hemisferio norte y se considera posible un aumento en el hemisferio sur con variaciones regionales sustanciales (Karnauskas et al., 2018). De hecho, esta tendencia ha venido manifestándose desde las últimas décadas con una disminución del potencial eólico de más del 30% en América del Norte, Europa y Asia desde 1979 (Tian et al., 2019). Aunque en general diferentes autores consideran que una variación del 10% o más en el potencial eólico es significativa en términos de la producción de energía eólica (De Jong et al., 2019; Tian et al., 2019), diferentes escenarios futuros conducen a una reducción de hasta un 35 % de la densidad del potencial eólico en el norte de Europa continental y el Mediterráneo central (Martinez & Iglesias, 2021). Según Jung & Schindler (2020), el cambio climático conducirá a un probable aumento del potencial eólico en la mayor parte de Brasil, Sudáfrica y Australia Oriental. A escala de las turbinas eólicas también se han realizado numerosos estudios que coinciden con estas proyecciones y que ofrecen beneficios prácticos para la evaluación del potencial eólico bajo los impactos del cambio climático (Gugliani et al., 2021; Islek et al., 2020; D.-Y. Kim et al., 2021; Weber et al., 2018; Wilkie & Galasso, 2020).

Es obvio que existe una tendencia contraria de la velocidad media del viento entre los hemisferios norte y sur. En ambos casos, los cambios en la velocidad media del viento se deben principalmente a cambios en los gradientes de temperatura (Karnauskas et al., 2018): en el hemisferio norte, es principalmente el gradiente de temperatura meridional entre la región polar y las latitudes medias lo que provoca valores altos de velocidad del viento. En el hemisferio sur, es el flujo de aire inducido por el gradiente de temperatura tierra-mar el que conduce a valores altos de velocidad media del viento (Karnauskas et al., 2018). Por un lado, se prevé que el gradiente de temperatura meridional disminuya, porque el cambio climático conduce a un mayor aumento de la temperatura en las regiones polares en comparación con las regiones de latitudes medias. Por otro lado, la velocidad y la cantidad de calentamiento de la tierra y el mar es diferente, lo que resulta en un mayor gradiente de temperatura entre la tierra y el mar en el hemisferio sur (Jung & Schindler, 2020).

Para estudiar el impacto del cambio climático en los sistemas de generación eólica, los modelos climáticos son la única herramienta capaz de producir proyecciones de cambios futuros en respuesta a las emisiones de gases de efecto invernadero (Soares et al., 2017). El Proyecto de Inter-Comparación de Modelos de Clima Acoplados Fase 5 (CMIP5) presentado en 2014 por el Panel Intergubernamental sobre Cambio Climático (IPCC) agrupa modelos climáticos globales (GCMs, del inglés *global climate models*) diseñados para mejorar nuestro conocimiento del cambio climático. Estos modelos adoptan cuatro Trayectorias de Concentración Representativas (RCP, del inglés *Representative Concentration Pathways*) de gases de efecto invernadero para evaluar escenarios futuros: RCP2.6, RCP4.5, RCP6.0 y RCP8.5. El RCP4.5 es un escenario medio, mientras que el RCP8.5 asume un alto crecimiento demográfico y una alta demanda energética sin políticas de cambio climático (Chen, 2020).

Una herramienta común derivada de los GCMs para explorar los impactos del cambio climático en los recursos renovables son los modelos regionales del clima (RCMs, del inglés *Regional Climate Models*). Estos tienen la ventaja sobre los GCMs de que permiten captar los cambios con una mayor resolución espacial y temporal brindando resultados más detallados (Davy et al., 2018). El Experimento Coordinado de Escalado Regional del Clima (CORDEX, por sus siglas en inglés), proporciona un conjunto de RCMs con simulaciones históricas y proyecciones futuras basadas en el CMIP5, y ha sido utilizado en muchos casos para estudiar los efectos del cambio climático regional en el potencial eólico (Chen, 2020; Gao et al., 2019; Solaun & Cerdá, 2020). Sin embargo, debido a su reducido dominio, los RCMs pudieran presentar una limitante cuando se necesita información sobre ciertas áreas geográficas, como las grandes cuencas oceánicas.

El sexto informe de evaluación del IPCC cuenta con nuevos modelos globales CMIP6 de última generación y mayor resolución espacial. Los escenarios actualizados se denominan Trayectorias Socioeconómicas Compartidas (SSP, del inglés *Shared Socioeconomic Pathways*). Los SSP1-2.6, SSP2-4.5, SSP4-6.0 y SSP5-8.5, dan como resultado niveles de forzamiento radiativo en el 2100 similares a los de su predecesor y además se incorporaron otros escenarios que describen desarrollos socioeconómicos alternativos. Debido a que los modelos del CMIP6 son relativamente recientes, existe un menor número de estudios que han utilizados estos modelos globales para investigar el comportamiento futuro del potencial eólico (Akinsanola et al., 2021; Martinez & Iglesias, 2021; Qian & Zhang, 2021) en comparación con los que se basan en modelos del CMIP5. No obstante algunos estudios sobre el recurso eólico basados en el CMIP6 muestran diferencias relevantes y avances en comparación con las del CMIP5 (Carvalho et al., 2021; Wu et al., 2020)

I.3. Influencia de la variabilidad climática sobre el potencial eólico

Independientemente de la variación gradual y progresiva ocasionada por el cambio climático sobre el recurso eólico, la velocidad del viento varía en múltiples escalas de tiempo (Brayshaw et al., 2011a): de segundos a minutos, el ciclo diurno, el ciclo anual y variaciones interanuales que están asociadas a tendencias de largo plazo o de baja frecuencia. Los impactos de estas variaciones en los sistemas eléctricos son diferentes según la escala de tiempo considerada. Las variaciones de alta frecuencia (escala local a mesoescala) tienen implicaciones en los aspectos operativos de los parques eólicos como control de frecuencia, seguimiento de carga, etc. (Brayshaw et al., 2011a), mientras que las variaciones de baja frecuencia (gran escala) son importantes al considerar la evaluación del recurso eólico, la planificación del sistema y el diseño a largo plazo (Alonzo et al., 2017; Bianchi et al., 2022).

La variabilidad climática natural del viento es causada por patrones u oscilaciones que se presentan cada cierto tiempo (meses, años, décadas) en la circulación atmosférica a gran escala y que modulan fuertemente su comportamiento (Ravestein et al., 2018); conocidos también como patrones de teleconexión, puesto que influyen sobre el clima de diferentes regiones del mundo. Las redes eléctricas están cada vez más expuestas a la variabilidad climática debido a la incorporación de energías renovables como la eólica (Ravestein et al., 2018), sin embargo, las oscilaciones climáticas a menudo no se tienen en cuenta en las campañas de medición para la instalación de parques eólicos (Bianchi et al., 2022), aunque numerosas investigaciones han demostrado su influencia en el recurso eólico y la generación de energía.

Alonzo et al. (2017) investigaron una vía para modelar parte de la variabilidad a largo plazo del recurso eólico a partir del conocimiento del estado de la atmósfera a gran escala, con atención en Francia y sus alrededores. El estudio, basado en un análisis de componentes principales sobre la velocidad de viento entre 1979 y 2013 muestra claras relaciones con patrones de teleconexión como la Oscilación del Atlántico Norte (NAO), el Patrón del Atlántico Oriental (EA), el patrón escandinavo (SCA) y el Segundo Patrón Europeo (EU2).

Correia et al. (2017) evaluaron el vínculo entre los patrones de circulación atmosférica a gran escala, el recurso eólico y la producción de energía en Portugal. Los tres modos climáticos bajo el foco son la NAO, el EA y el SCA, que se consideran los patrones de circulación a gran escala más relevantes para el clima del suroeste Europa. El análisis destaca la necesidad de comprender mejor el vínculo entre los principales patrones de circulación atmosférica y la producción de energía renovable, lo que aumenta su previsibilidad en diferentes escalas de tiempo. Garrido-Perez et al. (2020) analizaron en Europa occidental la dependencia del recurso eólico de la circulación atmosférica a gran escala, representada por un conjunto de 8 patrones atmosféricos. El estudio permitió comprender la evolución de episodios específicos regionales con anomalías en la producción de energía eólica.

Li et al. (2022) investigaron los cambios del viento en superficie en el este de China utilizando datos de observación de estaciones meteorológicas y datos de reanálisis de Japón desde 1970 hasta 2019. Los resultados muestran una correlación significativa con el índice del monzón de invierno de Asia oriental, además, con cuatro patrones de circulación atmosférica a gran escala, incluida la Oscilación del Ártico (AO), la NAO, la Oscilación Decadal del Pacífico (PDO) y El Niño/Oscilación del Sur (ENSO). Mendoza et al. (2014) estudiaron los efectos de la PDO en el clima de México durante el periodo 1948-2004, sobre los campos de anomalías de diferentes variables. En el caso del viento se encontraron patrones consistentes con ambas fases de la PDO.

Brayshaw et al. (2011) calcularon la potencia generada por una turbina eólica, al correlacionar la velocidad del viento en sitios específicos en el Reino Unido con un patrón del clima a gran escala como la NAO. Se encontró que las condiciones del viento bajo estos estados pueden producir una diferencia en la potencia media del viento de hasta 10%. Cradden et al. (2017) hallaron una relación entre varias de las características de producción eólica, incluyendo factor de capacidad, rampa y persistencia, y dos patrones atmosféricos a gran escala: la NAO y el EA. Usando una distribución de paneles fotovoltaicos y turbinas eólicas, Ravestein et al. (2018) encontraron que, aunque es probable que el cambio climático tenga un impacto significativo en el futuro de la producción fotovoltaica y eólica en Europa, sus efectos, especialmente para la energía eólica, son superados por el alto y fuertemente variable impacto de las fases de la NAO.

Ohba et al. (2016) analizaron la relación entre los patrones atmosféricos y la generación de energía eólica sobre Japón. El análisis extrajo siete patrones típicos que están vinculados a la ocurrencia frecuente de eventos de rampas de viento, definido como un cambio de potencia del 30% en menos de 6 horas, lo cual resulta significativo en la generación eólica. En este sentido, Dalton et al. (2021) investigaron el vínculo entre las rampas de viento y los patrones de circulación atmosférica en. Según el estudio, que considera un parque eólico en Sudáfrica, la variabilidad de la potencia media difiere significativamente en función de la circulación atmosférica. Los resultados de estos estudios sugieren que la clasificación detallada de los patrones de circulación atmosférica y su vínculo con el comportamiento del viento puede ser una herramienta útil para estimar la variabilidad en la generación de energía eólica futura.

I.4. Potencial eólico y variabilidad climática en América del Sur

En América del Sur la generación eólica terrestre ha experimentado un aumento vertiginoso en algunos de sus países durante la última década, cuadruplicando su capacidad instalada (Figura 1b). Los principales productores (Figura 1a) son: Brasil (32,959 MW), seguido de Chile (4,807 MW) y Argentina (4,320 MW), luego se encuentran Uruguay (1,524 MW) y Perú (1,151 MW). Estos cinco países representan el 99.3% de la capacidad instalada total en la región al cierre del año 2024, la cual tuvo un crecimiento del 11.9% con respecto al año anterior (IRENA, 2025).

Según las proyecciones futuras se espera que el potencial eólico en América del Sur aumente sustancialmente en la mayor parte de Brasil, y en algunas ubicaciones la generación eólica podría aumentar incluso en más del 40% para 2080 (De Jong et al., 2019). Este resultado coincide con el estudio de Karnauskas et al. (2018) que señala un aumento en la energía eólica para el este de Brasil del 21% para 2050 y del 42% para 2100. De acuerdo con estos resultados y las proyecciones a nivel global cabe la posibilidad de que en el resto de América del Sur ocurran variaciones de magnitud similar (al menos ±30%) en el futuro del potencial eólico, aunque con marcadas variaciones regionales producto de la gran diversidad geográfica del territorio y la influencia de diferentes moduladores de la variabilidad climática.

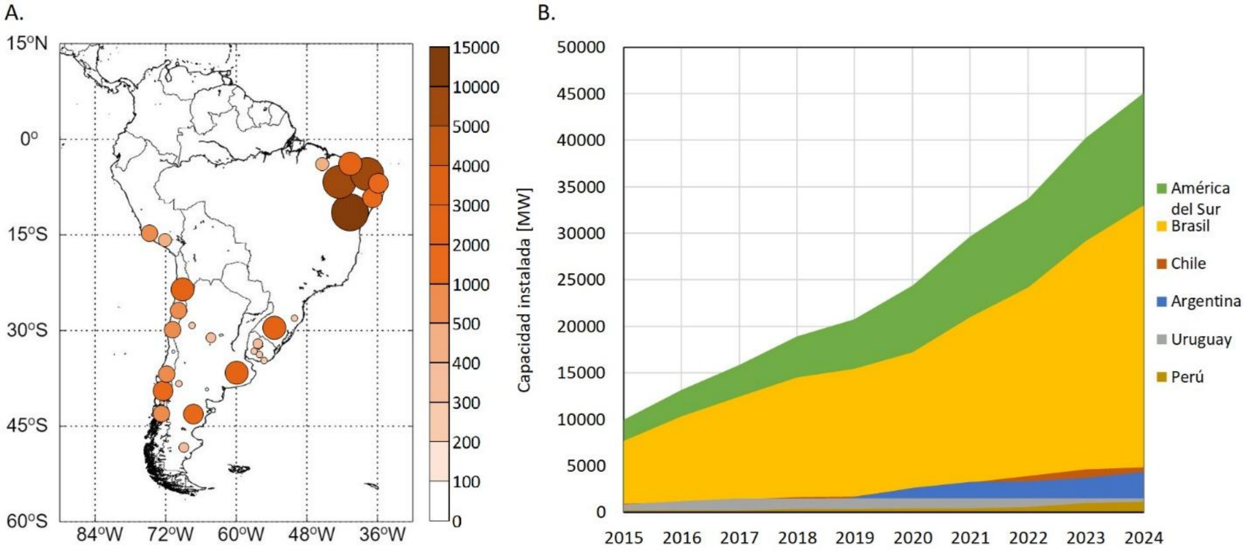

Figura 1. a) Capacidad instalada de energía eólica terrestre en América del Sur, distribuida según la división regional de cada país. Elaborado según datos tomados de *www.thewindpower.net*. b) Evolución de la capacidad eólica terrestre instalada en América del Sur durante la década 2015 – 2024. Elaborado según los datos del informe de IRENA (2025).

Según diferentes técnicas de análisis en América del Sur parece que la mayor parte de la variación de baja frecuencia reside en unos pocos modos globales: ENSO, PDO y la Oscilación Antártica (AAO) (Garreaud et al., 2009). El ENSO es un fenómeno acoplado océano-atmósfera con raíces en el Pacífico tropical, caracterizado por fluctuaciones irregulares entre sus fases cálidas (El Niño) y frías (La Niña) con una periodicidad de entre 2 y 7 años (Garreaud et al., 2009). El gradiente zonal de temperatura superficial del mar (SST) ecuatorial impulsa los vientos del este sobre el Pacífico tropical, y estos, a su vez, crean una SST fría sobre el Pacífico oriental, lo que resulta en el fortalecimiento del gradiente de SST (Bjerknes, 1969).

La PDO a menudo se describe como un fenómeno similar al ENSO, porque las huellas climáticas espaciales de ambos patrones tienen gran parecido. Las causas de la PDO y sus vínculos con el ENSO aún no se comprenden completamente, especialmente en el caso del viento (Garreaud et al., 2009).

La AAO es el patrón principal de variabilidad de la circulación troposférica al sur de los 20°S y se caracteriza por anomalías de presión de un signo centradas en la Antártida y anomalías del signo opuesto en una banda circuglobal entre 40°S y 50°S (Thompson & Wallace, 2000). La fase positiva de la AAO se asocia con una disminución (aumento) de la presión superficial y de las alturas geopotenciales sobre la Antártida (latitudes medias), así como con un fortalecimiento y desplazamiento hacia los polos de los vientos del oeste. Durante la fase negativa prevalecen condiciones opuestas (Garreaud et al., 2009).

Según Bianchi et al. (2017) tanto el ENSO como la AAO muestran señales relevantes sobre la velocidad del viento en la región austral de América del Sur. En un estudio más reciente, Bianchi et al. (2022) encontraron que el recurso eólico es más sensible a la AAO, con una relación negativa y más fuerte durante la primavera y el verano. En el caso de Chile, Watts et al. (2017) hallaron que la fase cálida del ENSO, reduce la velocidad del viento y la producción de energía eólica en la mayoría de los sitios del centro-norte de Chile, sin embargo, la magnitud y a veces el signo dependen del sitio analizado y del mes en que ocurren los fenómenos.

Por otro lado, tanto el Anticiclón del Pacífico Sur (SPA) como el Anticiclón del Atlántico Sur (SAA) son centros de alta presión semipermanentes con un ciclo anual marcado que alcanza su máximo durante el invierno austral y modula fuertemente el clima de Sudamérica (Ancapichún & Garcés-Vargas, 2015; Cabos et al., 2017). El SPA se centra sobre la cuenca del Pacífico Suroriental e influye principalmente en la costa chilena, con un flujo predominante del suroeste (Ancapichún & Garcés-Vargas, 2015).

El SAA afecta la cuenca tropical del Atlántico Sur, y su ciclo estacional está controlado principalmente por fuentes de calor convectivo sobre Sudamérica y el sur de África, y por la interacción entre la orografía con los vientos alisios del este y los vientos del oeste de latitudes medias (Miyasaka & Nakamura, 2010; Rodwell & Hoskins, 2001). Estos mecanismos fundamentales dan lugar a un SAA notablemente más intenso durante el invierno austral que durante el verano (Cabos et al., 2017).

I.5. Problema de investigación y novedad científica

Como muestran diferentes investigaciones, se han desarrollado estudios que reflejan un comportamiento espaciotemporal relativamente robusto en los cambios futuros de la velocidad del viento y el potencial eólico, basados en diversos escenarios de emisión y simulaciones con distintas resoluciones espaciales. Los resultados de dichas investigaciones muestran las regiones que pueden beneficiarse o ser impactadas negativamente por el cambio climático global. Sin embargo, la mayoría de estos trabajos no son concluyentes sobre las causas de tales cambios y la creciente variabilidad en la velocidad del viento y el potencial eólico, por lo que se deben realizar estudios adicionales para explorar los mecanismos que influyen en la variabilidad del recurso eólico.

En muchos casos los efectos del cambio climático son superados por el fuerte impacto de la variabilidad climática, por lo que son dos aspectos importantes a tener en cuenta. La mayoría de las investigaciones que buscan estudiar las relaciones existentes entre el comportamiento del potencial eólico y diferentes patrones atmosféricos se han desarrollado en Europa, Asia y Norteamérica. En el caso de América del Sur los trabajos que buscan explorar las relaciones con los patrones atmosféricos se han centrado en otras variables como la precipitación o la temperatura. Sin embargo, respecto al recurso eólico son pocos los análisis realizados en este sentido, los mismos se basan en casos de estudio puntuales y por lo general sólo analizan períodos de tiempo históricos.

Resulta evidente entonces que en la región de América del Sur aún existe una brecha entre los cambios futuros en el potencial eólico y los mecanismos atmosféricos que provocan tales cambios. Es por ello que la presente investigación resulta novedosa, puesto que describe el comportamiento del potencial eólico y la generación de energía en el futuro bajo los efectos del cambio climático, y además permite comprender cuáles son los patrones atmosféricos que causan ese comportamiento. Los resultados de este trabajo representan un valioso aporte al conocimiento científico y permiten un mejor enfoque en el manejo de los recursos eólicos para aumentar aún más su participación en la matriz energética regional y la transición hacia las energías renovables.

I.6. Hipótesis y objetivos

A partir del problema de investigación se planteó la siguiente hipótesis:

La variabilidad del viento en América del Sur ocasionada por los moduladores climáticos de gran escala SPA, SAA, ENSO y AAO tendrá un impacto de al menos ±30% en el futuro potencial eólico terrestre de la región bajo los efectos del cambio climático considerando el escenario SSP2-4.5.

Para dar solución al problema, el objetivo principal de la investigación es, por tanto:

- Analizar el impacto de diferentes moduladores climáticos sobre el potencial eólico terrestre en América del Sur, bajo la influencia del cambio climático.

Los objetivos específicos son:

1. Establecer las relaciones entre el comportamiento de la velocidad del viento y los moduladores climáticos SPA, SAA, ENSO y AAO durante el período histórico 1980-2014.
2. Determinar las relaciones futuras entre la velocidad del viento y los moduladores climáticos en las regiones con mayor variación del potencial eólico durante los períodos 2030 – 2069 y 2070 – 2099.
3. Estimar las variaciones futuras de la generación de energía eólica en las regiones de interés con mayor impacto de la variabilidad climática durante los períodos 2030 – 2069 y 2070 – 2099.

II. METODOLOGÍA

II.1. Área de estudio

Sudamérica presenta diferentes patrones climáticos y meteorológicos, debido a su considerable extensión austral y a su prominente orografía, que incluyen características tropicales, subtropicales y extratropicales. Con más de 25000 km de costa, la región tiene un gran potencial eólico, especialmente a lo largo de las costas de Brasil, Colombia y el sur de Chile (Shadman et al., 2023). La porción occidental del continente está rodeada por el océano Pacífico y está fuertemente influenciada por el Anticiclón del Pacífico Sur (SPA) y las perturbaciones extratropicales de los vientos del oeste (Figura 1b). La porción oriental del continente está rodeada por el océano Atlántico, y la estacionalidad del campo de vientos se ve influenciada por diferentes fenómenos, como la confluencia de los vientos alisios en el sector ecuatorial y la variabilidad del Anticiclón del Atlántico Sur (SAA) (De Souza Ferreira et al., 2024).

La cordillera de los Andes discurre continuamente cerca de la costa occidental del continente y, por lo tanto, representa un obstáculo importante para el flujo troposférico, con condiciones secas hacia el oeste y condiciones húmedas hacia el este en latitudes tropicales/subtropicales. La meseta brasileña también tiende a bloquear la circulación de bajo nivel sobre Sudamérica subtropical (Garreaud et al., 2009). Al sur de los 40°S, el flujo del oeste en niveles bajos prevalece durante todo el año sobre los océanos adyacentes y el continente. En particular, sobre el extremo meridional de América del Sur y el Pacífico sur adyacente, los vientos del oeste son más fuertes alcanzando un máximo entre 45°S y 55°S (Garreaud et al., 2009).

Con base en la distribución y explotación del recurso eólico en América del Sur mencionada anteriormente, se definieron tres subregiones de interés para el presente estudio (Figura 1a): REG1 (0° - 20° S, 33° - 50° O), que abarca el nordeste de Brasil; REG2 (17° - 37° S, 58° - 77° O), que abarca principalmente el centro-norte de Chile y Argentina; y REG3 (37° - 57° S, 55° - 80° O), que se extiende sobre la Patagonia. Estas subregiones abarcan las áreas donde se ubican la mayoría de los proyectos eólicos sudamericanos, correspondientes a los principales países productores de energía eólica de la región: Brasil, Chile y Argentina.

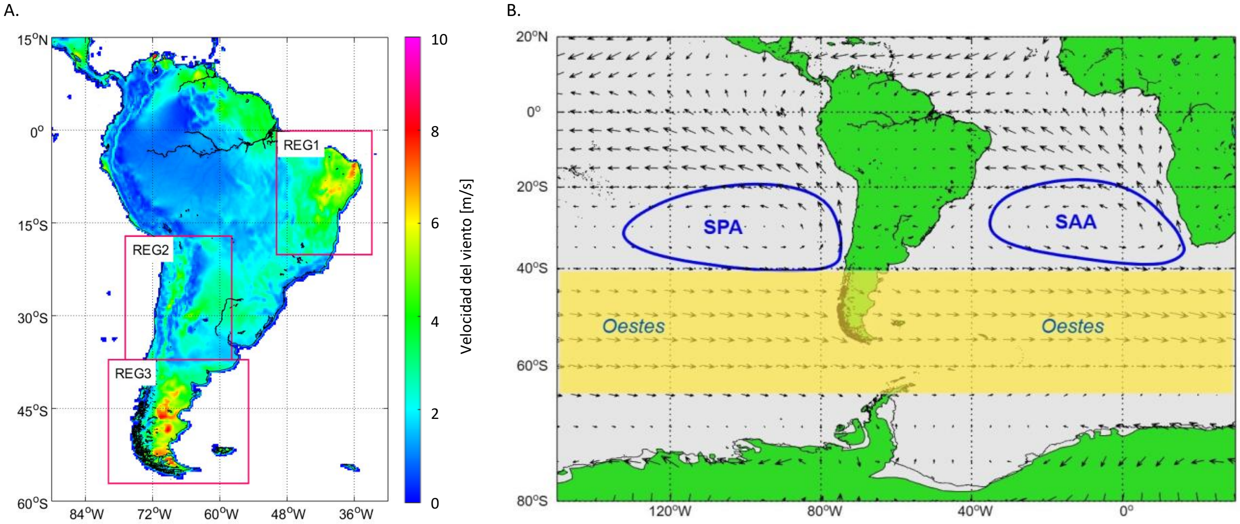

Figura 1.a) Distribución de la velocidad del viento a 100m sobre América del Sur y las subregiones seleccionadas. b) Diagrama esquemático de la media anual del campo de viento a 100m y sus principales moduladores climáticos sobre América del Sur. Fuente: datos de ERA5 (1980 – 2014).

II.2. Datos

Se descargaron datos de velocidad del viento cerca de la superficie (10 m), presión a nivel del mar (SLP) y temperatura superficial del mar (SST) de 14 modelos de CMIP6 (Tabla 1) para el período histórico 1980-2014 y los períodos futuros 2030 – 2069 y 2070 – 2099 bajo el escenario SSP2-4.5. Diversos autores han utilizado los modelos climáticos globales de CMIP6 para estudiar el comportamiento del recurso eólico (Carvalho et al., 2021; Deng et al., 2022; Qian & Zhang, 2021; Wu et al., 2020; Zhang et al., 2019) y su relación con diferentes patrones atmosféricos, como el ENSO (Fredriksen et al., 2020; Liao et al., 2021). Estos modelos se basan en una serie de trayectorias de emisiones nuevas y actualizadas que exploran una gama mucho más amplia de posibles resultados futuros que las incluidas en CMIP5. Dado que cada modelo tiene diferentes proyecciones cartográficas y resoluciones, se definió, por conveniencia, una cuadrícula horizontal homogénea con una resolución espacial de 1° x 1°, utilizando el método de interpolación bilineal implementado en el software Climate Data Operators (CDO), del Instituto Max Planck de Alemania (Greene et al., 2019). Todos los pasos descritos para la preparación y el análisis de datos se implementaron con el software Mathworks® Matlab.

Tabla 1. Información sobre los modelos de CMIP6 utilizados. Más detalle disponible en https://pcmdi.llnl.gov/CMIP6.

Modelo CMIP6	Resolución (°Lon x °Lat)			Experimento	Referencia	País de origen
	Viento	SST	SLP			
ACCESS-CM2	1.88 x 1.25	1.00 x 0.60	1.88 x 1.25	r1i1p1f1	Bi et al. (2020)	Australia
CanESM5-CanOE	2.81 x 2.81	1.00 x 0.62	2.81 x 2.81	r1i1p2f1	Swart et al. (2019)	Canadá
CMCC-CM2-SR5	1.25 x 0.94	0.99 x 0.62	1.25 x 0.94	r1i1p1f1	Cherchi et al. (2019)	Italia
CMCC-ESM2	1.25 x 0.94	0.99 x 0.62	1.25 x 0.94	r1i1p1f1	Lovato et al. (2022)	Italia
CNRM-CM6-1-HR	0.50 x 0.50	0.25 x 0.17	0.50 x 0.50	r1i1p1f2	Voldoire et al. (2019)	Francia
CNRM-ESM2-1	1.41 x 1.41	1.00 x 1.00	1.41 x 1.41	r1i1p1f2	Séférian et al. (2019)	Francia
FGOALS-f3-L	1.25 x 1.00	1.00 x 0.83	1.25 x 1.00	r1i1p1f1	He et al. (2020)	China
FIO-ESM-2-0	1.25 x 0.94	1.13 x 0.47	1.25 x 0.94	r1i1p1f1	Bao et al. (2020)	China
HadGEM3-GC31-LL	1.88 x 1.25	1.00 x 0.55	1.88 x 1.25	r1i1p1f3	Andrews et al. (2020)	Reino Unido
INM-CM5-0	2.00 x 1.50	1.00 x 1.00	2.00 x 1.50	r1i1p1f11	Volodin & Gritsun (2018)	Rusia
KIOST-ESM	1.88 x 1.88	1.00 x 0.90	1.88 x 1.88	r1i1p1f11	Y. H. Kim et al. (2020)	Corea del Sur
MIROC6	1.41 x 1.41	1.00 x 0.70	1.41 x 1.41	r1i1p1f1	Shiogama et al. (2023)	Japón
MIROC-ES2L	2.81 x 2.81	1.00 x 1.00	2.81 x 2.81	r1i1p1f2	Hajima et al. (2020)	Japón
UKESM1-0-LL	1.88 x 1.25	1.00 x 0.55	1.88 x 1.25	r1i1p1f2	Mulcahy et al. (2023)	Reino Unido

Los modelos globales de CMIP6 sólo proporcionan datos de velocidad del viento cercana a la superficie (10m). La ley de potencia es un método usado comúnmente para extrapolar la velocidad del viento v hasta la altura de la turbina h (Manwell, 2009; Tobin et al., 2015; Weber et al., 2018):

$$v_h = v_0 \left(\frac{z_h}{z_0}\right)^{\alpha} \tag{1}$$

donde α representa el exponente de cizalladura del viento, el cual es típicamente igual a 0.143 (Li et al., 2022; Tian et al., 2019). La altura de la turbina se estableció como z_h= 100 m, mientras que cerca de la superficie z_0 = 10 m. En lo adelante denominamos a la velocidad del viento a la altura de la turbina v_h como WS100.

II.3. Moduladores climáticos

Para investigar el rol de los patrones de circulación atmosférica en el comportamiento de WS100 en el área de estudio, se tomaron en consideración dos sistemas semipermanentes que modulan el clima de la región: el SPA y el SAA. Para establecer un índice que mide la intensidad del SPA, calculamos las anomalías medias mensuales del SLP, entre 15º - 50º S y 150º - 70º O, que corresponden al centro del SPA (Ancapichún & Garcés-Vargas, 2015). Las anomalías se calcularon restando la media histórica (1980-2014) y luego eliminando el ciclo estacional. De manera similar, se determinó el índice de intensidad del SAA para el área entre 10° - 40° S y 40° O - 10° E (Lübbecke et al., 2014).

Como segundo paso, se analizó además la influencia de dos modos de variabilidad climática con gran influencia sobre la región: ENSO y AAO. En el caso del ENSO, se utilizó el índice ONI (*Oceanic Niño Index*), calculado como la media móvil trimestral de las anomalías de SST en la región del Niño 3.4 (5°N-5°S, 120°-170°O). Para calcular el índice AAO, se utilizó la definición propuesta por Marshall (2003), basada en la diferencia en las anomalías normalizadas de SLP entre las bandas latitudinales centradas en 40°S y 65°S. En ambos casos, se utilizó el algoritmo desarrollado por (Greene et al., 2019) para Mathworks® Matlab.

Todos los índices seleccionados (SPA, SAA, ONI y AAO) se calcularon a partir de simulaciones CMIP6, ya que cada modelo tiene sus propios forzamientos y se buscó explorar las conexiones entre la velocidad del viento y los índices seleccionados dentro de la variabilidad interna de cada modelo. Los datos de reanálisis del ERA5, del Centro Europeo de Previsiones Meteorológicas a Plazo Medio (ECMWF) se utilizaron como referencia para validar los índices obtenidos de los modelos de CMIP6. ERA5 se utiliza ampliamente para la validación de modelos climáticos

(Aramburo et al., 2022; Hayes et al., 2021; Olauson, 2018; Patel et al., 2022; Sakuru & Ramana, 2023; Soukissian et al., 2021).

En el caso de los índices ONI y AAO, los criterios de comparación entre los resultados obtenidos para cada modelo CMIP6 y los obtenidos mediante de reanálisis del ERA5 fueron: la correspondencia con el período histórico 1980-2014, el período de retorno, la distribución de los valores del índice y las huellas espaciales en los campos de SST y SLP. Respecto a los índices SPA y SAA, los criterios considerados fueron: la correspondencia con el período histórico 1980-2014, la distribución de los valores del índice, el comportamiento del ciclo anual y las huellas espaciales en los campos de SST y SLP.

II.4. Análisis EOF y relación de WS100 con los moduladores climáticos

Para cada subregión, se aplicó un análisis de funciones ortogonales empíricas (EOF) a las anomalías mensuales (MON) y estacionales de verano (DJF) e invierno (JJA) de WS100, calculadas según el promedio histórico durante el período 1980-2014. Esta técnica es útil para analizar datos de velocidad del viento y aislar señales climáticas específicas de series temporales (Farjami & Hesari, 2020; Sinha et al., 2020; Wang et al., 2024; Watts et al., 2017; Zhou et al., 2022). El análisis EOF proporciona patrones espaciales (designados en este estudio como EOF1, EOF2, etc.) donde cada patrón corresponde a un vector de carga, que es linealmente independiente de todos los demás, y sus respectivas series temporales se denominan componentes principales (PC1, PC2, etc.). Tras el análisis EOF, los PC obtenidos se correlacionaron con los índices SPA, SAA, ONI y AAO utilizando series mensuales (MON) y estacionales (JJA y DJF, considerando meses individuales). Para determinar el grado de correlación entre los PC y los índices climáticos, se utilizó el método de Pearson, estableciendo la significancia con un nivel de confianza del 95%.

II.5. Cálculo de WPD y variaciones en el futuro

Luego de determinar la influencia de los principales patrones atmosféricos que determinan el comportamiento de WS100 en las diferentes subregiones, se evaluó el comportamiento de WPD sobre el área de estudio. WPD [W/m^2] depende directamente de la velocidad del viento v (WS100) al cubo y se calculó de acuerdo con la ecuación:

$$WPD = \frac{1}{2}\rho v^3 \tag{2}$$

donde ρ [kg/m^3] es la densidad del aire que, aunque algunas investigaciones la asumen como un valor constante, en nuestro caso y dada extensión y complejidad del área de estudio, la estimamos de la siguiente forma (De Souza Ferreira et al., 2024; Sawadogo et al., 2021):

$$\rho \cong \frac{353.4\left(1 - \frac{z_h}{45271}\right)^{5.2624}}{T} \tag{3}$$

donde z_h = 100m es la altura de la turbina y T es la temperatura del aire [K]. Dado que los modelos climáticos no proporcionan temperatura del aire a 100m, esta variable se estimó teniendo en cuenta la tasa vertical de la adiabática saturada de la atmósfera, según la cual la temperatura del aire disminuye aproximadamente a razón de 0.6°C cada 100m (De Souza Ferreira et al., 2024):

$$T = T_{2m} - \Gamma_{sat} \tag{4}$$

donde T_{2m} [K] es la temperatura del aire cercana a la superficie (2m) y Γ_{sat} es la tasa vertical de la adiabática saturada de la atmósfera, que en este caso para una altura de 100m tiene un valor de Γ_{sat} = 0.6.

Luego de obtener la distribución espaciotemporal de WPD a partir de WS100 sobre toda el área de estudio para cada modelo se calcularon las diferencias de WPD medio en cada período futuro con respecto al período histórico. Puesto que el aporte de nuestra investigación está dirigido fundamentalmente a la industria eólica, es importante encontrar aquellas regiones con cambios significativos de WPD. Para ello establecimos un umbral de valor medio de WS100 ≥ 3m/s, dado que para valores de velocidad de viento inferiores las aspas de la turbina eólica usada como referencia no se mueven (*cut-in:* 3m/s). De esta forma despreciamos aquellas áreas donde WS100 tiene valores inferiores a 3m/s durante el período histórico y no presentan aumentos en el futuro.

Esto nos permite tener en cuenta solamente las áreas que se encontraban por encima de este umbral y presentan cambios en el futuro, así como posibles zonas que superaron dicho umbral y pudieran considerarse como nuevas zonas de interés.

Después de calcular las diferencias determinamos las regiones con cambios significativos en WPD y que tuvieran consistencia con al menos el 80% de los modelos analizados en cuanto al signo, es decir, aumento o disminución. Luego construimos la serie temporal de anomalías de WS100 medio y comparamos con ERA5 en el período histórico, teniendo en cuenta criterios como el comportamiento del ciclo anual y la distribución de las series, a fin de conocer el desempeño de los modelos de CMIP6 para reflejar el comportamiento de WS100 en las regiones de interés. Además, construimos la serie temporal de anomalías de WPD medio en cada región y analizamos su tendencia para cada modelo hasta 2099 para compararla con la tendencia de los patrones atmosféricos.

II.6. Estimación de la energía generada

Para calcular las variaciones de energía eólica anual media generada en los períodos futuros 2030-2069 y 2070-2099 con respecto al período histórico 1980-2014 es necesario conocer la distribución de frecuencias de la velocidad del viento media horaria para cada uno de los períodos. Una amplia literatura ha reportado que la aplicación de la distribución de Weibull al modelar datos de velocidad del viento reproduce adecuadamente el régimen de velocidad del viento. La función de densidad de probabilidad de la distribución de Weibull se expresa de la siguiente manera:

$$f(v_i) = \frac{k}{c}\left(\frac{v_i}{c}\right)^{k-1} exp\left[-\left(\frac{v_i}{c}\right)^{k}\right] \tag{5}$$

donde v_i, c y k son la velocidad del viento media (WS100), el parámetro de escala y el parámetro de forma respectivamente. Sin embargo, puesto que los datos de velocidad del viento que ofrecen los modelos de CMIP6 en la mayoría de los casos tiene una resolución temporal máxima diaria (3 horas en algunos pocos casos) es necesario estimar la distribución de frecuencias horaria. Para ello utilizamos la metodología propuesta por (Shin et al., 2018) para estimar los parámetros de la función de densidad de probabilidad de Weibull a partir de datos diarios, los cuales sí disponemos para los modelos utilizados, excepto para el CanESM5-CanOE y FGOALS-f3-L.

El método consiste en calcular primeramente los momentos acumulativos brutos (CRM) de 1er y 2do orden de los datos de velocidad del viento correspondientes a escalas temporales más gruesas. Por ejemplo, si se dispone de datos de velocidad media diaria del viento (como en nuestro caso), se calculan las velocidades medias del viento de escalas temporales más gruesas (es decir, de 2, 3, 4, …, y hasta 30 días) agregando los datos de velocidad media diaria del viento. Se calculan los CRM de los datos de velocidad media diaria del viento de 2, 3, 4, …, y 30 días (convertido en momento bruto de muestra):

$$h^{er}\ momento\ bruto\ de\ muestra = \mu_R^h = \frac{1}{n}\mu_{CR}^h = \frac{1}{n}\sum_{i=1}^{n} v_i^h \tag{6}$$

Seguidamente se construye un modelo lineal entre el logaritmo de los CRM y el logaritmo de las escalas temporales. Luego, se estiman los CRM correspondientes a la escala temporal precisa de interés, por ejemplo 1 h (como en nuestro estudio), a partir del modelo lineal generado anteriormente. Posteriormente se convierten las estimaciones de CRM en momentos centrales. Dado que los CRM no pueden aplicarse directamente para ajustar la distribución de probabilidad, deben convertirse en los momentos centrales que se utilizan habitualmente en el método de momentos.

$$1^{er} momento\ central\ de\ muestra = \mu_C^1 = \mu_R^1 \tag{7}$$

$$2^{do}\ momento\ central\ de\ muestra = \mu_C^2 = \mu_R^2 - (\mu_C^1)^2 \tag{8}$$

Finalmente se estiman los parámetros de la distribución de probabilidad de Weibull mediante el método de momentos con estimaciones de momento central. Los momentos centrales teóricos de primer y segundo orden de la distribución de Weibull se expresan de la siguiente manera:

$$\mu_C^1 = c\Gamma\left(1 + {}^{1}\!/_{k}\right) \tag{9}$$

$$\mu_C^2 = c^2\left[\Gamma\left(1 + {}^{2}\!/_{k}\right) - \Gamma^2\left(1 + {}^{1}\!/_{k}\right)\right] \tag{10}$$

donde $\Gamma()$ es la función gamma. El método de momentos para la distribución de Weibull identifica los parámetros que producen los momentos teóricos de 1er y 2do orden equivalentes a los momentos muestrales 1er y 2do orden. Este problema del método de momentos se resolvió mediante un método de optimización numérica en Matlab. Luego, una vez que se conoce la función de distribución de probabilidad de Weibull, la energía generada se calculó según la ecuación:

$$E = T\sum_{i=1}^{N} P(v_i)f(v_i)\Delta v_i \tag{11}$$

donde $P(v_i)$ [W] es la potencia a la velocidad v_i, $f(v_i)$ es la probabilidad de que el viento tenga la velocidad v_i según la distribución de Weibull, Δv_i es el ancho del intervalo de velocidad, es decir, la diferencia entre los valores de v_i adyacentes, y T es el tiempo total (considerando un año: T = 8760 horas). Los valores de $P(v_i)$ se obtuvieron de la curva de potencia característica de la turbina eólica Vestas V126-3.45 MW, usada comúnmente como referencia en estudios enfocados en la generación eólica en tierra (Bianchi et al., 2022; De Jong et al., 2019; Russo et al., 2023). Esta turbina tiene una velocidad de *cut-in* de 3m/s, *cut -out* de 22.2m/s y una potencia nominal de 3.45MW (https://www.vestas.com).

III. EVALUACIÓN DE LA VARIABILIDAD DE LA VELOCIDAD DEL VIENTO Y SUS MODULADORES CLIMÁTICOS EN AMÉRICA DEL SUR USANDO SIMULACIONES DE CMIP6 (1980 – 2014)

Resumen

En este estudio, aplicamos un análisis de funciones ortogonales empíricas (EOF) al comportamiento de la velocidad del viento mensual a 100 m (WS100) en regiones seleccionadas de Sudamérica para detectar su modulación por diferentes patrones atmosféricos. Se utilizaron datos de reanálisis de ERA5 y 14 modelos climáticos globales de CMIP6 para el período 1980-2014. Encontramos que el Anticiclón del Atlántico Sur (SAA) es el principal modulador de WS100 sobre el nordeste de Brasil con una relación directa (coeficientes de correlación de hasta 0,55) entre la intensidad de SAA y el primer componente principal (PC1), que explica el 59,1% de la varianza total de WS100 en esa región. Esto significa que a medida que aumenta la intensidad de SAA, WS100 también aumenta sobre el nordeste de Brasil. Descubrimos un patrón de anomalías de presión a nivel del mar centrado en el Pasaje de Drake, al que denominamos patrón Patagonia-Antártica (PAT), y que constituye el principal modulador de WS100 sobre la Patagonia. Se hallaron correlaciones negativas significativas (de hasta -0,68) entre PAT y la PC1, que explica el 52,2% de la varianza total para dicha región. La fase positiva del índice PAT provoca una disminución de WS100 sobre la Patagonia, mientras que WS100 aumenta durante la fase negativa de PAT. También determinamos que la Oscilación Antártica (AAO) es el segundo modo de variabilidad que determina el campo WS100 sobre la Patagonia, dado por los altos coeficientes de correlación (de hasta 0,52) entre AAO y la PC2, que explica el 22,8% de la varianza total. La fase positiva de AAO provoca un aumento de WS100 sobre el extremo sur de la Patagonia y una disminución al norte de los 45° S; ocurre lo contrario durante la fase negativa de AAO. Estos resultados son de gran relevancia para una mejor comprensión de las causas de la variabilidad del viento en América del Sur, lo cual es esencial para la evaluación del recurso eólico, la planificación del sistema a largo plazo y la evaluación de riesgos en proyectos de energía eólica actuales y futuros.

RESEARCH ARTICLE

International Journal of Climatology, 2025

https://doi.org/10.1002/joc.8921

Evaluating Wind Speed Variability and Its Climate Modulators in South America Using CMIP6 Simulations (1980–2014)

Ovidio Llompart[1], Héctor H. Sepúlveda[2,3], Martín Jacques-Coper[2,4,5], Marieta Hernández[6]

[1]Doctoral Program in Energy, University of Concepcion, Concepción, Chile
[2]Department of Geophysics, University of Concepcion, Concepción, Chile
[3]Centro de Estudios del Cuaternario de Fuego-Patagonia y Antártica (CEQUA), Punta Arenas, Chile
[4]Center for Oceanographic Research COPAS Coastal, University of Concepcion, Concepción, Chile
[5]Center for Climate and Resilience Research (CR2), Santiago, Chile
[6]Doctoral Program in Environmental Sciences, Mention in Continental Aquatic System, University of Concepcion, Concepción, Chile

Correspondence: Martín Jacques-Coper (martinjacques@udec.cl)

Received: 5 September 2024, **Revised:** 22 May 2025, **Accepted:** 23 May 2025

Keywords: atmospheric patterns, climate variability, CMIP6, wind resource

Abstract

In this study, we applied an Empirical Orthogonal Functions (EOF) analysis on the behavior of monthly wind speed at 100 m (WS100) in selected regions of South America to detect its modulation by different atmospheric patterns. Reanalysis data from ERA5 and 14 global climate models from CMIP6 were used for the period 1980-2014. We found that the South Atlantic Anticyclone (SAA) is the main WS100 modulator over northeastern Brazil with a direct relationship (correlation coefficients up to 0.55) between the SAA intensity and the 1st principal component (PC1), which explains 59.1% of the WS100 total variance in that region. This means that as SAA intensity increases, WS100 increases as well over northeast Brazil and vice versa. We discovered a pattern of sea level pressure anomalies centered around the Drake Passage, which we named the Patagonia-Antarctic pattern (PAT), and it is the main WS100 modulator over Patagonia. Significant negative correlations (up to -0.68) were found between PAT and PC1, which explains 52.2% of the total variance for that region. The positive phase of the PAT index causes a decrease of WS100 over Patagonia, while WS100 increases during the negative phase of PAT. We also determined that the Antarctic Oscillation (AAO) is the second variability mode that determines the WS100 field over Patagonia, given by high correlation coefficients (up to 0.52) between AAO and PC2, which explains 22.8% of the total variance. The positive phase of AAO causes an increase of WS100 over the southern tip of Patagonia, and a decrease north of 45° S, the opposite occurs during the negative phase of AAO. These results are of great relevance for a better understanding of wind variability causes in South America, which is essential for wind resource evaluation, long term system planning and risk assessment in current and future wind power projects.

1. Introduction

Natural climate variability is caused by patterns or oscillations that take place recurrently on different time scales (months, years, decades) in the large-scale atmospheric circulation and that strongly modulate temperature, wind, and precipitation, among other climate variables. Different datasets and analysis techniques have allowed researchers to find many patterns of atmospheric variability relevant for South America, but most of the inter-annual and lower-frequency variability appears to be linked to a few global modes: El Niño-Southern Oscillation (ENSO), the Antarctic Oscillation (AAO), and the Pacific Decadal Oscillation (PDO)as stated by Garreaud et al. (2009).

ENSO is a coupled ocean-atmosphere phenomenon rooted in the tropical Pacific, characterized by irregular fluctuations between its warm (El Niño) and cold (La Niña) phases with a periodicity ranging from 2 to 7 years (Garreaud et al., 2009). Small perturbations to the tropical climate system may grow into either El Niño or La Niña through the Bjerknes positive dynamic feedback of the ocean–atmosphere interaction in the equatorial Pacific (An & Jin, 2004). The equatorial SST zonal gradient drives the easterlies over the tropical Pacific and these easterlies in turn create the cold SST over the eastern Pacific resulting in the strengthening of the SST gradient (Bjerknes, 1969). The transition from an El Niño to a La Niña event, and vice versa, is through a delayed negative feedback of ocean dynamical adjustment (An & Jin, 2004).

The PDO is a long-lived pattern of Pacific climate variability. The PDO is often described as ENSO-like, because the spatial climate fingerprints of its warm and cold phase have strong resemblance with those of El Niño and La Niña events, respectively. It turns out that PDO-related anomalies of precipitation and temperature over South America are ENSO-like (i.e., similar spatial structure), but their amplitude is about half of their ENSO counterparts (Garreaud et al., 2009).

The AAO is the leading pattern of tropospheric circulation variability south of 20°S, and it is characterized by pressure anomalies of one sign centered in the Antarctic and anomalies of the opposite sign on a circumglobal band at about 40°S – 50°S (Thomson & Wallace, 2000). The AAO signal extends coherently up to the lower stratosphere, and it seems to arise from the interaction between the eddies and the zonal mean flow (Codron, 2995). The positive phase of the AAO is associated with decreased (increased) surface pressure and geopotential heights over Antarctica (midlatitudes) and a strengthening and poleward shift of the westerlies. Opposite conditions prevail during the negative phase (Garreaud et al., 2009)

Most studies regarding this topic in South America focus on variables such as precipitation and drought events (Mortensen et al., 2018; Sulca et al., 2024), and to a lesser extent on wind. In the case of wind, according to Bianchi et al. (2017), both ENSO and AAO show relevant signals on wind speed at 50 m height in the southern region of South America. Bianchi et al. (2022) found that the wind resource in that region is more sensitive to AAO, with a negative and stronger relationship in spring and summer, that is, the positive phase of the AAO causes a decrease in wind speed over the region and vice versa. In the case of Chile, Watts et al. (2017) detected that the warm phase of ENSO reduces wind speed in most sites in central-northern Chile; however, the magnitude and sometimes the signal depend on the site analyzed and the month in which the phenomena occur.

The combination of some of those atmospheric patterns and local geography causes wind speed variations on multiple time scales, and power grids are increasingly more exposed to climate variability, due to the incorporation of renewable energies such as wind power. High-frequency variations (local to mesoscale) have implications for daily operational aspects of wind farms such as frequency control, load tracking, etc. (Kim et al., 2021; Gugliani et al., 2021; Khasanzoda et al., 2022). When considering planning, long-term design, and evaluation of the wind resource, variability at large spatio-temporal scales become a major concern. However, wind modulations by atmospheric patterns are not often considered in on-site data collection for the installation of wind farms (Bianchi et al., 2022).

Onshore wind power generation is a tested and mature technology with an extensive global supply chain. In South America, some countries have experienced a dramatic increase in wind power generation since 2019. The main wind power generators are Brazil, Chile, and Argentina; followed by Uruguay and Peru. These five countries represent 99.3% of the total installed capacity in the region at the end of 2022 (IRENA, 2023). To further increase the percentage of wind power generation in the electricity mix and achieve the Net Zero Emissions Scenario by 2050, there is a great need for the expansion of the exploitation of this resource in the region. The wind energy that can potentially be harvested by wind turbines is estimated through the wind potential (Koletsis et al., 2016). Since the wind potential density depends directly on the wind speed cubed, a small change in wind speed can have substantial consequences for wind power resources (Tian et al., 2019).

However, the spatiotemporal variability of the wind resource makes the accurate assessment of wind energy a complicated affair (Jung & Schindler, 2020). In this sense, previous studies have investigated the influence of different atmospheric patterns on the behavior of wind speed and wind power generation (Brayshaw et al., 2011; Mendoza et al., 2014; Ohba et al., 2016; Alonzo et al., 2017; Correia et al., 2017; Cradden et al., 2017; Ravestein et al., 2018; Garrido-Perez et al., 2020; Dalton et al., 2021). The results of these studies highlight the need to better understand the link between the main atmospheric circulation patterns and the variability of the wind resource.

Indeed, this improves wind resource assessment and reduces the long-term risk in wind power generation. As various studies show (Ravestein et al., 2018; Jung & Schindler, 2020), wind climate variability related to different atmospheric patterns has a significant impact on wind power generation. However, most of the research has been carried out in Europe, Asia, and North America. The main objective of this work is therefore to determine the impact of different atmospheric patterns on the variability of wind speed at the typical height of a wind turbine in selected regions of South America. Such information is of great relevance to a better understanding of wind variability causes in the region, which is essential for wind resource evaluation, long term system planning and risk assessment in current and future wind power projects.

1.1. Study area

Due to its considerable southern extent and prominent orography, South America presents different climate and weather patterns that include tropical, subtropical and extratropical characteristics. The western portion is surrounded by the Pacific Ocean, and it is strongly influenced by the subtropical South Pacific Anticyclone (SPA) and extra-tropical westerly disturbances. The eastern portion of the continent is surrounded by the Atlantic Ocean, and the seasonality of the wind field is influenced by different phenomena, such as the confluence of the trade winds in the equatorial sector and the variability of the subtropical South Atlantic Anticyclone (SAA) (de Souza Ferreira et al., 2024). The Andes cordillera runs continuously close to the western coast of the continent and therefore represents a major obstacle to the tropospheric flow. The Brazilian plateau also tends to block low-level circulation over subtropical South America (Garreaud et al., 2009).

Based on the aforementioned exploitation of the wind resource in South America, three subregions of interest were defined for the present study (Figure 1a), denominated REG1 (0° - 20° S, 33° - 50° W), which comprises the northeast of Brazil, REG2 (17° - 37° S, 58° - 77° W) which mainly covers central-northern Chile and Argentina, and REG3 (37° - 57° S, 55° - 80° W) that extends over Patagonia. These subregions cover the areas where most of the South American wind power projects are located, corresponding to the main wind power producing countries in the region: Brazil, Argentina and Chile. The average behavior of wind speed at 100 m (WS100) during 1980-2014 (Figures 1b and c) in region REG1 shows a clear annual cycle with a maximum in winter (July-August, JJA) and a minimum in summer (December-February, DJF). REG2 reaches maximum values in spring (September-November, SON) and minimum values in autumn (March-May, MAM), while in the case of REG3 the maximum occurs during the austral summer and the minimum occurs at the end of winter and beginning of spring.

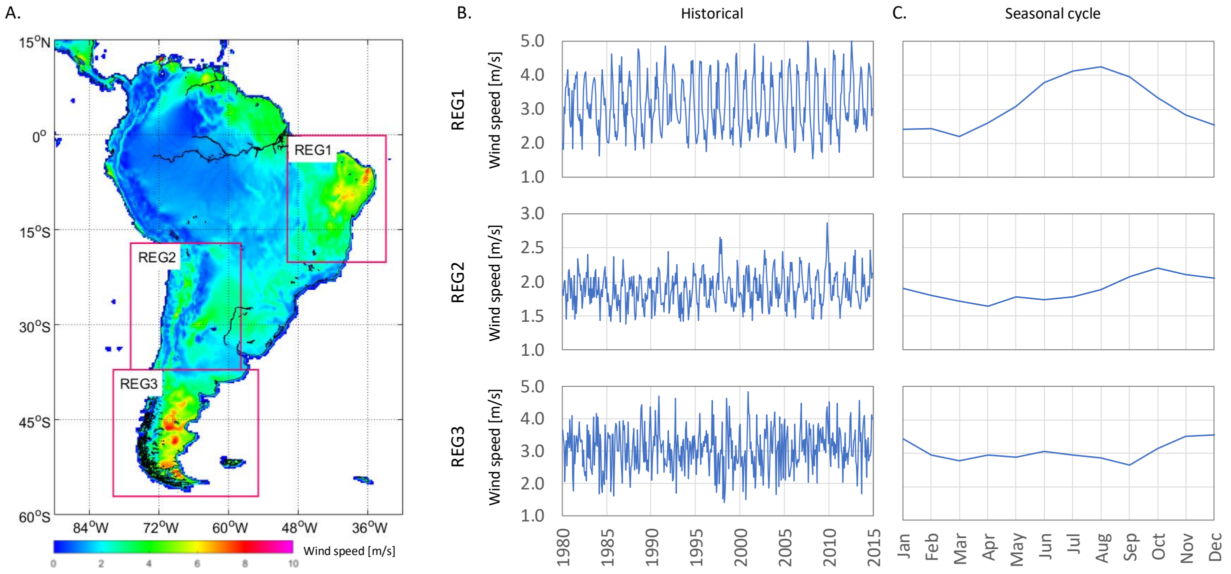

Figure 1. a) Climatology of wind speed at 100 m (WS100) over South America; the selected subregions are enclosed by rectangles. b) Historical behavior of monthly WS100 for each subregion. c) Annual cycle of WS100 for each subregion. Wind speed at 100 m for 1980-2014 retrieved from the ERA5 reanalysis.

2. Methodology

2.1. Data

Near-surface (10 m) wind speed, sea level pressure (SLP), and sea surface temperature (SST) data from 14 CMIP6 models (Table 1) were downloaded for the historical period 1980 – 2014. CMIP6 global climate models (GCM) have been used by several authors to study the behavior of the wind resource (Wu et al., 2020; Carvalho et al., 2021; Qian & Zhang, 2021; Zhang & Li, 2021; Deng et al., 2022) and their relationship to different atmospheric patterns such as ENSO (Fredriksen et al., 2020; Liao et al., 2021). These models run on a series of new and updated emission pathways that explore a much broader range of possible future outcomes than those included in CMIP5.

Since each model has different cartographic projections and different resolutions, a homogeneous horizontal grid of 1° x 1° spatial resolution was defined for convenience, using the bilinear interpolation method implemented within the Climate Data Operators (CDO) software, from the German Max Planck Institute (Greene C. A. et al., 2019). All steps described for data preparation and analysis were implemented with Mathworks® Matlab software (version2023a).

The CMIP6 GCMs only provide near-surface (10 m) wind speed. The power law is a method commonly used by different authors to extrapolate the wind speed v at turbine height h (Weber et al., 2018; Tobin et al., 2015; Tobin et al., 2016; Manwell et al., 2010):

$$v_h = v_0 \left(\frac{z_h}{z_0}\right)^{\alpha} \tag{1}$$

where α represents the wind shear exponent, which is typically equal to 0.143 (Li et al., 2022; Tian et al., 2019). The height of the turbine was set as z_h= 100 m, while near the surface z_0 = 10 m. The wind speed at turbine height v_h is termed WS100.

Table 1. Information of each CMIP6 model used in the study. Further information on https://pcmdi.llnl.gov/CMIP6/.

Climatic model	Resolution (°Lon x °Lat)			Variant label	Institute	Country of origin
	Wind	SST	SLP			
ACCESS-CM2	1.88 x 1.25	1.00 x 0.60	1.88 x 1.25	r1i1p1f1	Commonwealth Science and Industrial Research Organization	Australia
CanESM5-CanOE	2.81 x 2.81	1.00 x 0.62	2.81 x 2.81	r1i1p2f1	Canadian Centre for Climate Modelling and Analysis	Canada
CMCC-CM2-SR5	1.25 x 0.94	0.99 x 0.62	1.25 x 0.94	r1i1p1f1	Euro-Mediterranean Center on Climate Change	Italy
CMCC-ESM2	1.25 x 0.94	0.99 x 0.62	1.25 x 0.94	r1i1p1f1	Euro-Mediterranean Center on Climate Change	Italy
CNRM-CM6-1-HR	0.50 x 0.50	0.25 x 0.17	0.50 x 0.50	r1i1p1f2	National Center for Meteorological Research	France
CNRM-ESM2-1	1.41 x 1.41	1.00 x 1.00	1.41 x 1.41	r1i1p1f2	National Center for Meteorological Research	France
FGOALS-f3-L	1.25 x 1.00	1.00 x 0.83	1.25 x 1.00	r1i1p1f1	Institute of Atmospheric Physics of Chinese Academy of Science	China
FIO-ESM-2-0	1.25 x 0.94	1.13 x 0.47	1.25 x 0.94	r1i1p1f1	First Institute of Oceanography	China
HadGEM3-GC31-LL	1.88 x 1.25	1.00 x 0.55	1.88 x 1.25	r1i1p1f3	Met Office Hadley Centre	U.K.
INM-CM5-0	2.00 x 1.50	1.00 x 1.00	2.00 x 1.50	r1i1p1f11	Institute of Numerical Mathematics	Russia
KIOST-ESM	1.88 x 1.88	1.00 x 0.90	1.88 x 1.88	r1i1p1f11	Korea Institute of Ocean Science and Technology	South Korea
MIROC6	1.41 x 1.41	1.00 x 0.70	1.41 x 1.41	r1i1p1f1	Japanese Modelling Community	Japan
MIROC-ES2L	2.81 x 2.81	1.00 x 1.00	2.81 x 2.81	r1i1p1f2	Japanese Modelling Community	Japan
UKESM1-0-LL	1.88 x 1.25	1.00 x 0.55	1.88 x 1.25	r1i1p1f2	Met Office Hadley Centre	U.K.

2.2. Atmospheric patterns

To investigate the role of atmospheric circulation patterns on the behavior of WS100 in the study area, as a first step, two semi-permanent systems that modulate the climate of the region were taken into consideration: the SPA and the SAA. To establish an index that measures the intensity of the SPA, we calculated the monthly mean SLP anomalies, between 15º - 50º S and 150º - 70º W, which correspond to the long-term SPA center (Ancapichún & Garcés-Vargas, 2015). The anomalies were calculated by subtracting the historical mean (1980-2014) and then removing the seasonal cycle. In a similar way, the SAA intensity index was determined for the area between 10° - 40° S and 40°

W - 10° E (Lübbecke et al., 2014). As a second step, the influence of two modes of climate variability was analyzed: ENSO and AAO. In the case of ENSO, the ONI index was used (Figure 2, left) which is calculated as the three-month running mean of SST anomalies in the Niño 3.4 region (5°N-5°S, 120°-170° W). To calculate the AAO index (Figure 2, right), the definition proposed by Marshall (2003) was used, which is based on the difference in normalized SLP anomalies between latitudinal bands centered on 40°S and 65°S. In both cases, we used the algorithm developed by Greene et al. (2019) for Mathworks® Matlab. All of the chosen indices, SPA, SAA, ONI and AAO were calculated from CMIP6 simulations, since each model has its own forcings and we wanted to explore the connections between wind speed and the chosen indices inside each model internal variability.

ERA5 reanalysis data from the European Center for Medium-Range Weather Forecasts (ECMWF) was used as reference to validate the indices obtained from the GCMs. ERA5 is widely used for climate models validation (Olauson, 2018; Hayes et al., 2021; Soukissian et al., 2021; Aramburo et al., 2022; Patel et al., 2022; Sakuru & Ramana, 2023). Figure 2 shows the historical series of the indices calculated for the selected atmospheric patterns and their spatial footprints in the SST and SLP fields, using monthly values of SST and SLP during 1980-2014, retrieved from ERA5 reanalysis. In the case of the ONI and AAO indices, the criteria for comparison between the results obtained for each CMIP6 model and those obtained using the ERA5 reanalysis were: correspondence with the historical period 1980-2014, return period, distribution of the index values, as well as the spatial footprints on the SST and SLP fields. Regarding the SPA and SAA indices, the criteria taken into account were: correspondence with the historical period 1980-2014, distribution of the index values, behavior of the annual cycle, as well as the spatial footprints on the SST and SLP fields.

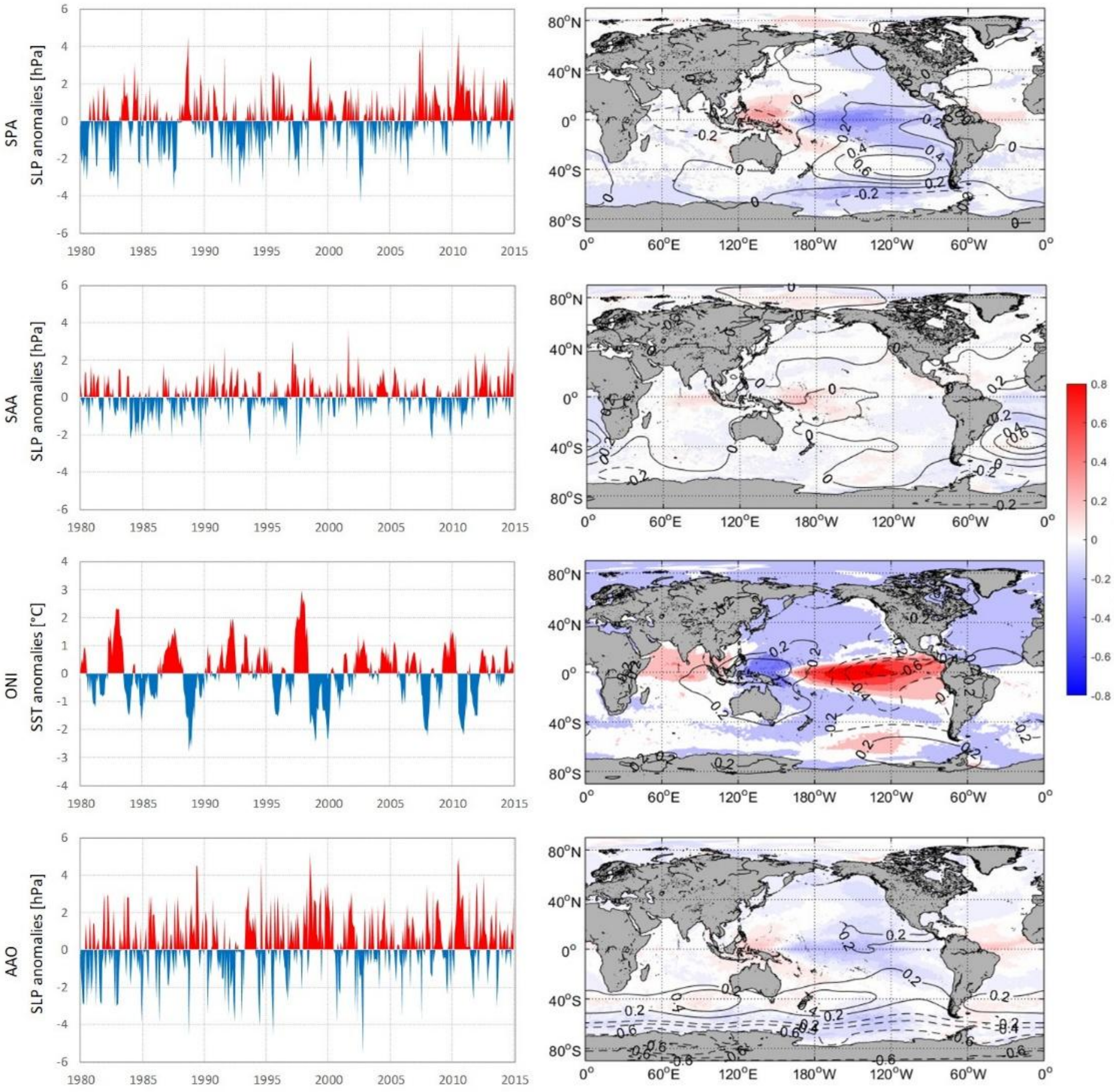

Figure 2. Historical series (left) and spatial footprints (right) of SPA, SAA, ONI and AAO indices over the SST (colors) and SLP (contours) fields. The values in right panels correspond to the Pearson correlation coefficients at a 95% confidence interval. Calculated for SPA, SAA, ONI and AAO using monthly values of SST and SLP during 1980-2014 retrieved from the ERA5 reanalysis.

2.3. EOF analysis on WS100 and relationships with the atmospheric patterns

For each subregion, an empirical orthogonal functions (EOF) analysis was applied to the monthly (MON) and seasonal anomalies for summer and winter of WS100, calculated according to the historical average during the period 1980-2014. This technique is useful for analyzing wind speed data and isolating specific climate signals from time series (Watts et al., 2017; Farjami & Hesari, 2020; Sinha et al., 2020; Zhou et al., 2022; Wang et al., 2024). The EOF analysis provides spatial patterns (designated in this study as EOF1, EOF2, etc.) where each pattern corresponds to a load vector, which is linearly independent of all others, and its respective time series are termed principal components (PC1, PC2, etc.). After the EOF analysis, the PCs obtained were correlated with the SPA, SAA, ONI and AAO indices using monthly and seasonal (JJA and DJF, considering individual months) series. To find the degree of correlation between the PCs and the climatic indices, the Pearson method was used and significance was established at the 95% confidence level.

3. Results

3.1. Representation of the atmospheric patterns.

Regarding the distributions of the index values (Figure 3), the GCMs show in general a similar behavior, although slight differences are observed. Specifically, in the case of ONI (Figure 3c), the GCMs show several differences: in contrast with the ERA5-derived index, CNRM-CM6-1-HR, CNRM-ESM2-1, and INM-CM5-0 present very low amplitude, which barely exceed the threshold of +/-0.5 °C that determines El Niño/La Niña events according to NOAA, respectively. On the contrary, CMCC-CM2-SR5, CMCC-ESM2, FGOALS-f3-L, KIOST-ESM, MIROC6 and MIROC-ES2L overestimate the amplitude of the series.

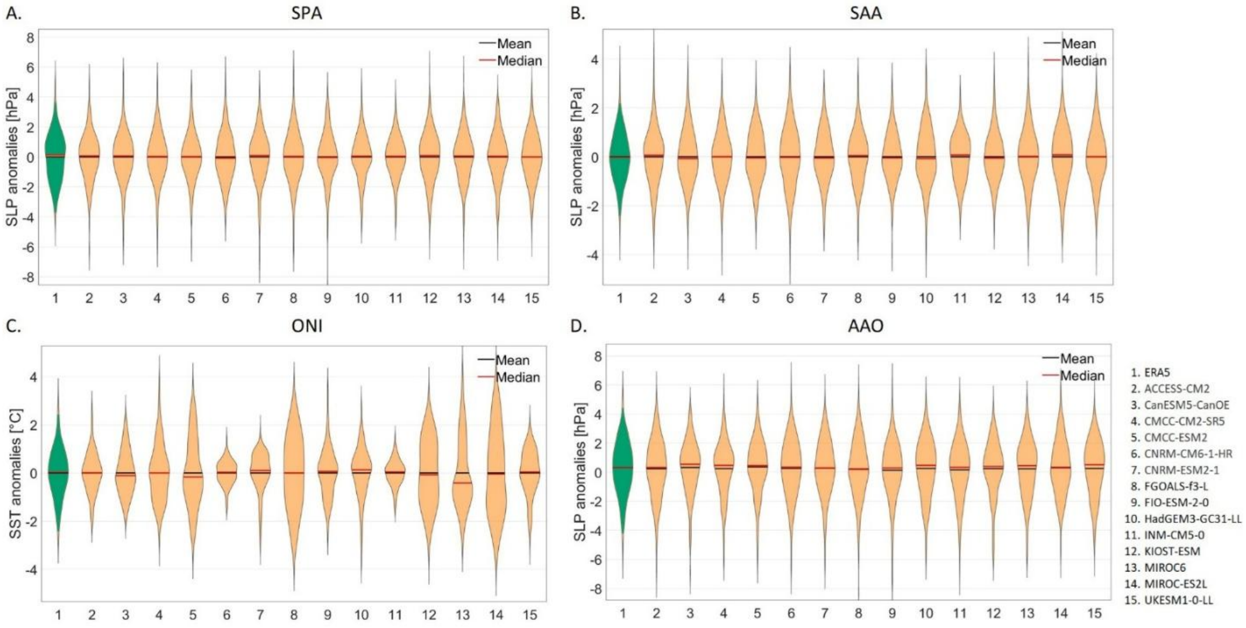

Figure 3. Violin plots showing the values distribution of each index during 1980-2014: a) SPA, b) SAA, c) ONI, and d) AAO.

The seasonality of SPA and SAA (considering SLP monthly mean values of the anticyclone center, without removing the seasonal cycle) as shown in Figure 4 top panels, is reasonably depicted by the GCMs. In the case of SPA the maximum intensity occurs during spring (March - May) and the minimum near the end of autumn (September - December). In the case of SSA, the maximum intensity occurs towards the end of winter and the beginning of spring, and the minimum during summer and autumn. However, in both cases, FGOALS-f3-L, MIROC6 and MIROC-ES2L underestimate the range of SLP values in which the SAA seasonal cycle oscillates.

On the other hand, the nonlinear interaction of the ENSO cycle with the annual cycle tends to frequency-lock the ENSO cycle. In the simplest case, the frequency is nonlinearly adjusted so that the phase matches the favorable season for each event (Neelin et al., 2000). Thus, ENSO is characterized by a strong boreal winter (Dec-Feb) peak for both warm (El Niño) and cold (La Niña) phases (Mitchell & Wallace, 1996; Neelin et al., 2000). As shown in Figure 4 (bottom panels), this characteristic is reasonably depicted by most CMIP6 models, with maximum/minimum peaks in

December-February for positive/negative phases, except for INM-CM5-0, MIROC6 and MIROC-ES2L with minimum peaks in October, September and June respectively during La Niña events.

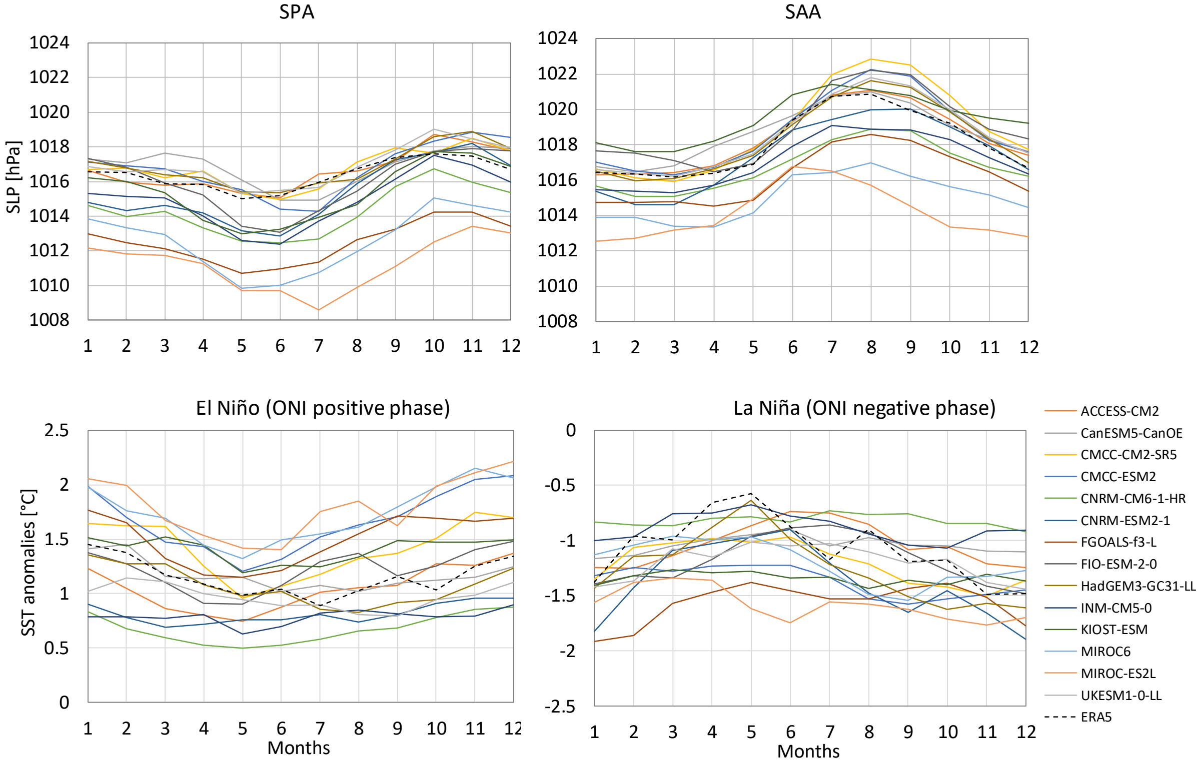

Figure 4. Seasonal cycle of SPA, SAA (considering SLP monthly mean values of the anticyclone center, without removing the seasonal cycle), El Niño (considering ONI positive phase) and La Niña (considering ONI negative phase) during 1980-2014.

As shown in Figure 5, both SPA and SAA indices show higher periodicity on the intra-annual scale, while SPA also peaked between 2 – 7 years, with significant peaks for FGOALS-f3-L, KIOST-ESM, MIROC-ES2L and ERA5 around 3 years, and for CMCC-ESM2, FGOALS-f3-L, MIROC6 and MIROC-ES2L around 5 years. In the case of the ONI index, the GCMs present a wide range of variability with spectral peaks within the range of 2 to 7 years. In this case, the MIROC-ES2L and FGOALS-f3-L models present greater regularity in periods of around 5 and 3 years respectively, CMCC-ESM2, KIOST-ESM, MIROC6 also present a high periodicity between 2.5

and 5 years. On the other hand, the behavior of the AAO index shows a higher periodicity mainly on the intra-annual scale with maximum peaks for HadGEM3-GC31-LL and UKESM1-0-LL in 5 months. Power peaks are also observed between 1 and 2 years, while FGOALS-f3-L, shows a peak around 5 years. Figure S1 of the supplementary material shows the superior limit of the red noise spectrum at a 95% confidence interval (Wilks, 2006) for each index simulated from CMIP6 models, in order to discard possible non-significant peaks.

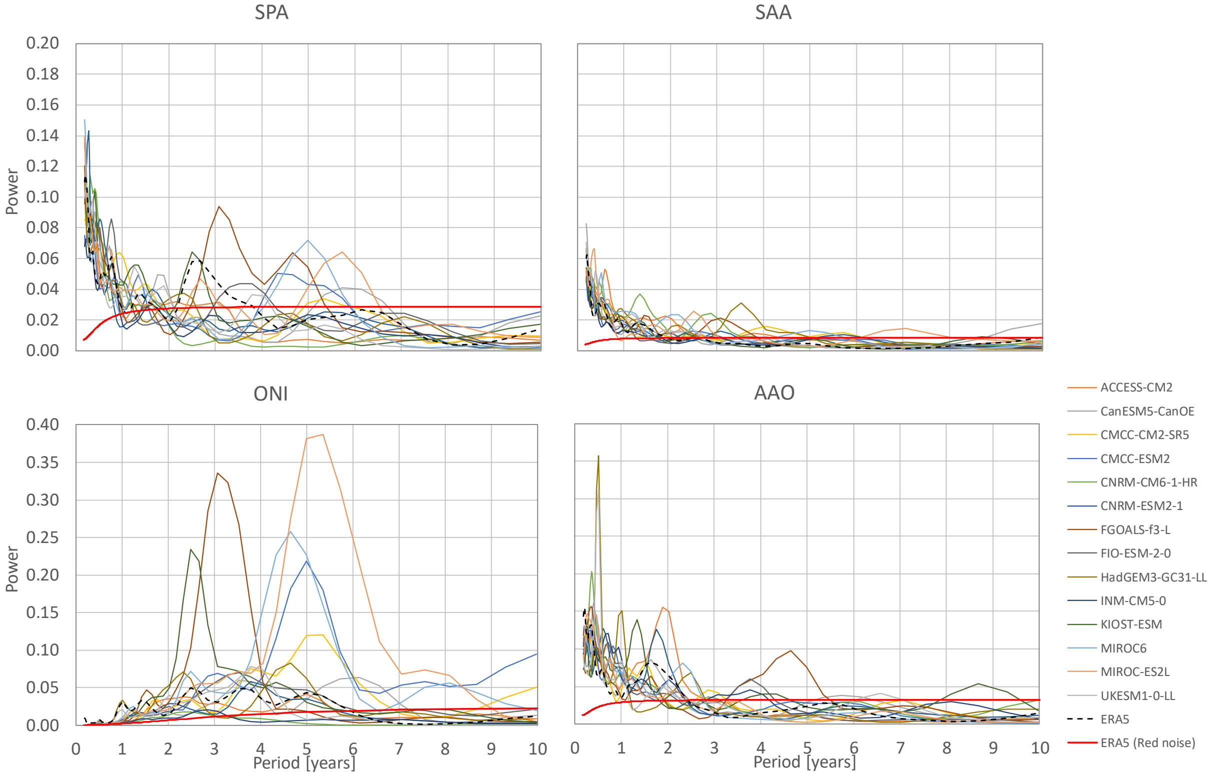

Figure 5. Spectral power curves of the Wavelet analysis for the SPA, SAA, ONI and AAO indices during 1980-2014. Red line represents the superior limit of red noise spectrum for ERA5 at a 95% confidence interval.

The spatial footprints of the selected atmospheric patterns over the SST and SLP fields obtained for each GCM (please see Figures S2 to S5 of the supplementary material) mostly showed similarities with those obtained from the ERA5 reanalysis, especially for SPA and SAA, although CNMR-CM6-1-HR does not show the negative relationship between SPA and SST over Equatorial

Pacific, as the rest of the models do. It is worth highlighting, both in the case of ONI and AAO, the models that presented the greatest similarities with the reanalysis: ACCESS-CM2, CanESM5-CanOE and FGOALS-f3-L, although the latter showed several differences in the previous tests. El Niño events are often stronger than La Niña events, this asymmetry is an intrinsic nonlinear characteristic of ENSO (An & Jin, 2004). Extreme El Niño events strongly enhance the overall ENSO asymmetry with their large amplitude in the eastern Pacific indeed intensifying and shifting the El Niño signals eastward relative to those of La Niña (Srinivas et al., 2024). Therefore, we also evaluate El Niño and La Niña signals on SST field separately. As shown in Figure S6 and Figure S7 of the supplementary material, except for CNMR-CM6-1-HR, CNMR-ESM2-1, INM-CM5-0, MIROC6 and MIROC-ES2L, most CMIP6 models (and ERA5 for reference) reasonably reproduce the asymmetry between El Niño and La Niña.

3.2. EOF analysis and relationship with the atmospheric patterns.

In the EOF analysis for the WS100 anomalies, the first three PCs were selected. The total variance accumulated by these three PCs was ~78.0% (average from all models accumulated variance by the three first PCs); starting from PC4 the explained variance was less than ~5%. The results for each subregion show that for REG1 the total explained variance was ~80.5% (PC1: 59.1%, PC2: 13.9% and PC3: 7.6%), for REG2 the total variance reaches ~70.7% (PC1: 43.9%, PC2: 17.1% and PC3: 9.7%) and for REG3 the total variance was ~82.8% (PC1: 52.2%, PC2: 22.8% and PC3: 7.9%).

Table 2 summarizes the most significant results of the correlations between the PCs and the analyzed indices, PC3 (not shown) presented very low or non-significant correlations in most cases and since the variance explained by this component was on average less than 10%, it was decided that it would not be considered for the rest of the analyses. It is important to note that the values shown in Table 2 as well as in Table 3 represent the magnitude of the correlations, while the corresponding EOF maps show the signal of the correlations.

Table 2. Magnitude of monthly (MON) and seasonal correlations (summer: DJF, winter: JJA) between a) SAA index and PC1 for REG1, and b) AAO index and PC2 for REG3. (Values highlighted in bold show a significant correlation at a 95% confidence interval).

A. REG1 PC1 vs. SAA

MODEL	MON	DJF	JJA
ERA5	**0.45**	**0.32**	**0.44**
ACCESS-CM2	**0.41**	0.06	**0.42**
CanESM5-CanOE	**0.55**	0.09	**0.49**
CMCC-CM2-SR5	**0.49**	0.12	**0.23**
CMCC-ESM2	**0.53**	**0.40**	0.19
CNRM-CM6-1-HR	**0.42**	0.13	**0.26**
CNRM-ESM2-1	**0.40**	**0.21**	**0.22**
FGOALS-f3-L	**0.44**	0.12	**0.33**
FIO-ESM-2-0	**0.50**	**0.22**	**0.28**
HadGEM3-GC31-LL	**0.18**	**0.20**	**0.50**
INM-CM5-0	**0.39**	**0.46**	**0.31**
KIOST-ESM	**0.39**	**0.25**	**0.24**
MIROC6	**0.38**	0.15	**0.39**
MIROC-ES2L	**0.31**	0.13	**0.54**
UKESM1-0-LL	**0.14**	0.12	**0.44**

B. REG3 PC2 vs. AAO

MODEL	MON	DJF	JJA
ERA5	**0.44**	**0.40**	**0.26**
ACCESS-CM2	**0.46**	0.51	**0.42**
CanESM5-CanOE	**0.39**	0.50	**0.22**
CMCC-CM2-SR5	**0.23**	0.05	**0.22**
CMCC-ESM2	**0.25**	**0.03**	0.25
CNRM-CM6-1-HR	**0.31**	0.47	**0.39**
CNRM-ESM2-1	**0.31**	**0.49**	**0.23**
FGOALS-f3-L	**0.34**	0.41	**0.35**
FIO-ESM-2-0	**0.27**	**0.10**	**0.30**
HadGEM3-GC31-LL	**0.33**	**0.52**	**0.12**
INM-CM5-0	**0.36**	**0.28**	**0.35**
KIOST-ESM	**0.26**	**0.34**	**0.16**
MIROC6	**0.27**	0.37	**0.21**
MIROC-ES2L	**0.30**	0.48	**0.13**
UKESM1-0-LL	**0.33**	0.50	**0.19**

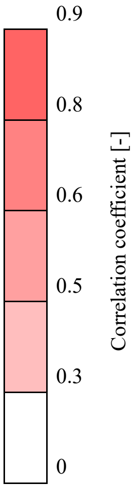

In the case of the SAA, significant correlations are mostly observed between the SAA index and the PC1 for REG1 (Table 2a). Higher correlations occur in the monthly series (CMIP6 reached 0.55, ERA5: 0.45) and stronger in winter than in summer. As seen in Figure 6, the correlations are positive throughout the region during the winter, while in the summer they are positive in the direction of the coast and become null or even negative in some cases towards the interior of the continent. This means that an increase of SAA intensity causes an increase of WS100 over northeast Brazil and vice versa. Although, some models present correlations of magnitude 0.3 - 0.53 between the SAA index and PC2 in and winter, however, ERA5 did not show such relationship (Table S1 of the supplementary material).

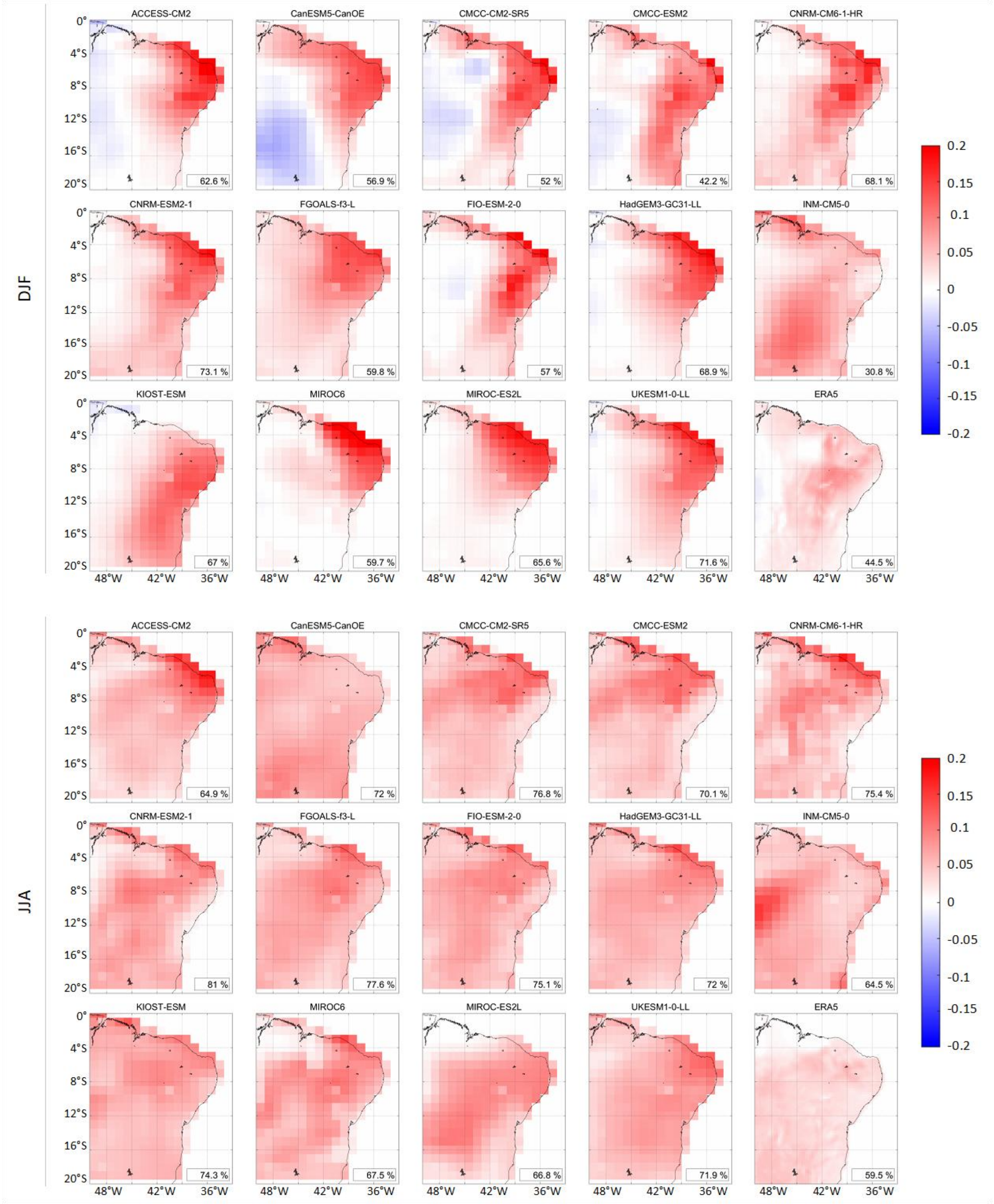

Figure 6. EOF1 maps corresponding to PC1 for REG1 in summer (upper set: DJF) and winter (lower set: JJA) during 1980-2014. The percentages shown in the lower right corners represent the variance explained in each case.

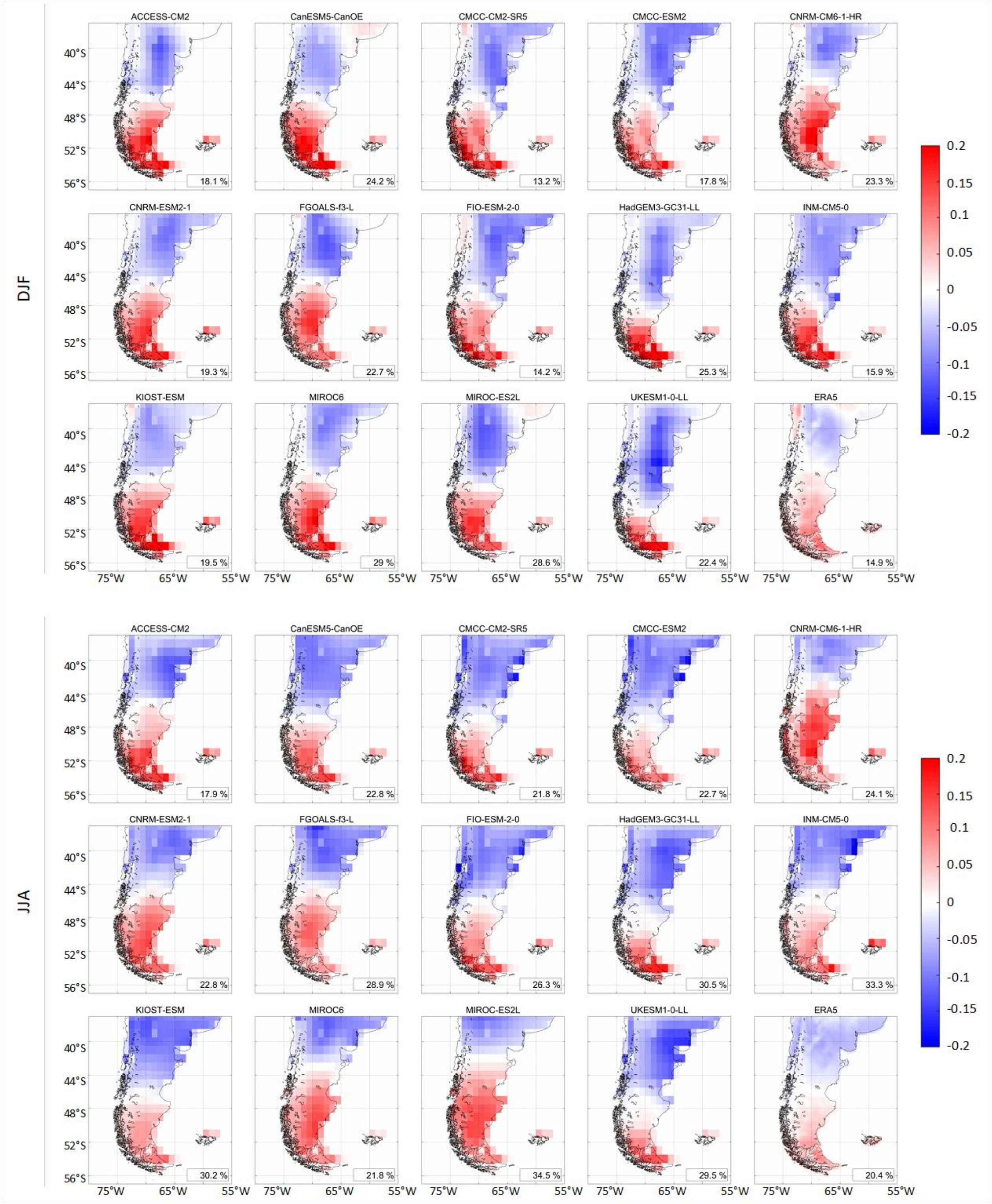

Figure 7. EOF2 maps corresponding to PC2 for REG3 in summer (upper set) and winter (lower set) during 1980-2014. The percentages shown in the lower right corners represent the variance explained in each case.

In the case of AAO, a consistency can be seen in the magnitude of the correlations between the AAO index and PC2 for REG3 (Table 2c). Correlations are stronger during summer (CMIP6 reached 0.52, except for CMCC-CM2-SR5, CMCC-ESM2 and FIO-ESM-2 -0 which were non-significant, ERA5: 0.4) than during winter (CMIP6 reached 0.42, except HadGEM3-GC31-LL, KIOST-ESM, MIROC-ES2L and UKESM1-0-LL, ERA5: 0.26). Meanwhile, for the monthly series the correlations were of magnitude 0.23 - 0.46 for CMIP6 models and 0.44 for ERA5. As can be seen in Figure 7, for both summer and winter there is a dipole with positive correlations towards the southern tip of Patagonia and negative correlations north of approximately 45° S. This means that the positive phase of the AAO causes an increase of WS100 over the southern tip of Patagonia, and a decrease around north of 45° S, the opposite occurs during the negative phase of AAO.

In the case of ENSO, GCMs did not show an evident consensus in the correlations between ONI index and PCs in the subregions analyzed (shown in the supplementary material). However, correlations that reach 0.45 magnitude in some cases are seen between ONI index and PC1 for REG2 in both monthly and summer series. For REG1, in some cases, correlations were found between ONI index and PC2 in the monthly series and reached 0.55 of magnitude only a few cases in winter, although ERA5 showed a weak (< 0.3) or non-significant correlation.

The SPA intensity did not present significant correlations for the subregions analyzed, except for ERA5, which suggests a relationship of magnitude 0.37 between SPA index and PC1 for REG2 in winter. Table S1 of the supplementary material shows the magnitude of all correlations between the selected atmospheric patterns and PCs for each subregion.

3.3. Relationship with the SLP field

PC1 for REG2 and REG3 did not present significant correlations consistent with the atmospheric patterns analyzed; however, in all cases this component (PC1) explains most of the variance of WS100, so its relationship with the SLP field was studied to understand what mechanisms this mode of wind variability responds to. Figure 8 shows mostly weak correlations for REG2 in monthly and summer series, while during winter it shows positive correlations associated with pressure anomalies over the South Pacific between approximately 15° - 50° S, within the eastern portion of the area of greatest influence of SPA. For REG3 a negative correlation pattern with the SLP anomalies is observed in the area between 40° - 75° S and 30° - 110° W. A dipole of correlations with the WS100 field is observed within the above-mentioned area, with positive correlations over Patagonia and the adjacent seas, and negative values over the Drake Passage and the areas surrounding the Antarctic Peninsula.

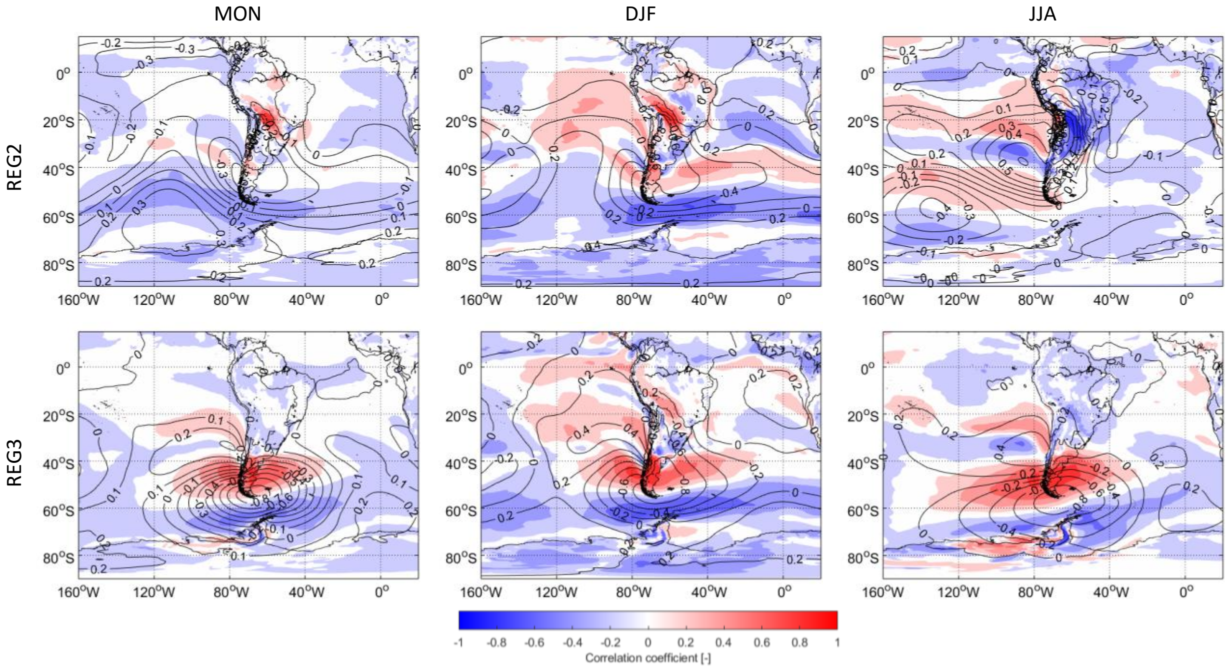

Figure 8. Monthly (MON) and seasonal correlations (summer: DJF, winter: JJA) between. PC1 and the SLP (contours) and WS100 (colors) fields for REG2 (upper panels) and REG3 (lower panels). The values correspond to the Pearson correlation coefficients at a 95% confidence interval. Wind speed at 100 m and SLP during 1980-2014 retrieved from the ERA5 reanalysis.

To investigate what causes these correlation patterns, a synoptic analysis was performed taking the lower 10% and the upper 10% of the PC1 series that corresponds to the months with minimum and maximum WS100 values respectively. Then, the days with negative/positive anomalies with regards to the historical average (1980-2014) that correspond to the lower/upper range were taken, and the mean SLP field was calculated for these cases.

In the case of REG2, Figure 9a shows that for days with minimum values of WS100, the intensity of the SPA is lower compared to that of days with maximum values of WS100 (Figure 9b). The most significant variations of WS100 are observed over central and northern Argentina with anomalies of magnitude up to 1 m/s, both for the days of minimums (Figure 9c) as well as for the days of maximums (Figure 9d). Some correspondence is also observed in the sign of the WS100 anomalies within REG2 and the SLP anomalies within the area of greatest influence of the SPA, however, the magnitude of the anomalies in both fields is small (< 2.5 hPa) even when only extreme cases are being considered.

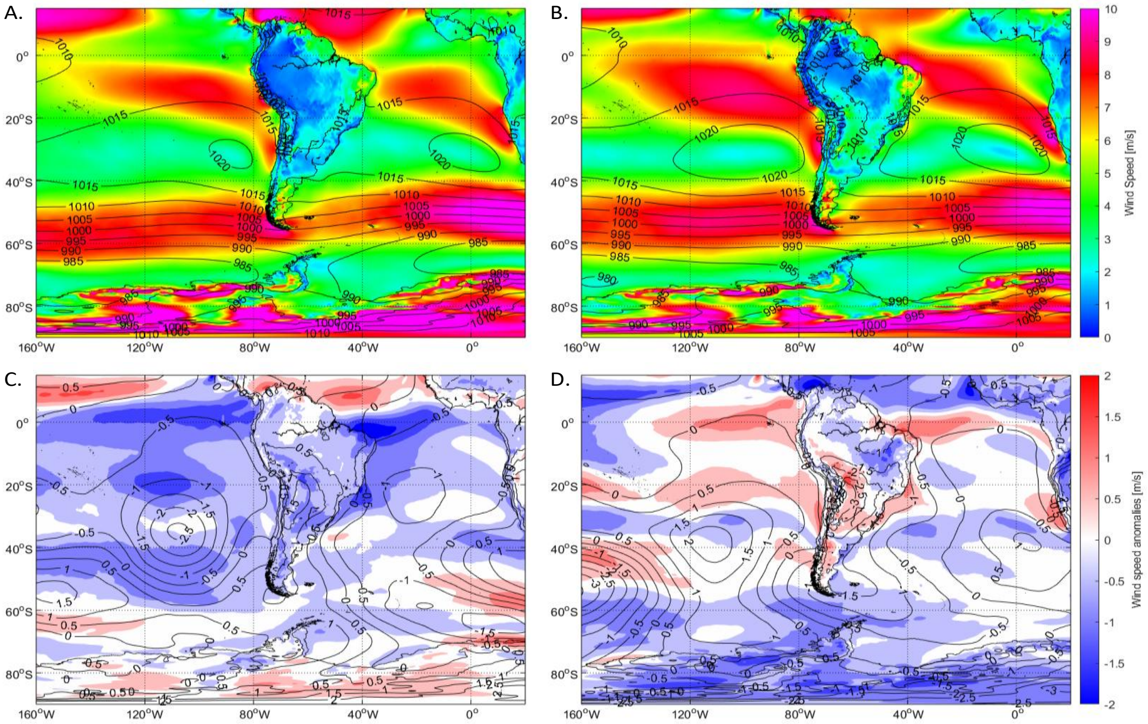

Figure 9. a) WS100 field (colors) and SLP (contours) that correspond to the lower 10% of the PC1 time series for REG2. b) same as before but corresponding to the top 10%. c) WS100 anomaly field (colors) and SLP anomalies (contours) that correspond to the lower 10% of the PC1 time series. d) same as before but corresponding to the top 10%. Wind speed at 100 m and SLP during 1980-2014 retrieved from the ERA5 reanalysis.

Therefore, it is likely that the relationship between SPA and WS100 for REG2 is only considerable in extreme cases and therefore the SPA index and PC1 for that region do not present a high correlation. The SPA intensity begins to increase in late winter to reach the maximum during spring, so it makes sense that moderate positive correlations are observed between the SPA index and PC1 in winter as mentioned in section 3.3. In fact, 73.8% of the WS100 higher values represented by PC1 occurred during spring, while 57.1% of the lowest WS100 values occurred in autumn, which has a certain relationship with the seasonal behavior of the SPA.

In the case of REG3, as shown in Figure 10a, for the days with minimum values of WS100, the SLP field shows a configuration with an anticyclonic curvature over the Drake Passage, which causes a more southerly shift of the westerlies flow in that area and a weakening of the wind over Patagonia. On the other hand, for the days with maximum values of WS100 (Figure 10b), a low-pressure center can be seen to the west of the Antarctic Peninsula. This, in combination with a greater intensity of the SPA makes the pressure gradient stronger over Patagonia and, therefore, the intensity of the westerlies over said region increases. Figure 10c and Figure 10d show the SLP and WS100 anomaly fields that correspond to days within the bottom 10% and top 10% of the WS100 series, respectively.

In both cases, a pattern of SLP anomalies centered in the Drake Passage is observed with a relationship opposite to the behavior of the WS100 anomalies over Patagonia and the adjacent seas, and to a lesser extent, a direct relationship with WS100 in the vicinity of the Antarctica Peninsula. That is, an increase in SLP in that area corresponds to a decrease of WS100 over Patagonia and its surroundings and a slight increase of WS100 in the vicinity of the Antarctic Peninsula (Figure 10c) and vice versa (Figure 10d). This pattern in the SLP anomaly field and its relationship with the WS100 anomalies is similar to the correlation pattern observed between the SLP field and PC1 for REG3. The occurrence of stronger or weaker winds related to this pattern did not present large seasonal differences, since the occurrence of minimum winds was 26.2% of the cases in summer and 21.4% in winter (autumn: 28.6%, spring: 23.8%). In the case of the strongest winds, 23.8% of the cases occurred in summer and 31% in winter (autumn: 14.3%, and spring: 31%).

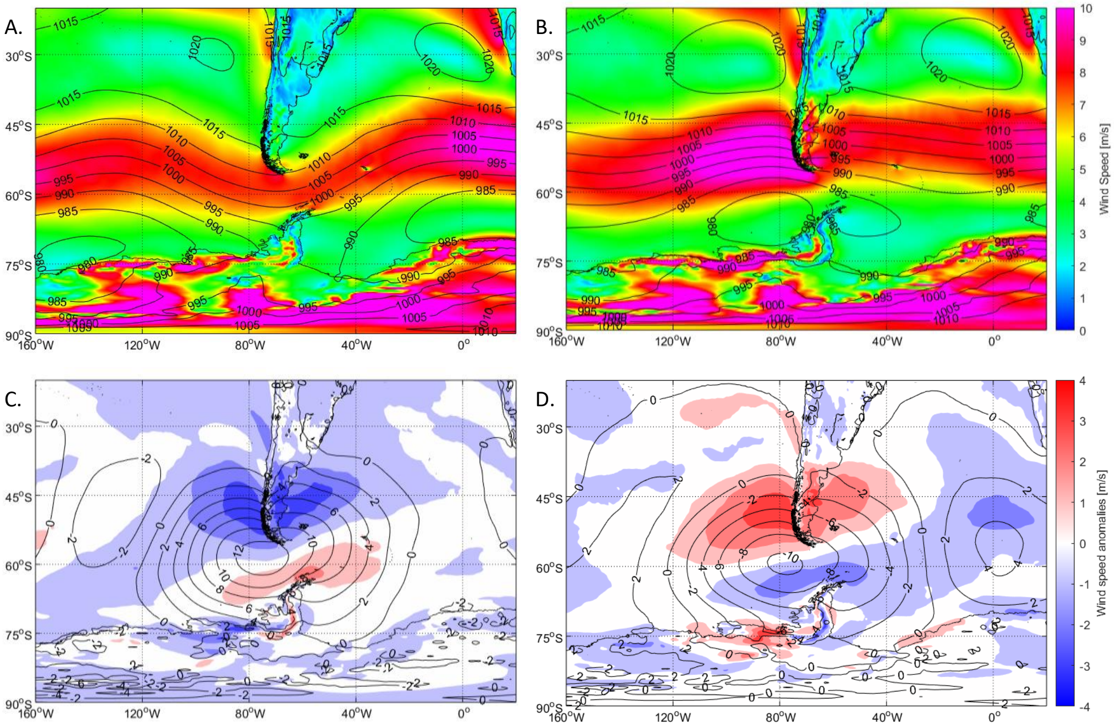

Figure 10. a) WS100 field (colors) and SLP (contours) that correspond to the lower 10% of the PC1 time series for REG3. b) same as before but corresponding to the top 10%. c) WS100 anomaly field (colors) and SLP anomalies (contours) that correspond to the lower 10% of the PC1 time series. d) same as before but corresponding to the top 10%. Wind speed at 100 m and SLP during 1980-2014 retrieved from the ERA5 reanalysis.

Based on the relationships found for REG3 between PC1 and the SLP and WS100 fields, we designed an index that we named PAT (Patagonia-Antarctic pattern) to measure the intensity of the SLP anomalies pattern associated with the behavior of PC1. This index is based on the SLP anomalies within the area delimited by 40° - 75° S, 30° - 110° W. Then, this index was calculated for each GCM, the seasonal cycle from PAT was removed and correlations with PC1 for REG3 were found. As Table 3 shows, in all cases the GCMs, as well as ERA5, evidence significant correlations both for the monthly series (CMIP6 reached 0.81, ERA5: 0.77), as well as for winter (CMIP6 reached 0.75, ERA5: 0.79) and summer (CMIP6 reached 0.83, ERA5: 0.61), which are negative over practically the entire REG3 (Figure 11). This means that the positive phase of the PAT index causes a decrease of WS100 over Patagonia, while WS100 increases during the negative phase of PAT.

Table 3. Monthly (MON) and seasonal correlations (summer: DJF, winter: JJA) of a) PAT index and b) SPA index with the PC1 that results from the EOF decomposition for REG3. (Values highlighted in bold show a significant correlation at a 95% confidence interval).

A. REG3 PC1 vs. PAT

MODEL	MON	DJF	JJA
ERA5	**0.77**	**0.61**	**0.79**
ACCESS-CM2	**0.76**	**0.65**	**0.71**
CanESM5-CanOE	**0.81**	**0.66**	**0.75**
CMCC-CM2-SR5	**0.76**	**0.67**	**0.66**
CMCC-ESM2	**0.75**	**0.64**	**0.68**
CNRM-CM6-1-HR	**0.67**	**0.57**	**0.42**
CNRM-ESM2-1	**0.68**	**0.68**	**0.64**
FGOALS-f3-L	**0.72**	**0.75**	**0.67**
FIO-ESM-2-0	**0.75**	**0.68**	**0.66**
HadGEM3-GC31-LL	**0.49**	**0.66**	**0.63**
INM-CM5-0	**0.77**	**0.83**	**0.74**
KIOST-ESM	**0.73**	**0.58**	**0.69**
MIROC6	**0.73**	**0.55**	**0.71**
MIROC-ES2L	**0.65**	**0.62**	**0.52**
UKESM1-0-LL	**0.49**	**0.56**	**0.60**

B. REG3 (Chilean side) PC1 vs. SPA

MODEL	MO	DJF	JJA
ERA5	**0.12**	**0.17**	**0.38**
ACCESS-CM2	**0.13**	**0.34**	**0.47**
CanESM5-CanOE	0.05	0.09	**0.39**
CMCC-CM2-SR5	0.09	**0.15**	**0.35**
CMCC-ESM2	**0.22**	0.03	**0.40**
CNRM-CM6-1-HR	0.02	**0.39**	**0.12**
CNRM-ESM2-1	0.09	**0.30**	**0.16**
FGOALS-f3-L	0.03	**0.32**	**0.28**
FIO-ESM-2-0	0.08	**0.19**	**0.40**
HadGEM3-GC31-LL	**0.14**	**0.35**	**0.49**
INM-CM5-0	0.08	**0.31**	**0.34**
KIOST-ESM	0.01	**0.35**	**0.35**
MIROC6	**0.11**	**0.26**	**0.31**
MIROC-ES2L	0.01	**0.19**	**0.14**
UKESM1-0-LL	**0.12**	**0.40**	**0.23**

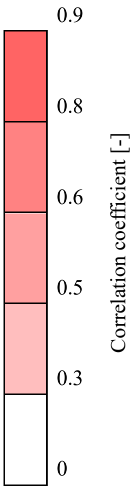

Also, given the Andes represents an obstacle to the tropospheric flow over REG2 and REG3, we also analyzed Chilean and Argentinean sides of these regions separately. We computed the new EOFs and calculated the correlations with the indices. The Chilean sides were correlated with SPA and ONI, while the Argentinean sides were correlated with SAA and ONI. As shown in Table 3, in the case of the Chilean side of REG3 correlations with SPA increased a little and appear more clearly particularly in winter with magnitudes up to 0.49 in some cases. These correlations are positive (Figure 12) which means that an increase in WS100 over Chilean side of Patagonia is related to a strengthening in SPA intensity, particularly for southern extreme. While for Chilean side of REG2 correlations are still low in most cases. Correlations with ONI remain low in most cases for all the regions, and correlations with SAA for the Argentinean sides in most cases are still very low. All correlations regarding this analysis are shown in Table S2 of the supplementary material. Figure 12 summarizes the EOFs corresponding to cases when significant relationships with climate indices were found. for ERA5 reanalysis as reference.

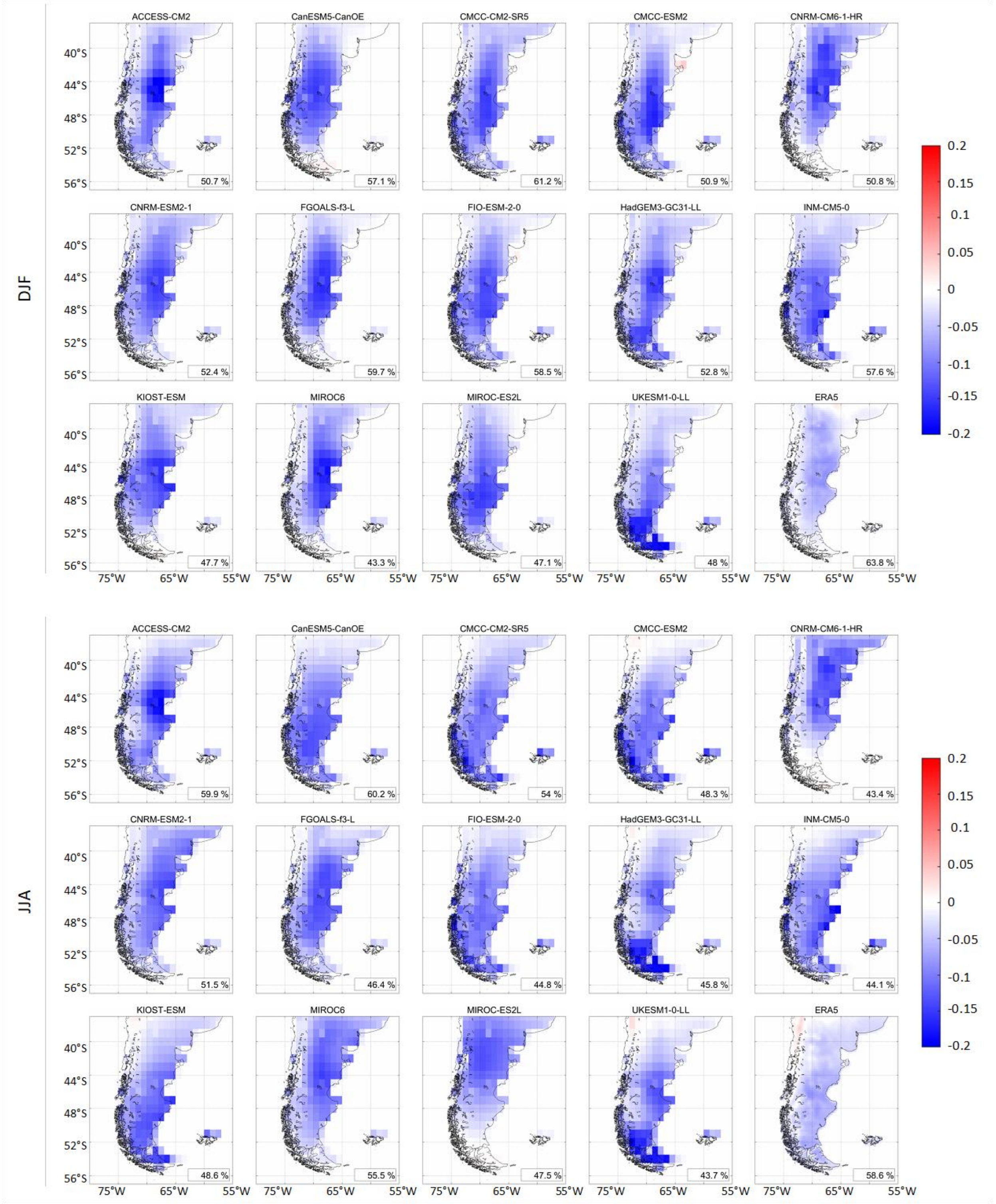

Figure 11. EOF1 maps corresponding to PC1 for REG3 in summer (upper set) and winter (lower set) during 1980-2014. The percentages shown in the lower right corners represent the variance explained in each case.

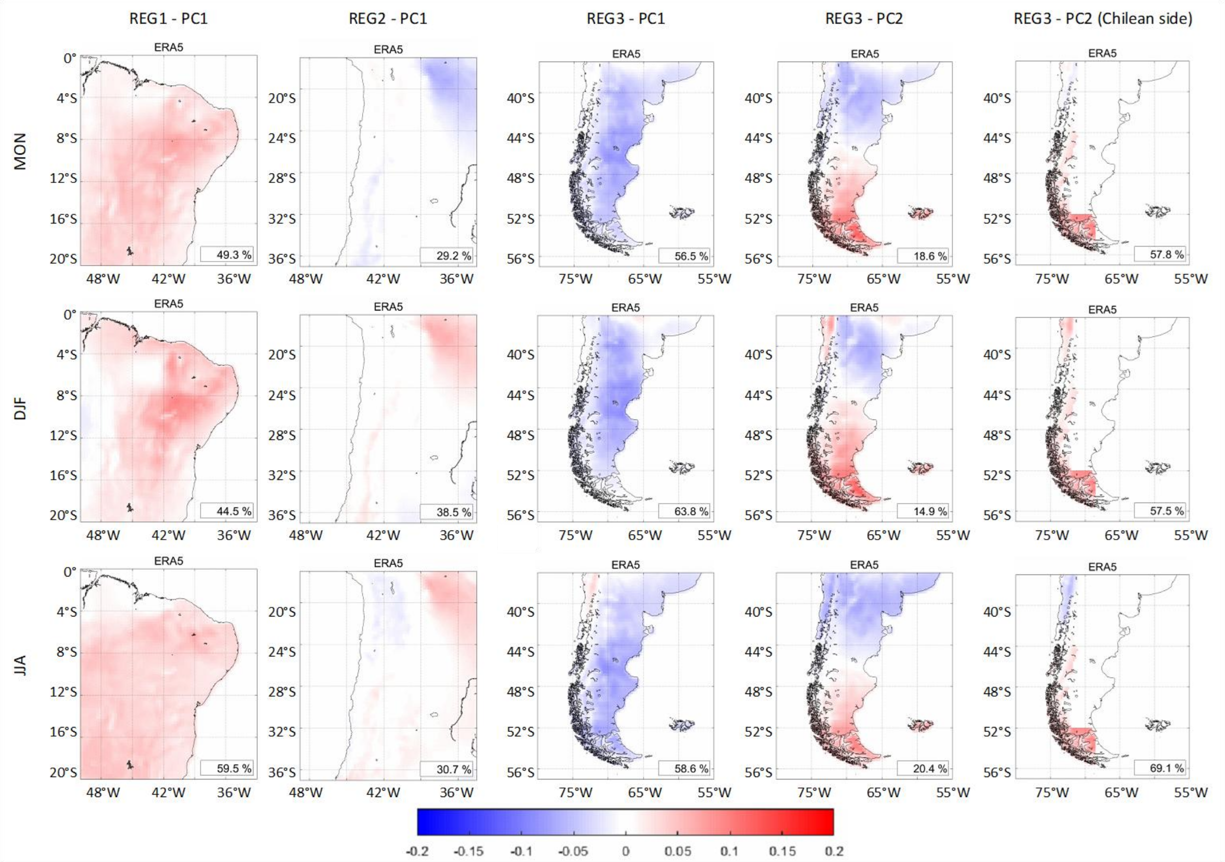

Figure 12. Monthly (MON), summer (DJF) and winter (JJA) EOF maps and PCs explained variance (percentages shown in the lower right corners) for ERA5 reanalysis corresponding to cases when significant relationships with climate indices were found.

Finally, the correlations of the SPA, SAA and PAT indices with the ONI and AAO indices were calculated to study the interrelationships between them. Table 4 shows positive correlations between SPA and AAO, with slightly higher values during the summer. SPA also presents negative correlations with ONI, which become stronger in winter. SAA presents positive correlations with the AAO mainly during the summer. In the case of PAT, the correlations were mostly low or non-significant, although in some cases positive correlations were seen with ONI in summer and negative correlations with AAO in winter.

Table 4. Monthly (MON) and seasonal correlations (summer: DJF, winter: JJA) of the SPA, SAA and PAT indices with the ONI and AAO indices. (Values highlighted in bold show a significant correlation at a 95% confidence interval).

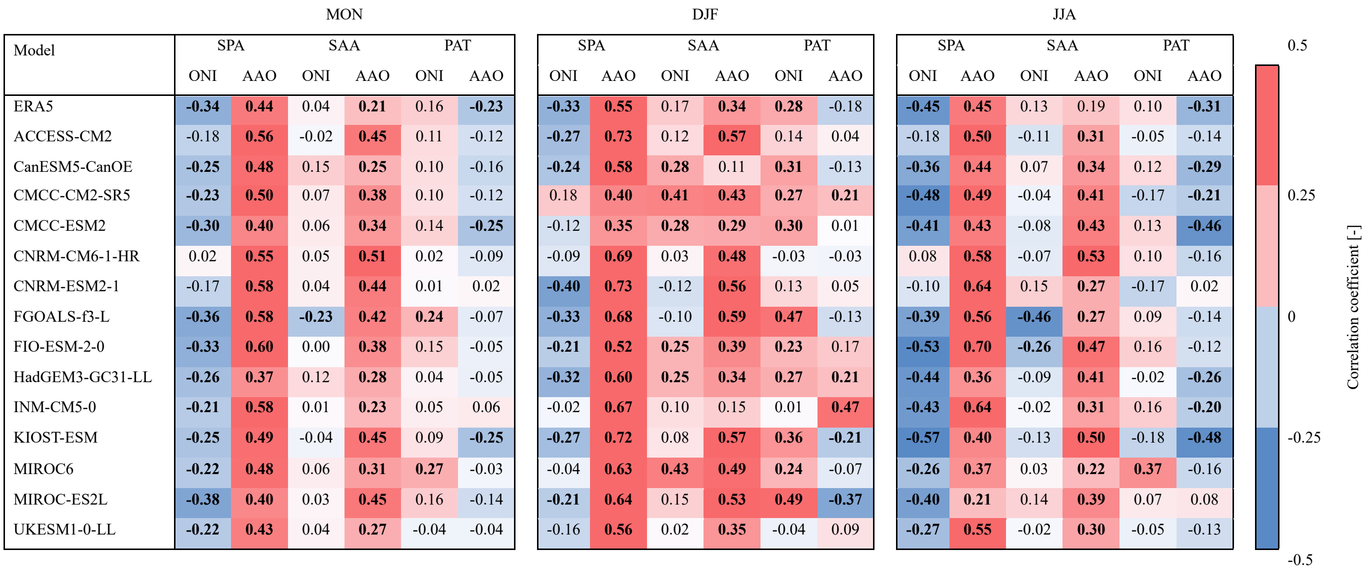

Model	MON						DJF						JJA					
	SPA		SAA		PAT		SPA		SAA		PAT		SPA		SAA		PAT	
	ONI	AAO	ONI	AAO	ONI	AAO	ONI	AAO	ONI	AAO	ONI	AAO	ONI	AAO	ONI	AAO	ONI	AAO
ERA5	**-0.34**	**0.44**	0.04	**0.21**	0.16	**-0.23**	**-0.33**	**0.55**	0.17	**0.34**	**0.28**	-0.18	**-0.45**	**0.45**	0.13	0.19	0.10	**-0.31**
ACCESS-CM2	-0.18	**0.56**	-0.02	**0.45**	0.11	-0.12	**-0.27**	**0.73**	0.12	**0.57**	0.14	0.04	-0.18	**0.50**	-0.11	**0.31**	-0.05	-0.14
CanESM5-CanOE	**-0.25**	**0.48**	0.15	**0.25**	0.10	-0.16	**-0.24**	**0.58**	**0.28**	0.11	**0.31**	-0.13	**-0.36**	**0.44**	0.07	**0.34**	0.12	**-0.29**
CMCC-CM2-SR5	**-0.23**	**0.50**	0.07	**0.38**	0.10	-0.12	0.18	**0.40**	**0.41**	**0.43**	**0.27**	**0.21**	**-0.48**	**0.49**	-0.04	**0.41**	-0.17	**-0.21**
CMCC-ESM2	**-0.30**	**0.40**	0.06	**0.34**	0.14	**-0.25**	-0.12	**0.35**	**0.28**	**0.29**	**0.30**	0.01	**-0.41**	**0.43**	-0.08	**0.43**	0.13	**-0.46**
CNRM-CM6-1-HR	0.02	**0.55**	0.05	**0.51**	0.02	-0.09	-0.09	**0.69**	0.03	**0.48**	-0.03	-0.03	0.08	**0.58**	-0.07	**0.53**	0.10	-0.16
CNRM-ESM2-1	-0.17	**0.58**	0.04	**0.44**	0.01	0.02	**-0.40**	**0.73**	-0.12	**0.56**	0.13	0.05	-0.10	**0.64**	0.15	**0.27**	-0.17	0.02
FGOALS-f3-L	**-0.36**	**0.58**	**-0.23**	**0.42**	**0.24**	-0.07	**-0.33**	**0.68**	-0.10	**0.59**	**0.47**	-0.13	**-0.39**	**0.56**	**-0.46**	**0.27**	0.09	-0.14
FIO-ESM-2-0	**-0.33**	**0.60**	0.00	**0.38**	0.15	-0.05	**-0.21**	**0.52**	**0.25**	**0.39**	**0.23**	0.17	**-0.53**	**0.70**	**-0.26**	**0.47**	0.16	-0.12
HadGEM3-GC31-LL	**-0.26**	**0.37**	0.12	**0.28**	0.04	-0.05	**-0.32**	**0.60**	**0.25**	**0.34**	**0.27**	**0.21**	**-0.44**	**0.36**	-0.09	**0.41**	-0.02	**-0.26**
INM-CM5-0	**-0.21**	**0.58**	0.01	**0.23**	0.05	0.06	-0.02	**0.67**	0.10	0.15	0.01	**0.47**	**-0.43**	**0.64**	-0.02	**0.31**	0.16	**-0.20**
KIOST-ESM	**-0.25**	**0.49**	-0.04	**0.45**	0.09	**-0.25**	**-0.27**	**0.72**	0.08	**0.57**	**0.36**	**-0.21**	**-0.57**	**0.40**	-0.13	**0.50**	-0.18	**-0.48**
MIROC6	**-0.22**	**0.48**	0.06	**0.31**	**0.27**	-0.03	-0.04	**0.63**	**0.43**	**0.49**	**0.24**	-0.07	**-0.26**	**0.37**	0.03	**0.22**	**0.37**	-0.16
MIROC-ES2L	**-0.38**	**0.40**	0.03	**0.45**	0.16	-0.14	**-0.21**	**0.64**	0.15	**0.53**	**0.49**	**-0.37**	**-0.40**	**0.21**	0.14	**0.39**	0.07	0.08
UKESM1-0-LL	**-0.22**	**0.43**	0.04	**0.27**	-0.04	-0.04	-0.16	**0.56**	0.02	**0.35**	-0.04	0.09	**-0.27**	**0.55**	-0.02	**0.30**	-0.05	-0.13

4. Discussion

Through our research we found that, most CMIP6 models reasonable reflect the main characteristics of SPA, SAA, ENSO and AAO with some discrepancies. In the case of the semi-permanent patterns related to SPA and SAA, CMIP6 models were able to represent reasonably the amplitude of the oscillations, the behavior of the seasonal cycle and the spatial footprints of these atmospheric patterns with slight differences. While all CMIP6 models can produce quasi-oscillatory behavior clearly corresponding to ENSO, there is a wide range of variability with spectral peaks in the range of 2 to 7 years, which is consistent with Fredriksen et al. (2020), however the they also reasonable depict the asymmetry between STT teleconnections related to El Niño and La Niña, and the phase-locking to seasonal cycle of both phases. The distribution of the ONI and AAO indices time series, the periodicity and the spatial footprints of these atmospheric patterns shown by GCMs coincide with each other in most cases and with those shown by ERA5, with some discrepancies.

According to the literature, the amplitude and the spatial structure of different types of ENSO are better depicted in CMIP6 models compared to their previous versions in CMIP5 (Hou & Tang, 2022). Some of the CMIP6 models reproduce the global structures of the surface temperature and SLP anomalies quite accurately between opposite phases of ENSO, as previously determined from observational data and reanalysis (Serykh & Sonechkin, 2024). However, they simulate more intense and spatially extended ENSO patterns and have issues in capturing the correct seasonality, persistence and frequency (Vaittinada et al., 2023). According to our results, it is worth pointing out the cases of ACCESS-CM2, CanESM5-CanOE, CMCC-CM2-SR5 and CMCC-ESM2 which were capable of passing all the tests performed; they largely represent the behavior of the analyzed atmospheric patterns and their relationships with the WS100 field. Quite the opposite, INM-CM5-0, HadGEM3-GC31-LL, MIROC6 and MIROC-ES2L presented the most failures in the tests performed.

The performance of the GCMs from CMIP6 to represent wind speed behavior has been studied by numerous authors for different regions (Wu et al., 2020; Qian & Zhang, 2021; Akinsanola et al., 2021; Carvalho et al., 2021), so that analysis was not performed in our research. Specifically in the case of South America, de Souza Ferreira et al. (2024) points out that CMIP6 GCMs underestimate the wind intensity in regions like northeastern Brazil and Argentine Patagonia, also in the central portion of South America south of 10° S during austral autumn and winter and over Uruguay during spring. However, as the authors mention, the CMIP6 models adequately simulates the wind speed seasonal variability in the Amazonia region and the higher magnitudes in sectors such as northern Venezuela, Suriname, Guyanas, and extreme northern Brazil.

Historical data from observations in South America is very scarce in the case of 100 m wind. Nevertheless, we gathered the available observational datasets of near-surface wind speed to validate near-surface wind speed from CMIP6 models using the root mean square error (RMSE). As shown in Figure S8 of the supplementary material, Northeast Brazil region has lower values of RMSE, under 2.5 m/s in most cases or even near 0 m/s. On the other hand, Chile has higher RMSE values, above 2.5 m/s in most cases, reaching almost 5 m/s over Northern and Southern extremes of the country. Although the stations used are scarce, not well space-distributed and the coverage period is not enough for a proper validation these results show that simulated wind speed from

CMIP6 models cannot accurately reproduce real wind speed in areas with complex as it is the case of Chile, while for Northeast Brazil, a less complex orography region, the simulations have better performance. Although the GCMs from CMIP6 have greatly improved their simulation capabilities in the historical period when compared to those of CMIP5 (Qian & Zhang, 2021), with more complete physical processes than their predecessors, their performance in capturing local and regional forcing remains poor, especially in regions with complex terrain (Wu et al., 2020).

4.1. Influence of the atmospheric patterns on WS100 behavior

The SAA turned out to be the dominant mode of WS100 variability over northeast Brazil (REG1) and the only atmospheric pattern for which a significant relationship was found for that region. This was found to be a direct relationship and stronger during winter. This means that as the SAA intensity increases, WS100 increases as well over northeast Brazil and vice versa. The variability of the SAA affects the southern tropical Atlantic basin through wind variability in the region, and its seasonal cycle is controlled mainly by convective heat sources over South America and southern Africa, and by the interaction between the orography with the eastern trade winds and the westerly mid-latitude winds (Rodwell & Hoskins, 2001; Miyasaka & Nakamura, 2010).

These fundamental mechanisms lead to a SAA that is noticeably stronger during the austral winter rather than during the austral summer (Cabos et al., 2017), which coincides with our results and explains the positive relationship found between the SAA intensity and PC1 for REG1; PC1 concentrates most of the variance of the WS100 field over northeast Brazil and is therefore its main modulator. The influence of the SAA on the behavior of WS100 is important, especially in winter and spring. As de Souza Ferreira et al. (2024) points out there are suitable conditions for wind power generation in much of northeast Brazil during austral winter and spring.

According to our results, the variability of WS100 over Patagonia (REG3) is mainly negatively correlated to a pattern of SLP anomalies within the region between 40° - 75° S and 30° - 110° W, named PAT (Patagonia – Antarctic pattern) in this study, which covers the section of the westerlies belt close to Patagonia. South of 40° S, the westerly flow prevails at low levels throughout the year

(Garreaud et al., 2009), so the variability of the wind in Patagonia responds fundamentally to variations in the abovementioned flow. The region where the pattern we found is centered, is an exchange zone where both mid-latitude and low-latitude systems influence the westerly flow.

We found that WS100 increases when a low-pressure center occurs west of the Antarctic Peninsula, which together with a greater intensity of the SPA causes an increase in the pressure gradient and the intensity of the westerlies over the Patagonia region; this situation corresponds to a negative PAT index. On the other hand, when the SLP field shows a configuration with an anticyclonic curvature over the Drake Passage (showing a positive PAT index), the westerlies move further south in that area, which causes a weakening of WS100 over Patagonia.

In second place, we found that the behavior of WS100 over Patagonia is further modulated by AAO. This relationship becomes evident for PC2 for REG3, and it is stronger during summer with a negative signal over central Argentina, which coincides with the results of Bianchi et al. (2022), while it takes a positive signal in the extreme south (45° S) of Patagonia (Bianchi et al., 2017). The positive phase of the AAO is associated with an increase in surface pressure in mid-latitudes and a decrease towards Antarctica and a strengthening and shift towards the pole of the westerlies (Garreaud et al., 2009). This explains the increase of WS100 in the extreme south of Patagonia during the positive phase of the AAO and it is weakening further north over central Argentina. A reverse behavior occurs during the negative phase of the AAO.

According to our results, the AAO presents positive correlations with the intensity of SPA and SAA, which is more evident in the seasonal series, especially during summer in both cases. This means that the strengthening of both SPA and SAA coincides with the positive phase of the AAO. This direct relationship makes sense, given that the strengthening of both SPA and SAA, or their shifting southward during summer, causes an increase in surface pressure gradient in mid-latitudes and the intensification and shift of the westerlies towards the pole, which also coincides with the positive phase of the AAO.

ENSO did not show any clear influence on WS100 in the subregions analyzed. However, regarding REG1 (northeast Brazil), a few significant correlations were found between ONI and PC2 in the monthly series, and mainly in winter, although in the latter case the ERA5 did not show a significant correlation. As Colberg et al. (2004) point out, during La Niña (negative phase of ENSO), the SAA strengthens, and that teleconnection could explain the influence of ENSO over northeast Brazil, given that SAA is the main WS100 modulator over this region. However, according to the literature and to our results, the influence of ENSO on the SAA is still not clear and several authors point out that ENSO does not have an important role in the variability of the SAA, or its influence is weak (Sterl & Hazeleger, 2003; Lübbecke et al., 2014).

Significant correlations were seen in a few cases between ONI and PC1 for REG2 (northern Chile and Argentina) slightly higher in summer. This makes sense, because as seen in Figure 4, both phases of ENSO peak in austral summer. On the other hand, ERA5 suggests that there is a relationship between the SPA intensity and WS100 in northern Chile and Argentina during winter, which makes sense since SPA intensifies during winter. Also, our results showed that ENSO has a negative correlation with the intensity of the SPA, so that the positive phase of ENSO coincides with a weakening of the SPA and vice versa.

This result coincides with Gómez-Fontealba et al. (2022), who points out that El Niño (positive phase of ENSO) causes a weakening of the SPA and Watts et al. (2017) discovered that the positive phase of ENSO reduces wind speed over central-northern Chile. Therefore, this suggests that there is a teleconnection between ENSO, SPA and WS100 over central-northern Chile. This makes sense, given that SPA variability is also negative related to SST variations in Equatorial Pacific (as shown in Figure 2 and Figure S2 of the supplementary material). Therefore, it is to be expected that this relationship will also manifest between SPA and ENSO, characterized by Equatorial Pacific SST variations, and ultimately it influences WS100 behavior over this region.

We also performed an extreme case analysis for WS100 that showed some relationship with the seasonal behavior of the SPA, with 73.8% of the total cases of maximum WS100 values in spring and 57.1% of the total cases of minimum WS100 values in autumn.

Given the Andes represents an obstacle to the tropospheric flow over REG2 and REG3, we also analyzed Chilean and Argentinean sides of these regions separately. We find that SPA has some positive influence on WS100 over Chilean side of REG3 and as we aforementioned, the SPA plays a role in the mechanisms that cause variations in the pressure gradient and the intensity of the westerlies over the Patagonia region. On the other hand, for REG2 the correlations of WS100 with SPA remain low, even for Chilean side. A smaller-scale study over this region with complex physical geographic characteristics would perhaps provide greater insight into the influence of climatic oscillations on the behavior of WS100.

5. Conclusions

In this study, the influence of the SPA, SAA, ENSO and AAO atmospheric patterns on the behavior of the wind resource in South America was analyzed using the historical simulations (1980-2014) of 14 CMIP6 models and the ERA5 reanalysis. CMIP6 mostly reasonably reflect characteristics such as the amplitude of the oscillations, the return periods, as well as the spatial footprints of those atmospheric patterns in the SST and SLP fields. The ACCESS-CM2 and CanESM5-CanOE models stand out as they managed to capture the signal of the patterns analyzed in the tests performed and their influence on WS100. Although CMIP6 models performance in capturing local and regional forcing remains poor, especially in regions with complex terrain, they do allow for a monthly and seasonal analysis of their influence on the behavior of WS100, which has a great impact on the exploitation of the wind resource in South America.

We applied an EOF analysis on the WS100 field to detect the influence of the selected atmospheric patterns on three subregions of interest: REG1) northeast Brazil, REG2) northern Chile and Argentina and REG3) Patagonia. The SAA was found to be the main modulator of WS100 over northeast Brazil, given by a direct relationship, with correlation coefficients up to 0.55 in the monthly series (0.54 in winter and 0.46 in summer), between the SAA intensity and PC1 for REG1, which explains 59.1% of the total variance.

Over Patagonia we found that the behavior of WS100 is dominated in first place by a pattern of SLP anomalies, which we named PAT (Patagonia - Antarctic Pattern), centered around the Drake Passage and affecting the flow of the westerlies in the region. Significant negative correlations, up to -0.83 in summer and -0.75 in winter (-0.81 in the monthly series), were found between PAT and PC1 for REG3 that explains 52.2% of the total variance in the region. This means that the positive phase of the PAT index causes a decrease in WS100 over Patagonia, and vice versa. In second place, the AAO is responsible for the variability of WS100 over Patagonia mainly in summer, which is determined by positive correlation coefficients, up to 0.52 (0.42 in winter and 0.46 in the monthly series), between the AAO index and the PC2 for REG3 that explains 22.8% of the total variance. The positive phase of AAO causes an increase of WS100 over the southern tip of Patagonia, and a decrease north of 45° S.

In the case of northern Chile and Argentina, only a weak correlation coefficient of 0.3 (ERA5) between the SPA intensity and WS100 was found for the extreme cases of WS100, mainly during spring. An analysis with finer resolution of that region would allow for a greater insight on the behavior of the wind resource and its climate modulators. While for the Chilean side of Patagonia some influence of SPA was found, which appears more clearly particularly in winter with correlation coefficients up to 0.49 (0.4 in summer). The SPA plays a role in the mechanisms that cause variations in the pressure gradient and the intensity of the westerlies over the Patagonia region, and it is also negative correlated with ENSO, a relationship that should be explored in greater detail in the future.

This study is the first part of a more extensive project, with the main objective to estimate the long-term effects of the analyzed large-scale drivers on wind power generation in the future (until 2100). In forthcoming work, we would like to explore the persistence over time of the relationships found between those atmospheric patterns and 100 m wind speed over South América; using CMIP6 future scenarios (i.e., SSP2-4.5 and SSP5-8.5) for the models that we have found with better performance. We also keep in mind that it is important to focus separately on smaller regions of interest, given the diverse orography of South America and work with higher temporal resolution data to get more accurate results. That will allow us to evaluate the influence of climate variability and global warming on the future changes of wind resource and its impacts on wind power generation in the long term.

Declaration of interests

The authors declare that they have no known competing financial interests or personal relationships that could have appeared to influence the work reported in this paper.

Funding

This work was supported by the Agencia Nacional de Investigación y Desarrollo (ANID) de Chile [grant number 21210309] to OL. MJC acknowledges the support of the Center for Climate and Resilience Research (CR)2, ANID/FONDAP/1523A0002, and Center for Oceanographic Research COPAS Coastal, ANID/FB210021.

Author contributions

Ovidio Llompart: Conceptualization, Methodology, Investigation, Formal Analysis, Visualization, Writing – original draft, Writing – review & editing. **Héctor H. A. Sepúlveda:** Conceptualization, Methodology, Investigation, Supervision, Writing – review & editing. **Martín Jacques-Coper:** Conceptualization, Methodology, Investigation, Writing – review & editing. **Marieta Hernández:** Conceptualization, Writing – review & editing. All of the authors discussed the results and reviewed the manuscript.

Data availability statement

All datasets used in this study are freely accessible. The ERA5 reanalysis products are available at website https://cds.climate.copernicus.eu/cdsapp#!/dataset/reanalysis-era5-single-levels-monthly-means (last access on 1 February 2024). The CMIP6 simulations can be downloaded from https://cds.climate.copernicus.eu/cdsapp#!/dataset/projections-cmip6 (last access on 1 February 2024).

Supporting information

Figure S1: Superior limit of the red noise spectrum for each index time series simulated from CMIP6 models.

Figure S2: Spatial footprints of SPA index over the SST and SLP fields.

Figure S3: Spatial footprints of SAA index over the SST and SLP fields.

Figure S4: Spatial footprints of ONI index over the SST and SLP fields.

Figure S5: Spatial footprints of ONI index over the SST and SLP fields.

Figure S6: SST anomalies associated with extreme El Niño events.

Figure S7: SST anomalies associated with extreme La Niña events.

Figure S8: CMIP6 models validation based on available observational datasets.

Table S1: Magnitude of monthly and seasonal correlations between PCs and each subregion analyzed.

Table S2: Correlations between climate indices and PCs for the new regions considering Chilean and Argentinean sides separately.

References

Akinsanola, A. A., Ogunjobi, K. O., Abolude, A. T., & Salack, S. (2021). Projected changes in wind speed and wind energy potential over West Africa in CMIP6 models. *Environmental Research Letters*, *16*(4). https://doi.org/10.1088/1748-9326/abed7a

Alonzo, B., Ringkjob, H. K., Jourdier, B., Drobinski, P., Plougonven, R., & Tankov, P. (2017). Modelling the variability of the wind energy Equidistant Cylindrical

resource on monthly and seasonal timescales. In *Renewable Energy* (Vol. 113, pp. 1434–1446). Elsevier Ltd. https://doi.org/10.1016/j.renene.2017.07.019

An, S. I., & Jin, F. F. (2004). Nonlinearity and Asymmetry of ENSO. Journal of Climate, 17 (12), 2399–2412. https://doi.org/10.1175/1520-0442(2004)017<2399:NAAOE>2.0.CO;2

Ancapichún, S., & Garcés-Vargas, J. (2015). Variabilidad del anticiclón subtropical del pacífico sudeste y su impacto sobre la temperatura superficial del mar frente a la costa Centro-Norte de Chile. *Ciencias Marinas*, *41*(1), 1–20. https://doi.org/10.7773/cm.v41i1.2338

Aramburo, D., Montoya, R. D., & Osorio, A. F. (2022). Impact of the ENSO phenomenon on wave variability in the Pacific Ocean for wind sea and swell waves. *Dynamics of Atmospheres and Oceans*, *100*. https://doi.org/10.1016/j.dynatmoce.2022.101328

Bjerknes, J. (1969). Atmospheric teleconnections from the equatorial pacific. *Monthly Weather Review*, *97* (3), 163–172. https://doi.org/10.1175/1520-0493(1969)097<0163:ATFTEP>2.3.CO;2

Bianchi, E., Guozden, T., & Kozulj, R. (2022). Assessing low frequency variations in solar and wind power and their climatic teleconnections. *Renewable Energy*, *190*, 560–571. https://doi.org/10.1016/j.renene.2022.03.080

Bianchi, E., Solarte, A., & Guozden, T. M. (2017). Large scale climate drivers for wind resource in Southern South America. *Renewable Energy*, *114*, 708–715. https://doi.org/10.1016/j.renene.2017.07.075

Brayshaw, D. J., Troccoli, A., Fordham, R., & Methven, J. (2011). The impact of large scale atmospheric circulation patterns on wind power generation and its potential predictability: A case study over the UK. *Renewable Energy*, *36*(8), 2087–2096. https://doi.org/10.1016/j.renene.2011.01.025

Cabos, W., Sein, D. V., Pinto, J. G., Fink, A. H., Koldunov, N. V., Alvarez, F., Izquierdo, A., Keenlyside, N., & Jacob, D. (2017). The South Atlantic Anticyclone as a key player for the representation of the tropical Atlantic climate in coupled climate models. *Climate Dynamics*, *48*(11–12), 4051–4069. https://doi.org/10.1007/s00382-016-3319-9

Carvalho, D., Rocha, A., Costoya, X., deCastro, M., & Gómez-Gesteira, M. (2021). Wind energy resource over Europe under CMIP6 future climate projections: What changes from CMIP5 to CMIP6. *Renewable and Sustainable Energy Reviews*, *151*. https://doi.org/10.1016/j.rser.2021.111594

Codron, F. (2005). Relation between annular modes and the mean state: southern hemisphere summer. *Journal of Climate*, *18* (2), 320–330. https://doi.org/10.1175/JCLI-3255.1

Colberg, F., Reason, C. J. C., & Rodgers, K. (2004). South Atlantic response to El Niño-Southern Oscillation induced climate variability in an ocean general circulation model. *Journal of Geophysical Research: Oceans*, *109*(12), 1–14. https://doi.org/10.1029/2004JC002301

Correia, J. M., Bastos, A., Brito, M. C., & Trigo, R. M. (2017). The influence of the main large-scale circulation patterns on wind power production in Portugal. *Renewable Energy*, *102*, 214–223. https://doi.org/10.1016/j.renene.2016.10.002

Cradden, L. C., McDermott, F., Zubiate, L., Sweeney, C., & O'Malley, M. (2017). A 34-year simulation of wind generation potential for Ireland and the impact of large-scale atmospheric pressure patterns. *Renewable Energy*, *106*, 165–176. https://doi.org/10.1016/j.renene.2016.12.079

Dalton, A., Bekker, B., & Koivisto, M. J. (2021). Simulation and detection of wind power ramps and identification of their causative atmospheric circulation patterns. *Electric Power Systems Research*, *192*. https://doi.org/10.1016/j.epsr.2020.106936

de Souza Ferreira, G. W., Reboita, M. S., Ribeiro, J. G. M., Carvalho, V. S. B., Santiago, M. E. V., Silva, P. L. L. S., Baldoni, T. C., & de Souza, C. A. (2024). Assessment of the wind power density over South America simulated by CMIP6 models in the present and future climate. Climate Dynamics, 62(3), 1729–1763. https://doi.org/10.1007/s00382-023-06993-3

Deng, K., Azorin-Molina, C., Yang, S., Hu, C., Zhang, G., Minola, L., & Chen, D. (2022). Changes of Southern Hemisphere westerlies in the future warming climate. *Atmospheric Research*, *270*. https://doi.org/10.1016/j.atmosres.2022.106040

Farjami, H., & Hesari, A. R. E. (2020). Assessment of sea surface wind field pattern over the Caspian Sea using EOF analysis. *Regional Studies in Marine Science*, *35*. https://doi.org/10.1016/j.rsma.2020.101254

Fredriksen, H. B., Berner, J., Subramanian, A. C., & Capotondi, A. (2020). How Does El Niño–Southern Oscillation Change Under Global Warming—A First Look at CMIP6. *Geophysical Research Letters*, *47*(22). https://doi.org/10.1029/2020GL090640

Garreaud, R. D., Vuille, M., Compagnucci, R., & Marengo, J. (2009). Present-day South American climate. *Palaeogeography, Palaeoclimatology, Palaeoecology*, *281*(3–4), 180–195. https://doi.org/10.1016/j.palaeo.2007.10.032

Garrido-Perez, J. M., Ordóñez, C., Barriopedro, D., García-Herrera, R., & Paredes, D. (2020). Impact of weather regimes on wind power variability in western Europe. *Applied Energy*, *264*. https://doi.org/10.1016/j.apenergy.2020.114731

Gómez-Fontealba, C., Flores-Aqueveque, V., & Alfaro, S. C. (2022). Variability of the Southwestern Patagonia (51°S) Winds in the Recent (1980–2020) Period: Implications for Past Wind Reconstructions. *Atmosphere*, *13*(2). https://doi.org/10.3390/atmos13020206

Greene, C. A., Thirumalai, K., Kearney, K. A., Delgado, J. M., Schwanghart, W., Wolfenbarger, N. S., Thyng, K. M., Gwyther, D. E., Gardner, A. S., & Blankenship, D. D. (2019). The Climate Data Toolbox for MATLAB. *Geochemistry, Geophysics, Geosystems*, *20*(7), 3774–3781. https://doi.org/10.1029/2019GC008392

Gugliani, G., Sarkar, A., Ley, C., & Matsagar, V. (2021). Identification of optimum wind turbine parameters for varying wind climates using a novel month-based turbine performance index. Renewable Energy, 171, 902-914. https://doi.org/10.1016/j.renene.2021.02.141

Hayes, L., Stocks, M., & Blakers, A. (2021). Accurate long-term power generation model for offshore wind farms in Europe using ERA5 reanalysis. *Energy*, *229*. https://doi.org/10.1016/j.energy.2021.120603

Hou, M. & Tang, Y. (2022). Recent progress in simulating two types of ENSO – from CMIP5 to CMIP6. Frontiers in Marine Science, 9:986780. https://doi.org/10.3389/fmars.2022.986780

IRENA (2023), *Renewable capacity statistics 2023*, International Renewable Energy Agency, Abu Dhabi. ISBN: 978-92-9260-525-4

Jung, C., & Schindler, D. (2020). Introducing a new approach for wind energy potential assessment under climate change at the wind turbine scale. *Energy Conversion and Management*, *225*. https://doi.org/10.1016/j.enconman.2020.113425

Khasanzoda, N., Zicmane, I., Beryozkina, S., Safaraliev, M., Sultonov, S., & Kirgizov, A. (2022). Regression model for predicting the speed of wind flows for energy needs based on fuzzy logic. Renewable Energy, 191, 723-731. https://doi.org/10.1016/j.renene.2022.04.017

Kim, D.Y., Kim, Y. H., & Kim, B. S. (2021). Changes in wind turbine power characteristics and annual energy production due to atmospheric stability, turbulence intensity, and wind shear. Energy, 214, 119051. https://doi.org/10.1016/j.energy.2020.119051

Koletsis, I., Kotroni, V., Lagouvardos, K., & Soukissian, T. (2016). Assessment of offshore wind speed and power potential over the Mediterranean and the Black Seas under future climate changes. In *Renewable and Sustainable Energy Reviews* (Vol. 60, pp. 234–245). Elsevier Ltd. https://doi.org/10.1016/j.rser.2016.01.080

Li, X., Li, Q. P., Ding, Y. H., & Wang, M. (2022). Near-surface wind speed changes in eastern China during 1970–2019 winter and its possible causes. *Advances in Climate Change Research*, *13*(2), 228–239. https://doi.org/10.1016/j.accre.2022.01.003

Liao, H., Wang, C., & Song, Z. (2021). ENSO phase-locking biases from the CMIP5 to CMIP6 models and a possible explanation. *Deep-Sea Research Part II: Topical Studies in Oceanography*, *189–190*. https://doi.org/10.1016/j.dsr2.2021.104943

Lübbecke, J. F., Burls, N. J., Reason, C. J. C., & Mcphaden, M. J. (2014). Variability in the South Atlantic anticyclone and the Atlantic Niño mode. *Journal of Climate*, *27*(21), 8135–8150. https://doi.org/10.1175/JCLI-D-14-00202.1

Manwell, J. F., McGowan, J. G., & Rogers, A. L. (2010). *Wind Energy Explained: Theory, Design and Application*. John Wiley & Sons Ltd, The Atrium, Southern Gate, Chichester, West Sussex, PO19 8SQ, United Kingdom, 2010. ISBN 978-0-470-01500-1 (Hbk)

Marshall, G. J. (2003). Trends in the Southern Annular Mode from observations and reanalyses. *Journal of Climate*, *16*(24), 4134–4143. https://doi.org/10.1175/1520-0442(2003)016<4134:TITSAM>2.0.CO;2

Mendoza, V. M., Oda, B., Garduño, R., Villanueva, E. E., & Adem, J. (2014). Simulation of the PDO effect on the North America summer climate with emphasis on Mexico. *Atmospheric Research*, *137*, 228–244. https://doi.org/10.1016/j.atmosres.2013.10.010

Mitchell, T. P., & Wallace, J. M. (1996). ENSO Seasonality: 1950–78 versus 1979–92. Journal of Climate, 9 (12), 3149–3161. https://doi.org/10.1175/1520-0442(1996)009<3149:ESV>2.0.CO;2

Miyasaka, T., & Nakamura, H. (2010). Structure and mechanisms of the Southern Hemisphere summertime subtropical anticyclones. *Journal of Climate*, *23*(8), 2115–2130. https://doi.org/10.1175/2009JCLI3008.1

Mortensen, E., Wu, S., Notaro, M., Vavrus, S., Montgomery, R., De Piérola J., Sánchez, C. & Block, P. (2018). Regression-based season-ahead drought prediction for southern Peru conditioned on large-scale climate variables. Hydrology and Earth System Sciences, 22, 287–303. https://doi.org/10.5194/hess-22-287-2018

Neelin, J. D., Jin F. F., & Syu, H. H. (2000). Variations in ENSO Phase Locking. Journal of Climate, 13 (14), 2570–2590. https://doi.org/10.1175/1520-0442(2000)013<2570:VIEPL>2.0.CO;2

Ohba, M., Kadokura, S., & Nohara, D. (2016). Impacts of synoptic circulation patterns on wind power ramp events in East Japan. *Renewable Energy*, *96*, 591–602. https://doi.org/10.1016/j.renene.2016.05.032

Olauson, J. (2018). ERA5: The new champion of wind power modelling? *Renewable Energy*, *126*, 322–331. https://doi.org/10.1016/j.renene.2018.03.056

Patel, R. P., Nagababu, G., Kachhwaha, S. S., & Surisetty, V. V. A. K. (2022). A revised offshore wind resource assessment and site selection along the Indian coast using ERA5 near-hub-height wind products. *Ocean Engineering*, *254*. https://doi.org/10.1016/j.oceaneng.2022.111341

Qian, H., & Zhang, R. (2021). Future changes in wind energy resource over the Northwest Passage based on the CMIP6 climate projections. *International Journal of Energy Research*, *45*(1), 920–937. https://doi.org/10.1002/er.5997

Ravestein, P., van der Schrier, G., Haarsma, R., Scheele, R., & van den Broek, M. (2018). Vulnerability of European intermittent renewable energy supply to climate change and climate variability. *Renewable and Sustainable Energy Reviews*, *97*, 497–508. https://doi.org/10.1016/j.rser.2018.08.057

Rodwell, M. J., & Hoskins, B. J. (2001). Subtropical anticyclones and summer monsoons. *Journal of Climate*, *14*(15), 3192–3211. https://doi.org/10.1175/1520-0442(2001)014<3192:SAASM>2.0.CO;2

Sakuru, S. K. V. S., & Ramana, M. V. (2023). Wind power potential over India using the ERA5 reanalysis. *Sustainable Energy Technologies and Assessments*, *56*. https://doi.org/10.1016/j.seta.2023.103038

Serykh, I.V., & Sonechkin, D.M. (2024). Global El Niño–Southern Oscillation teleconnections in CMIP6 models. Atmosphere, 15, 500. https:// doi.org/10.3390/atmos15040500

Sinha, M., Jha, S., & Chakraborty, P. (2020). Indian Ocean wind speed variability and global teleconnection patterns. *Oceanologia*, *62*(2), 126–138. https://doi.org/10.1016/j.oceano.2019.10.002

Soukissian, T. H., Karathanasi, F. E., & Zaragkas, D. K. (2021). Exploiting offshore wind and solar resources in the Mediterranean using ERA5 reanalysis data. *Energy Conversion and Management*, *237*. https://doi.org/10.1016/j.enconman.2021.114092

Srinivas, G., Vialard, J., Liu, F., Voldoire, A., Izumo, T., Guilyardi, E., & Lengaigne, M. (2024). Dominant contribution of atmospheric nonlinearities to ENSO asymmetry and extreme El Niño events. Scientific Reports, 14, 8122. https://doi.org/10.1038/s41598-024-58803-3

Sterl, A., & Hazeleger, W. (2003). Coupled variability and air-sea interaction in the South Atlantic Ocean. *Climate Dynamics*, *21*(7–8), 559–571. https://doi.org/10.1007/s00382-003-0348-y

Sulca, J., Takahashi, K., Espinoza, J. C., Tacza, J., Zubieta, R., Mosquera, K., & Apaestegui, J. (2024). A multiple linear regression model for the prediction of summer rainfall in the northwestern Peruvian Amazon using large-scale índices. Climate Dynamics, 62, 4431–4451. https://doi.org/10.1007/s00382-023-07044-7

Thompson, D. W. J., & Wallace, J. M. (2000). Annular modes in the extratropical circulation. Part I: month-to-month variability. *Journal of Climate*, *13* (5), 1000–1016. https://doi.org/10.1175/1520-0442(2000)013<1000:AMITEC>2.0.CO;2

Tian, Q., Huang, G., Hu, K., & Niyogi, D. (2019). Observed and global climate model based changes in wind power potential over the Northern Hemisphere during 1979–2016. *Energy*, *167*, 1224–1235. https://doi.org/10.1016/j.energy.2018.11.027

Tobin, I., Jerez, S., Vautard, R., Thais, F., Van Meijgaard, E., Prein, A., Déqué, M., Kotlarski, S., Maule, C. F., Nikulin, G., Noël, T., & Teichmann, C. (2016). Climate change impacts on the power generation potential of a European mid-century wind farms scenario. In *Environmental Research Letters* (Vol. 11, Issue 3). Institute of Physics Publishing. https://doi.org/10.1088/1748-9326/11/3/034013

Tobin, I., Vautard, R., Balog, I., Bréon, F. M., Jerez, S., Ruti, P. M., Thais, F., Vrac, M., & Yiou, P. (2015). Assessing climate change impacts on European wind energy from ENSEMBLES high-resolution climate projections. *Climatic Change*, *128*(1–2), 99–112. https://doi.org/10.1007/s10584-014-1291-0

Vaittinada Ayar, P., Battisti, D. S., Li, C., King, M., Vrac, M., & Tjiputra, J. (2023). A regime view of ENSO flavors through clustering in CMIP6 models. Earth's Future, 11, e2022EF003460. https://doi.org/10.1029/2022EF003460

Wang, K., Wu, D., Zhang, T., Yin, L., Wu, K., & Zheng, C. (2024). Spatial distribution and long-term trend of wind energy in the Northwest Pacific Ocean. *Water-Energy Nexus*. https://doi.org/10.1016/j.wen.2023.11.005

Watts, D., Durán, P., & Flores, Y. (2017). How does El Niño Southern Oscillation impact the wind resource in Chile? A techno-economical assessment of the influence of El Niño and La Niña on the wind power. *Renewable Energy*, *103*, 128–142. https://doi.org/10.1016/j.renene.2016.10.031

Weber, J., Gotzens, F., & Witthaut, D. (2018). Impact of strong climate change on the statistics of wind power generation in Europe. *Energy Procedia*, *153*, 22–28. https://doi.org/10.1016/j.egypro.2018.10.004

Wilks, D. S. (2006). Statistical methods in the atmospheric sciences, Second Edition (pp. 394–397). Volume 91 in the International Geophysics Series. Elsevier Inc. 30 Corporate Drive, Suite 400, Burlington, MA 01803, USA. ISBN 13: 978-0-12-751966-1, ISBN 10: 0-12-751966-1

Wu, J., Shi, Y., & Xu, Y. (2020). Evaluation and Projection of Surface Wind Speed Over China Based on CMIP6 GCMs. *Journal of Geophysical Research: Atmospheres*, *125*(22). https://doi.org/10.1029/2020JD033611

Zhang, S., & Li, X. (2021). Future projections of offshore wind energy resources in China using CMIP6 simulations and a deep learning-based downscaling method. *Energy*, *217*. https://doi.org/10.1016/j.energy.2020.119321

Zhou, F., Zhao, Z., Azorin-Molina, C., Jia, X., Zhang, G., Chen, D., Liu, J., Guijarro, J. A., Zhang, F., & Fang, K. (2022). Teleconnections between large-scale oceanic-atmospheric patterns and interannual surface wind speed variability across China: Regional and seasonal patterns. *Science of the Total Environment*, *838*. https://doi.org/10.1016/j.scitotenv.2022.156023

Supplementary Material

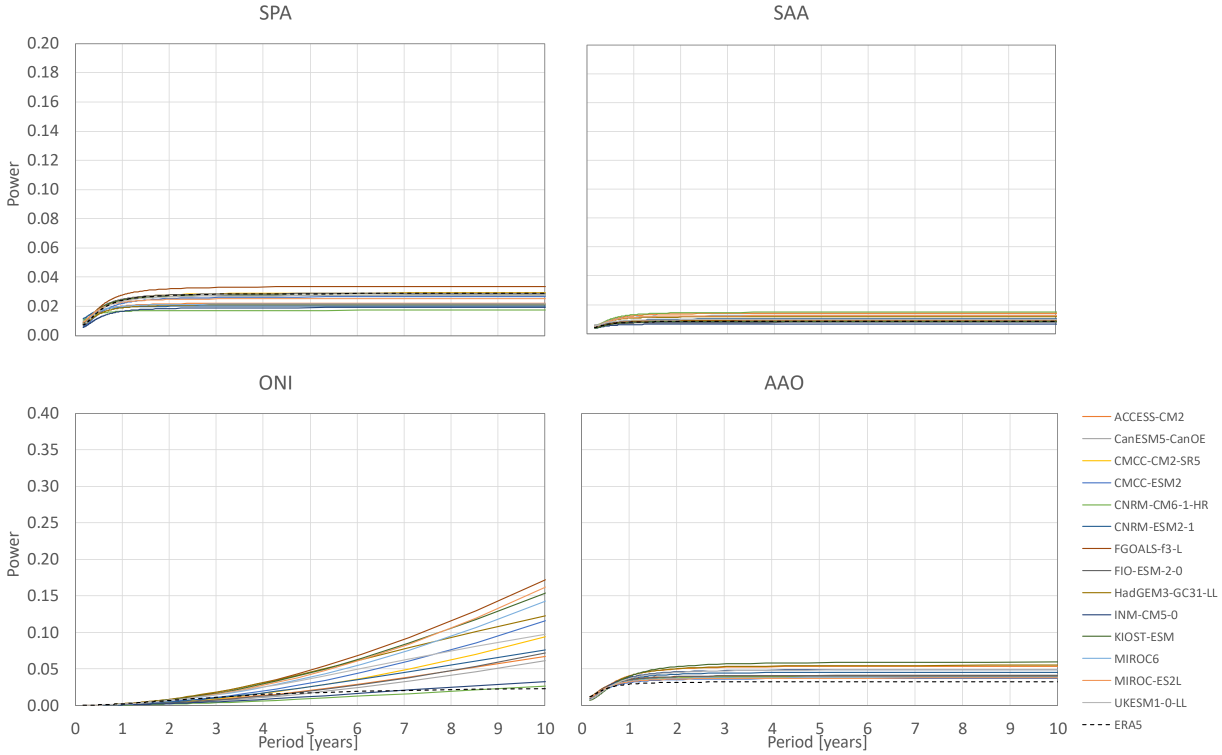

Figure S1. Superior limit of the red noise spectrum at a 95% confidence interval for each index time series simulated from CMIP6 models.

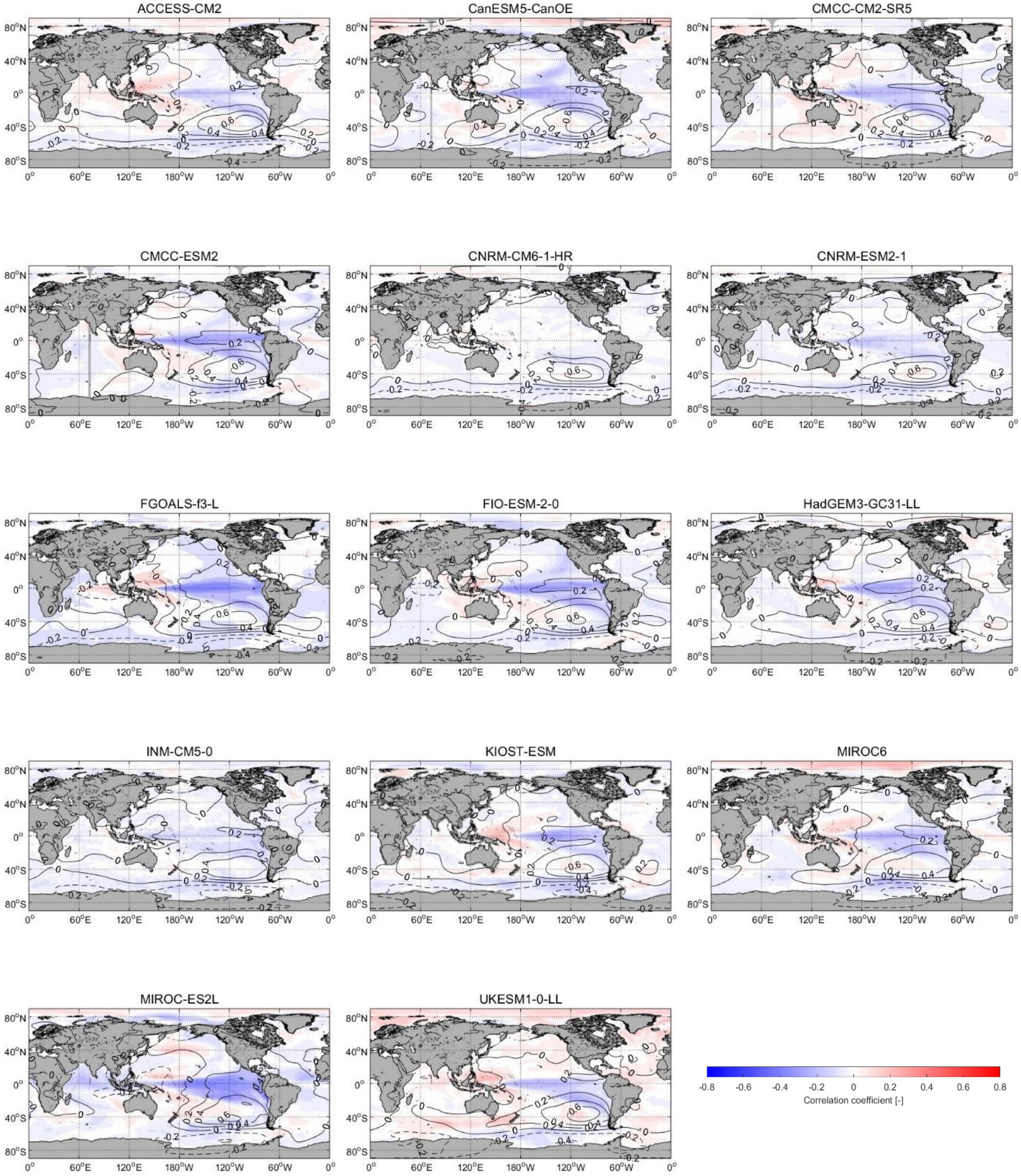

Figure S2. Spatial footprints of SPA index over the SST and SLP fields, calculated using monthly values of SST and SLP during 1980-2014 from each CMIP6 model. The values correspond to the Pearson correlation coefficients at a 95% confidence interval.

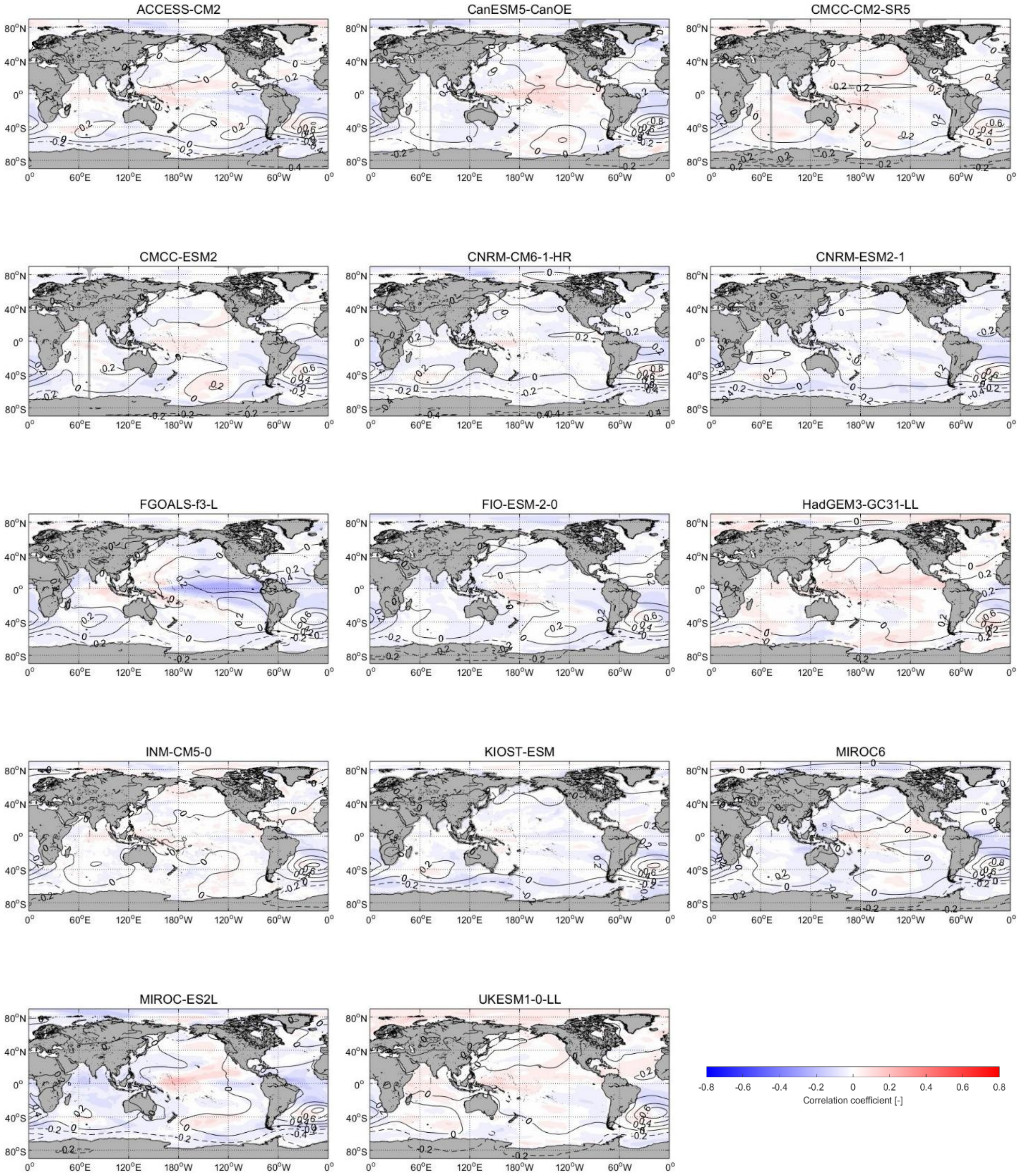

Figure S3. Spatial footprints of SAA index over the SST and SLP fields, calculated using annual mean values of SST and SLP during 1980-2014 from each CMIP6 model. The values correspond to the Pearson correlation coefficients at a 95% confidence interval.

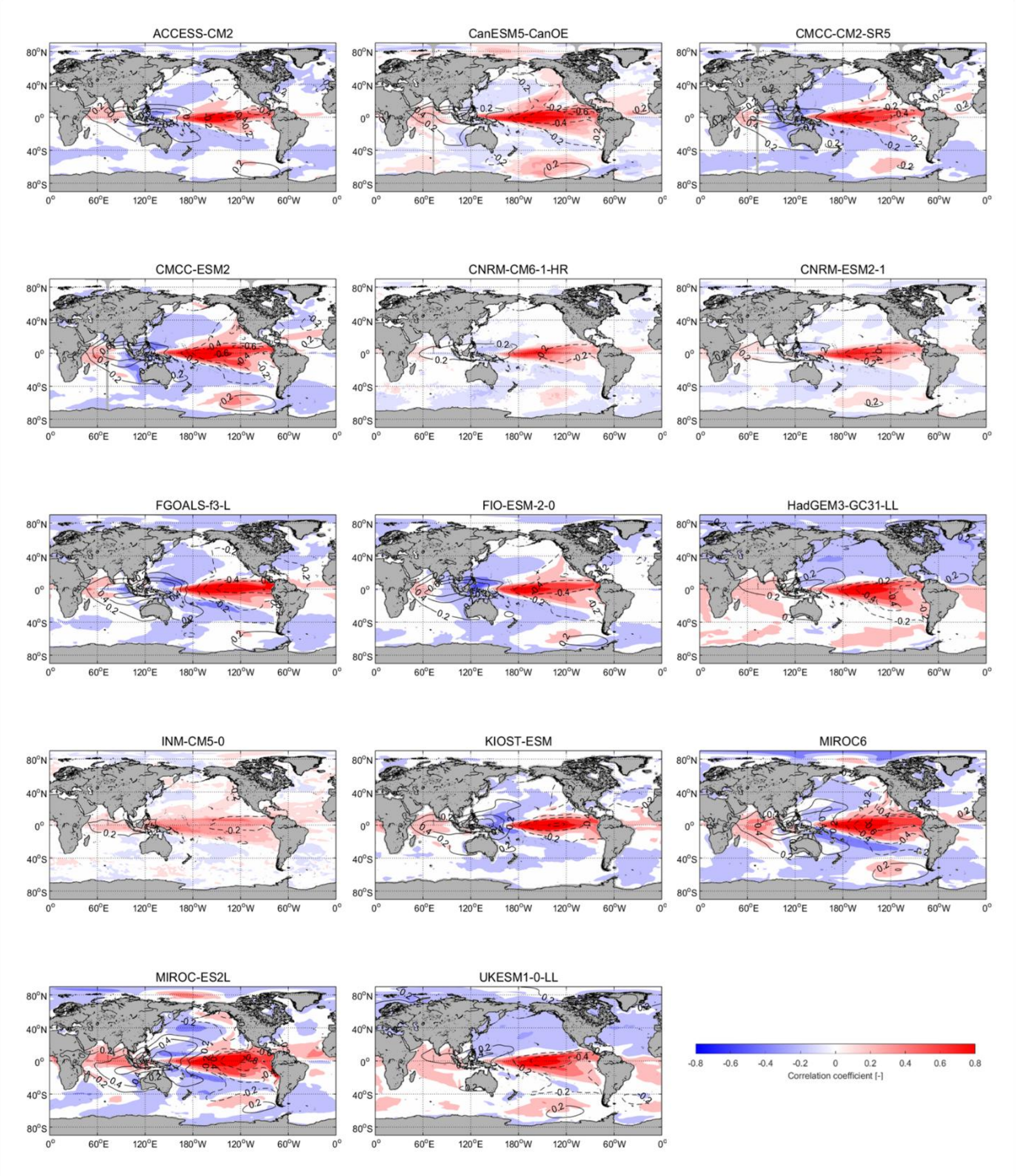

Figure S4. Spatial footprints of ONI index over the SST and SLP fields, calculated using monthly values of SST and SLP during 1980-2014 from each CMIP6 model. The values correspond to the Pearson correlation coefficients at a 95% confidence interval.

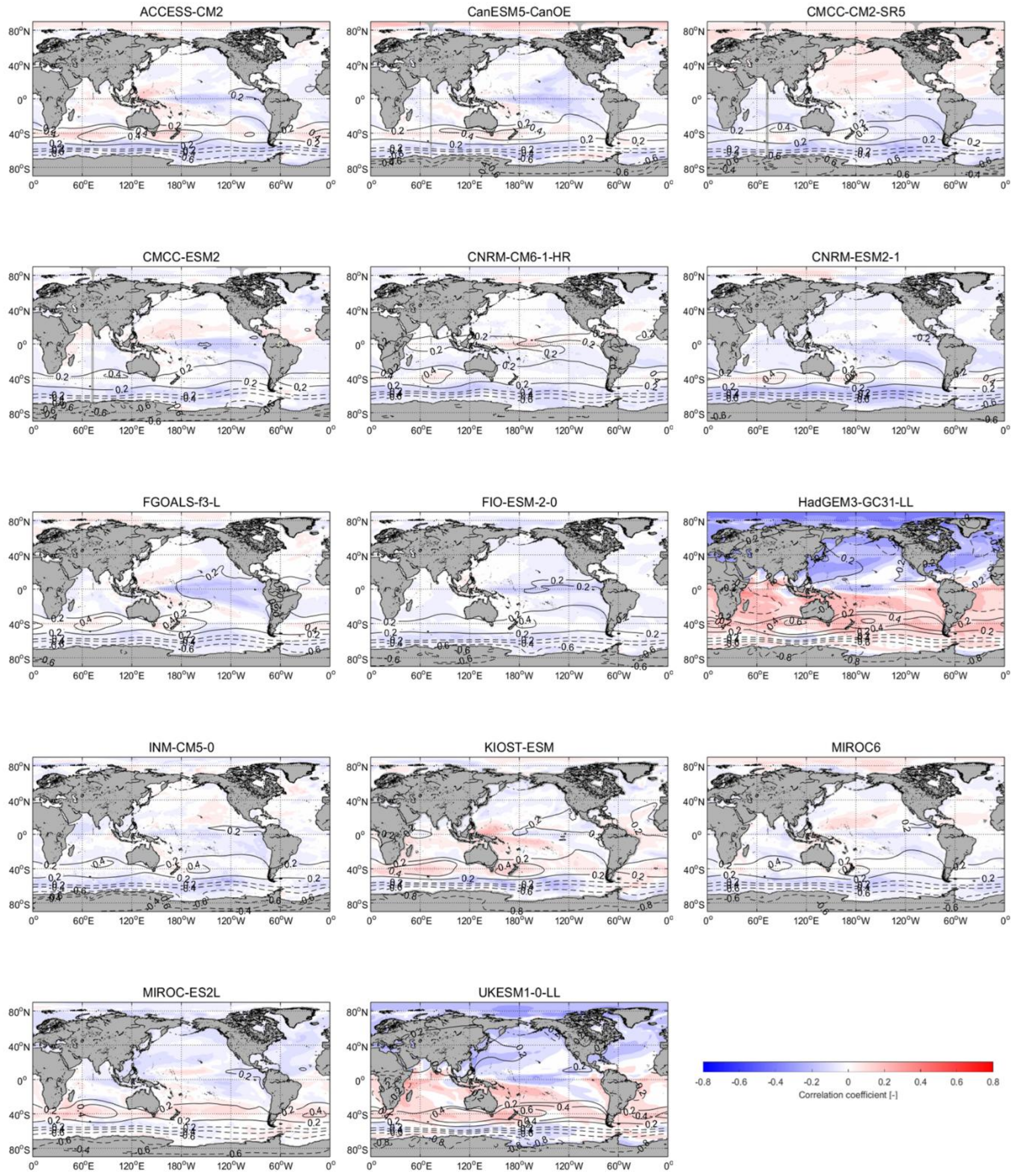

Figure S5. Spatial footprints of AAO index over the SST and SLP fields, calculated using monthly values of SST and SLP during 1980-2014 from each CMIP6 model. The values correspond to the Pearson correlation coefficients at a 95% confidence interval.

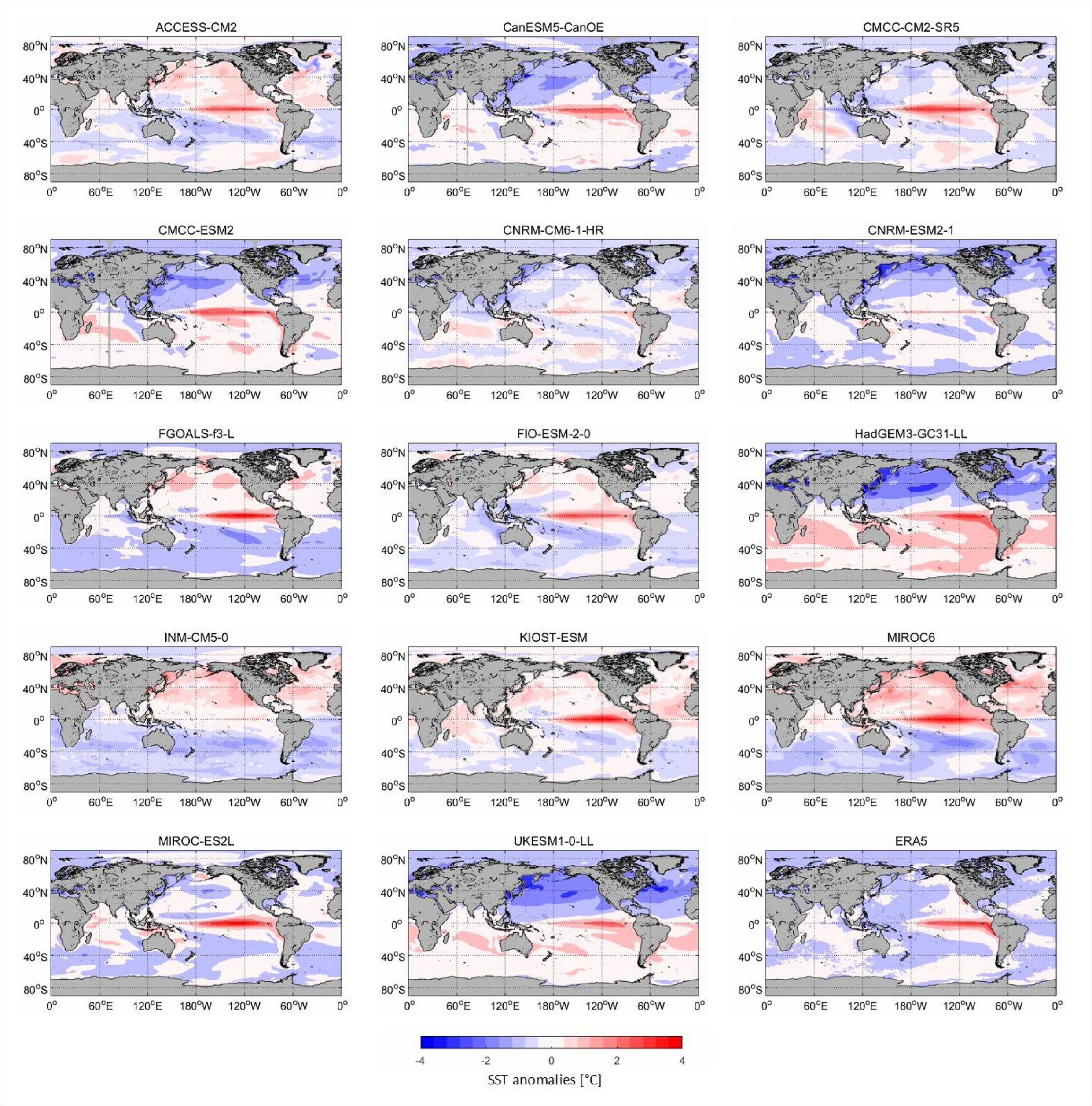

Figure S6. SST anomalies associated with extreme El Niño events, based on the higher 5% of the total cases of ONI positive anomalies (≥ 0.5°C).

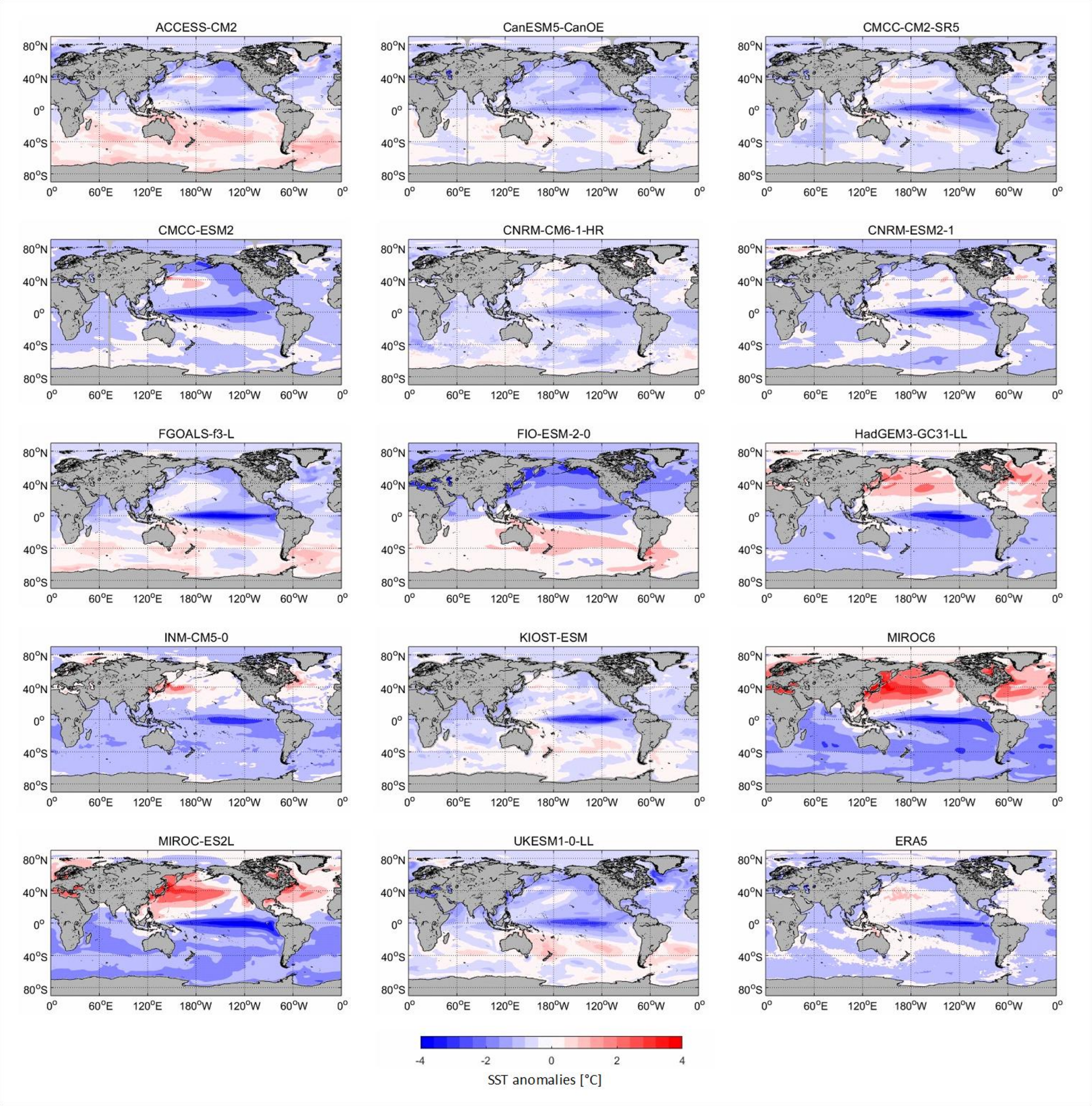

Figure S7. SST anomalies associated with extreme La Niña events, based on the lower 5% of the total cases of ONI negative anomalies (≤ -0.5°C).

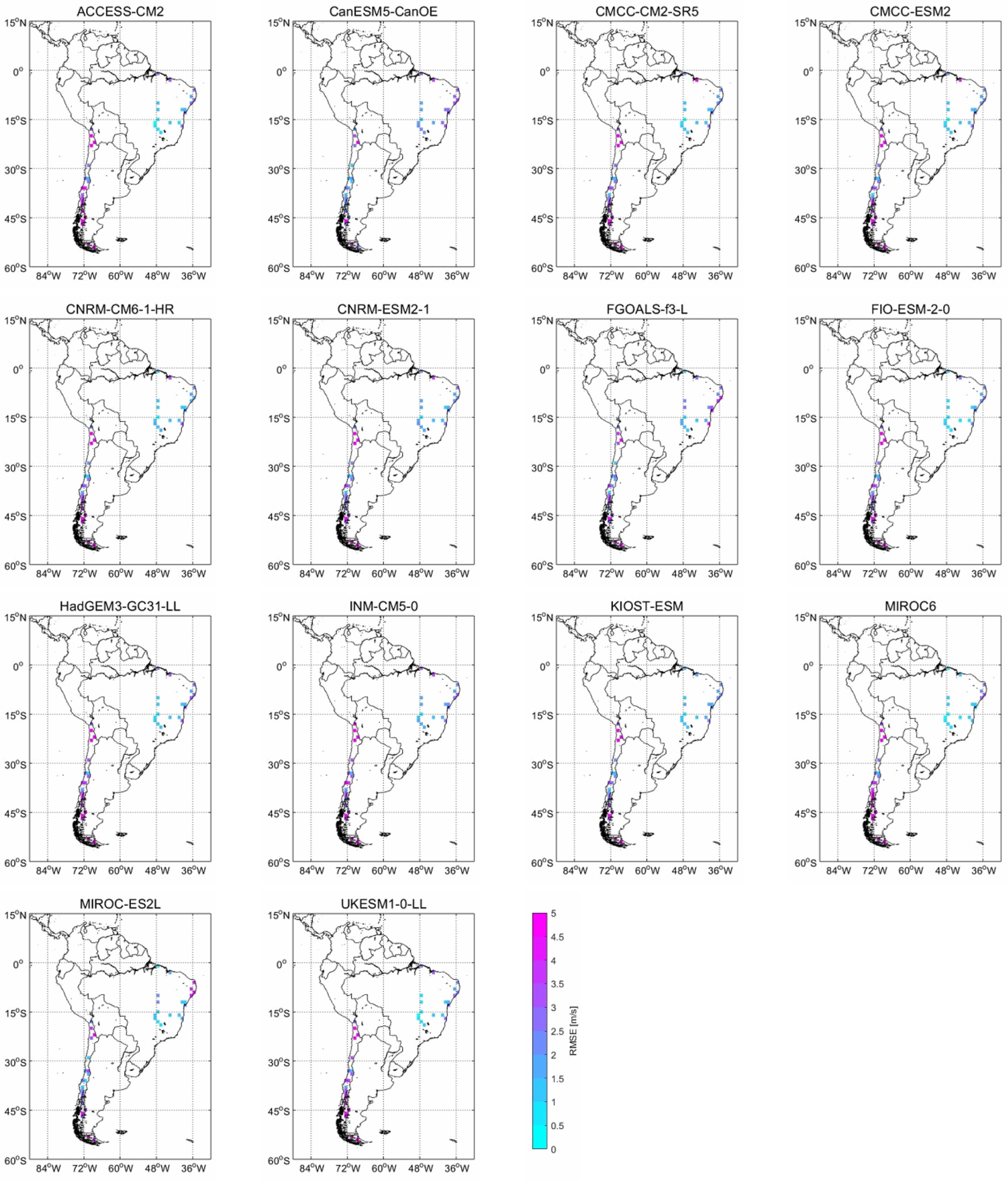

Figure S8. CMIP6 models validation based on available observational datasets from meteorological stations located in Northeast Brazil and Chile. Surface wind datasets obtained from Brazilian National Meteorological Institute (https://portal.inmet.gov.br) and Chilean Meteorological Department (https://climatologia.meteochile.gob.cl).

Table S1. Magnitude of monthly and seasonal correlation between PCs and WS100 (significant values in bold).

		REG1				REG2				REG3				REG1				REG2				REG3			
	MODEL	PC1				PC1				PC1				PC2				PC2				PC2			
		ONI	AAO	SPA	SAA	ONI	AAO	SPA	SAA	ONI	AAO	SPA	SAA	ONI	AAO	SPA	SAA	ONI	AAO	SPA	SAA	ONI	AAO	SPA	SAA
MON	ERA5	0.06	0.06	0.00	**0.45**	**0.30**	**0.27**	**0.15**	0.02	**0.10**	0.02	**0.19**	**0.11**	**0.28**	0.05	**0.12**	0.09	0.02	0.02	**0.30**	**0.13**	**0.18**	**0.44**	**0.35**	**0.14**
	ACCESS-CM2	**0.14**	0.07	**0.14**	**0.41**	**0.10**	0.02	0.10	**0.10**	0.08	**0.10**	**0.20**	**0.20**	**0.17**	**0.11**	**0.12**	**0.24**	**0.33**	0.04	0.03	**0.18**	**0.15**	**0.46**	**0.34**	**0.30**
	CanESM5-CanOE	**0.11**	**0.13**	0.04	**0.55**	**0.30**	**0.11**	**0.11**	**0.14**	**0.11**	0.06	**0.26**	**0.18**	**0.49**	**0.27**	**0.19**	0.04	**0.10**	0.06	**0.10**	**0.17**	0.05	**0.39**	**0.20**	**0.19**
	CMCC-CM2-SR5	0.06	**0.17**	**0.23**	**0.49**	**0.20**	0.06	**0.10**	0.00	**0.11**	**0.12**	**0.25**	**0.19**	**0.32**	**0.10**	0.04	0.03	**0.12**	**0.12**	0.06	**0.15**	0.10	**0.23**	**0.19**	0.06
	CMCC-ESM2	0.03	**0.13**	**0.25**	**0.53**	**0.36**	**0.11**	0.04	0.01	**0.15**	**0.14**	**0.31**	**0.29**	**0.40**	**0.11**	**0.21**	0.09	**0.12**	**0.10**	0.08	**0.10**	0.07	**0.25**	0.02	0.07
	CNRM-CM6-1-HR	0.01	**0.11**	0.03	**0.42**	0.06	0.08	0.09	0.03	0.02	0.07	0.06	0.03	0.09	0.04	0.07	**0.15**	0.09	0.05	**0.17**	**0.16**	0.02	**0.31**	**0.25**	**0.15**
	CNRM-ESM2-1	0.07	**0.10**	0.02	**0.40**	**0.25**	0.07	0.02	0.01	0.05	0.05	**0.14**	**0.16**	0.02	0.02	0.09	0.08	0.00	0.01	**0.19**	**0.20**	**0.12**	**0.31**	**0.15**	**0.21**
	FGOALS-f3-L	0.02	0.04	**0.19**	**0.44**	**0.45**	**0.12**	**0.11**	**0.23**	**0.28**	**0.11**	**0.14**	0.09	**0.11**	0.07	0.07	**0.12**	0.03	**0.22**	**0.25**	0.01	**0.22**	**0.34**	**0.29**	**0.21**
	FIO-ESM-2-0	0.01	**0.17**	**0.16**	**0.50**	**0.19**	0.02	**0.12**	0.04	**0.21**	0.03	**0.22**	**0.14**	0.01	0.09	**0.15**	**0.19**	0.02	**0.10**	0.02	**0.18**	0.07	**0.27**	**0.20**	0.06
	HadGEM3-GC31-LL	**0.14**	**0.15**	0.00	**0.18**	**0.18**	**0.21**	0.05	0.02	**0.20**	**0.19**	**0.18**	0.05	**0.11**	**0.31**	0.09	**0.12**	0.05	**0.14**	0.01	0.03	0.01	**0.33**	**0.24**	**0.15**
	INM-CM5-0	0.06	0.05	0.05	**0.39**	0.02	**0.20**	0.08	**0.11**	0.06	0.07	0.05	**0.12**	**0.12**	0.08	**0.16**	0.02	0.05	0.06	**0.29**	0.09	0.08	**0.36**	**0.28**	0.04
	KIOST-ESM	0.05	0.05	**0.17**	**0.39**	0.07	**0.11**	0.05	0.03	**0.21**	**0.14**	**0.23**	**0.28**	**0.21**	**0.14**	0.03	0.07	**0.28**	0.03	**0.11**	0.07	0.03	**0.26**	**0.25**	**0.16**
	MIROC6	**0.34**	0.03	0.06	**0.38**	**0.32**	0.02	0.01	0.08	**0.19**	**0.10**	0.09	**0.13**	0.07	**0.14**	0.07	**0.28**	**0.28**	0.07	0.07	**0.21**	**0.11**	**0.27**	**0.17**	0.07
	MIROC-ES2L	**0.38**	0.02	0.09	**0.31**	**0.24**	0.03	0.02	**0.15**	**0.26**	0.01	**0.14**	**0.11**	**0.48**	**0.12**	**0.15**	**0.23**	0.01	0.08	0.01	**0.21**	0.09	**0.30**	**0.12**	**0.22**
	UKESM1-0-LL	**0.10**	0.06	0.00	**0.14**	**0.12**	**0.12**	0.00	0.04	**0.10**	**0.16**	**0.11**	**0.15**	**0.14**	**0.35**	0.02	0.05	0.08	**0.11**	0.01	0.04	**0.10**	**0.33**	**0.25**	0.09
	MODEL	PC1				PC1				PC1				PC2				PC2				PC2			
		ONI	AAO	SPA	SAA	ONI	AAO	SPA	SAA	ONI	AAO	SPA	SAA	ONI	AAO	SPA	SAA	ONI	AAO	SPA	SAA	ONI	AAO	SPA	SAA
DJF	ERA5	0.17	0.07	0.08	**0.32**	**0.27**	**0.22**	0.09	0.16	0.09	0.08	0.14	0.02	0.08	0.06	**0.21**	0.08	0.05	0.05	0.06	0.11	0.16	**0.40**	**0.23**	**0.20**
	ACCESS-CM2	**0.21**	0.06	0.12	0.06	**0.20**	0.08	0.02	0.02	0.09	0.11	0.03	0.17	0.10	**0.21**	**0.24**	0.16	**0.21**	0.02	0.00	0.04	0.11	**0.51**	**0.34**	**0.31**
	CanESM5-CanOE	**0.29**	0.18	**0.19**	0.09	**0.33**	0.03	0.06	0.16	**0.24**	**0.21**	0.04	0.07	0.12	**0.04**	0.05	0.01	0.15	0.03	0.12	**0.19**	0.16	**0.50**	**0.20**	0.14
	CMCC-CM2-SR5	0.05	0.03	0.07	0.12	0.07	0.01	**0.23**	0.08	0.07	0.14	0.06	0.14	**0.46**	0.01	0.00	0.00	0.06	**0.22**	0.05	0.02	0.06	0.05	0.08	0.10
	CMCC-ESM2	**0.32**	0.15	**0.19**	**0.40**	**0.41**	0.12	**0.21**	0.16	0.10	0.02	0.02	0.09	0.02	0.07	**0.28**	**0.25**	0.12	**0.08**	0.02	0.10	0.00	0.03	**0.25**	0.04
	CNRM-CM6-1-HR	0.12	0.03	0.04	0.13	0.13	0.01	0.04	0.06	0.10	0.03	0.09	0.01	0.01	0.09	**0.19**	0.13	0.18	0.12	0.04	**0.29**	0.05	**0.47**	**0.38**	0.13
	CNRM-ESM2-1	0.08	0.14	0.01	**0.21**	**0.25**	0.02	0.02	0.12	**0.21**	0.00	0.07	**0.24**	**0.25**	0.09	**0.25**	0.16	0.01	0.12	0.08	0.13	**0.30**	**0.49**	**0.28**	0.14
	FGOALS-f3-L	0.16	0.04	0.00	0.12	**0.44**	0.12	0.01	0.04	**0.38**	0.02	0.04	0.08	0.14	0.08	0.10	0.08	0.10	0.00	0.09	0.04	**0.23**	**0.41**	**0.36**	**0.23**
	FIO-ESM-2-0	0.01	0.01	0.02	**0.22**	0.18	0.02	0.13	0.09	0.18	**0.23**	0.05	0.07	**0.26**	**0.10**	0.14	0.04	0.05	**0.29**	0.08	**0.22**	0.09	0.10	0.13	0.10
	HadGEM3-GC31-LL	0.14	0.03	0.04	**0.20**	**0.25**	0.09	0.00	0.16	**0.26**	0.08	0.14	0.06	**0.20**	0.13	**0.27**	0.09	0.09	0.01	0.03	0.04	0.11	**0.52**	**0.30**	0.12
	INM-CM5-0	**0.20**	**0.20**	**0.30**	**0.46**	0.02	**0.33**	0.08	**0.22**	0.02	**0.48**	**0.38**	0.08	0.00	**0.19**	**0.26**	0.08	0.14	0.15	0.04	0.08	0.03	**0.28**	**0.20**	0.05
	KIOST-ESM	0.18	0.18	0.13	**0.25**	0.14	0.04	0.17	0.14	0.19	0.12	**0.23**	0.01	**0.31**	**0.15**	**0.23**	0.07	**0.29**	**0.13**	0.05	0.06	0.18	**0.34**	**0.26**	0.18
	MIROC6	**0.41**	0.05	0.10	0.15	**0.39**	0.17	0.12	**0.28**	0.11	0.14	0.12	0.01	**0.37**	**0.10**	0.01	**0.23**	**0.21**	**0.21**	0.17	0.09	0.15	**0.37**	0.18	0.06
	MIROC-ES2L	**0.70**	0.18	0.15	0.13	**0.35**	0.17	0.13	0.02	**0.39**	0.18	0.16	0.01	**0.24**	**0.18**	0.14	0.08	**0.37**	**0.03**	0.08	**0.31**	0.04	**0.48**	0.18	**0.22**
	UKESM1-0-LL	**0.22**	0.02	0.06	0.12	0.14	0.14	0.01	0.06	0.05	**0.33**	**0.30**	0.19	0.04	0.01	0.15	**0.20**	0.06	0.01	0.15	0.14	**0.22**	**0.50**	**0.26**	0.04
	MODEL	PC1				PC1				PC1				PC2				PC2				PC2			
		ONI	AAO	SPA	SAA	ONI	AAO	SPA	SAA	ONI	AAO	SPA	SAA	ONI	AAO	SPA	SAA	ONI	AAO	SPA	SAA	ONI	AAO	SPA	SAA
JJA	ERA5	**0.30**	0.13	**0.24**	**0.44**	**0.19**	0.18	**0.37**	0.13	0.17	**0.20**	**0.39**	**0.21**	0.06	0.00	0.09	0.04	**0.25**	0.15	0.04	0.00	**0.21**	**0.26**	**0.23**	0.13
	ACCESS-CM2	0.11	0.14	0.17	**0.42**	0.16	0.19	0.18	0.14	0.10	0.09	**0.29**	**0.21**	**0.25**	0.09	**0.22**	**0.51**	0.07	0.05	0.13	**0.21**	0.10	**0.42**	**0.36**	**0.31**
	CanESM5-CanOE	0.15	0.15	0.03	**0.49**	**0.27**	0.09	0.12	**0.24**	0.07	**0.21**	**0.44**	**0.29**	**0.21**	**0.22**	0.14	**0.48**	0.06	0.16	0.14	0.08	0.02	**0.22**	0.04	0.19
	CMCC-CM2-SR5	0.04	**0.19**	0.12	**0.23**	0.10	0.10	0.04	0.03	0.02	**0.29**	**0.29**	0.17	**0.30**	**0.27**	**0.39**	**0.52**	0.09	0.13	0.04	0.14	**0.23**	**0.22**	**0.20**	0.00
	CMCC-ESM2	0.03	0.01	0.10	0.19	0.10	0.08	0.03	0.08	**0.27**	**0.33**	**0.39**	**0.34**	**0.39**	**0.20**	**0.42**	**0.34**	**0.28**	**0.22**	**0.22**	**0.20**	0.17	**0.25**	0.10	0.19
	CNRM-CM6-1-HR	0.04	0.07	0.03	**0.26**	0.02	**0.23**	0.01	0.05	0.02	**0.27**	0.02	0.13	0.11	0.18	0.03	**0.55**	0.08	**0.29**	**0.23**	0.19	0.04	**0.39**	**0.32**	**0.20**
	CNRM-ESM2-1	0.05	0.01	0.07	**0.22**	0.11	0.03	0.01	0.12	0.13	0.13	0.15	0.05	0.08	0.05	0.05	**0.37**	0.17	0.06	**0.22**	**0.34**	0.04	**0.23**	0.11	**0.35**
	FGOALS-f3-L	**0.25**	0.03	**0.21**	**0.33**	**0.39**	**0.19**	0.15	**0.24**	0.13	0.10	0.16	0.14	**0.44**	0.09	0.18	**0.50**	0.04	**0.28**	**0.33**	0.04	**0.27**	**0.35**	**0.30**	0.14
	FIO-ESM-2-0	0.10	0.18	0.18	**0.28**	0.14	0.07	0.14	0.10	**0.25**	**0.21**	**0.31**	**0.21**	**0.52**	**0.35**	**0.45**	**0.45**	**0.28**	**0.32**	**0.24**	0.11	**0.21**	**0.30**	**0.37**	0.09
	HadGEM3-GC31-LL	**0.25**	0.07	0.16	**0.50**	**0.20**	0.15	0.16	**0.27**	**0.23**	**0.23**	**0.50**	**0.21**	0.05	**0.34**	**0.21**	**0.46**	**0.33**	**0.20**	**0.31**	0.18	0.01	0.12	0.14	0.19
	INM-CM5-0	0.04	0.11	0.15	**0.31**	0.01	0.15	0.02	0.04	**0.23**	**0.21**	**0.29**	**0.22**	**0.24**	**0.21**	**0.26**	0.17	0.02	**0.25**	**0.39**	0.04	0.11	**0.35**	**0.31**	0.02
	KIOST-ESM	0.19	0.06	0.18	**0.24**	0.11	0.16	0.06	0.05	0.12	**0.33**	**0.30**	**0.49**	**0.27**	**0.24**	**0.34**	**0.30**	0.13	0.00	0.01	0.18	0.15	0.16	**0.26**	0.13
	MIROC6	0.07	0.14	0.01	**0.39**	**0.35**	0.02	0.00	0.01	**0.44**	0.09	**0.21**	0.07	**0.55**	0.02	0.14	**0.43**	**0.43**	**0.27**	**0.20**	0.18	**0.23**	**0.21**	**0.26**	0.04
	MIROC-ES2L	0.13	0.08	0.00	**0.54**	**0.23**	0.07	0.04	0.11	**0.21**	**0.21**	0.10	0.00	**0.35**	0.12	0.13	0.10	**0.32**	**0.31**	0.15	0.12	0.11	0.13	0.14	**0.31**
	UKESM1-0-LL	**0.23**	**0.21**	0.10	**0.44**	**0.19**	0.12	0.05	0.05	0.06	0.14	**0.21**	**0.20**	0.03	0.02	0.10	**0.25**	0.19	0.12	0.03	0.01	0.15	0.19	0.14	0.02

0 0.3 0.45 0.6 0.75 0.9

Correlation coefficient [-]

Table S2. Correlations between climate indices and PCs considering Chilean and Argentinean sides separately.

		REG 2 (Chilean side)				REG 2 (Argentinean side)				REG 3 (Chilean side)				REG 3 (Argentinean side)			
	MODEL	PC1		PC2		PC1		PC2		PC1		PC2		PC1		PC2	
		SPA	ONI	SPA	ONI	SAA	ONI	SAA	ONI	SPA	ONI	SPA	ONI	SAA	ONI	SAA	ONI
MON	ERA5	0.01	0.12	0.07	0.17	0.01	0.12	0.04	0.17	0.05	0.06	0.04	0.07	0.03	0.06	0.05	0.07
	ACCESS-CM2	0.12	0.13	0.05	0.08	0.08	0.00	0.00	0.01	0.05	0.07	0.02	0.06	0.02	0.00	0.00	0.06
	CanESM5-CanOE	0.03	0.05	0.03	0.03	0.00	0.08	0.06	0.00	0.04	0.13	0.01	0.00	0.01	0.13	0.01	0.01
	CMCC-CM2-SR5	0.09	0.09	0.09	0.19	0.04	0.11	0.14	0.08	0.01	0.08	0.01	0.14	0.00	0.01	0.07	0.10
	CMCC-ESM2	0.03	0.22	0.03	0.08	0.04	0.21	0.01	0.11	0.01	0.18	0.03	0.06	0.02	0.13	0.04	0.04
	CNRM-CM6-1-HR	0.04	0.02	0.01	0.05	0.01	0.00	0.13	0.06	0.02	0.04	0.06	0.03	0.03	0.03	0.00	0.03
	CNRM-ESM2-1	0.03	0.09	0.03	0.12	0.01	0.07	0.10	0.11	0.11	0.04	0.00	0.07	0.05	0.06	0.04	0.02
	FGOALS-f3-L	0.08	0.03	0.05	0.15	0.00	0.11	0.01	0.09	0.01	0.09	0.11	0.02	0.05	0.06	0.03	0.05
	FIO-ESM-2-0	0.03	0.08	0.01	0.13	0.03	0.01	0.05	0.02	0.02	0.08	0.09	0.05	0.07	0.04	0.04	0.06
	HadGEM3-GC31-LL	0.40	0.14	0.02	0.15	0.19	0.10	0.52	0.09	0.20	0.16	0.10	0.01	0.28	0.11	0.13	0.13
	INM-CM5-0	0.05	0.08	0.03	0.03	0.00	0.09	0.04	0.01	0.05	0.09	0.08	0.06	0.04	0.12	0.06	0.04
	KIOST-ESM	0.01	0.01	0.09	0.09	0.05	0.04	0.06	0.04	0.08	0.10	0.05	0.04	0.08	0.07	0.06	0.05
	MIROC6	0.11	0.11	0.02	0.02	0.04	0.15	0.05	0.20	0.01	0.19	0.03	0.17	0.02	0.19	0.04	0.06
	MIROC-ES2L	0.01	0.01	0.06	0.02	0.03	0.02	0.08	0.08	0.06	0.13	0.02	0.09	0.09	0.15	0.07	0.01
	UKESM1-0-LL	0.32	0.12	0.10	0.11	0.07	0.15	0.51	0.11	0.13	0.09	0.15	0.04	0.22	0.14	0.07	0.01
	MODEL	PC1		PC2		PC1		PC2		PC1		PC2		PC1		PC2	
		SPA	ONI	SPA	ONI	SAA	ONI	SAA	ONI	SPA	ONI	SPA	ONI	SAA	ONI	SAA	ONI
DJF	ERA5	0.08	0.28	0.11	0.01	0.14	0.28	0.14	0.01	0.17	0.02	0.25	0.18	0.08	0.02	0.09	0.18
	ACCESS-CM2	0.04	0.21	0.08	0.32	0.04	0.10	0.01	0.38	0.34	0.25	0.30	0.09	0.16	0.10	0.31	0.07
	CanESM5-CanOE	0.10	0.40	0.11	0.29	0.27	0.37	0.09	0.22	0.09	0.31	0.18	0.02	0.06	0.26	0.15	0.16
	CMCC-CM2-SR5	0.18	0.32	0.27	0.13	0.10	0.02	0.02	0.12	0.15	0.13	0.05	0.16	0.17	0.06	0.09	0.13
	CMCC-ESM2	0.13	0.14	0.16	0.31	0.18	0.45	0.15	0.17	0.03	0.14	0.04	0.06	0.12	0.11	0.01	0.07
	CNRM-CM6-1-HR	0.05	0.11	0.14	0.07	0.04	0.11	0.20	0.19	0.39	0.01	0.11	0.11	0.03	0.14	0.14	0.07
	CNRM-ESM2-1	0.19	0.00	0.05	0.06	0.17	0.20	0.07	0.14	0.30	0.33	0.29	0.11	0.25	0.21	0.15	0.29
	FGOALS-f3-L	0.01	0.46	0.03	0.19	0.07	0.37	0.07	0.27	0.32	0.50	0.23	0.04	0.09	0.38	0.22	0.23
	FIO-ESM-2-0	0.35	0.03	0.03	0.02	0.13	0.14	0.23	0.04	0.19	0.22	0.18	0.08	0.05	0.16	0.09	0.05
	HadGEM3-GC31-LL	0.27	0.01	0.06	0.17	0.13	0.15	0.08	0.21	0.35	0.28	0.13	0.04	0.06	0.17	0.10	0.15
	INM-CM5-0	0.15	0.01	0.12	0.06	0.22	0.02	0.05	0.14	0.31	0.02	0.35	0.04	0.09	0.01	0.04	0.02
	KIOST-ESM	0.12	0.35	0.46	0.05	0.17	0.01	0.03	0.36	0.35	0.31	0.24	0.19	0.01	0.19	0.16	0.12
	MIROC6	0.28	0.04	0.19	0.29	0.28	0.45	0.16	0.04	0.26	0.12	0.24	0.05	0.01	0.11	0.05	0.19
	MIROC-ES2L	0.14	0.09	0.19	0.19	0.07	0.35	0.25	0.02	0.19	0.37	0.04	0.18	0.04	0.39	0.21	0.10
	UKESM1-0-LL	0.37	0.08	0.10	0.11	0.05	0.17	0.12	0.11	0.40	0.22	0.09	0.15	0.13	0.05	0.04	0.27
	MODEL	PC1		PC2		PC1		PC2		PC1		PC2		PC1		PC2	
		SPA	ONI	SPA	ONI	SAA	ONI	SAA	ONI	SPA	ONI	SPA	ONI	SAA	ONI	SAA	ONI
JJA	ERA5	0.36	0.27	0.13	0.05	0.07	0.27	0.01	0.05	0.38	0.21	0.21	0.02	0.20	0.21	0.10	0.02
	ACCESS-CM2	0.27	0.13	0.26	0.06	0.17	0.15	0.27	0.07	0.47	0.01	0.29	0.08	0.17	0.07	0.32	0.09
	CanESM5-CanOE	0.12	0.31	0.13	0.05	0.23	0.28	0.21	0.05	0.39	0.10	0.06	0.05	0.25	0.07	0.23	0.03
	CMCC-CM2-SR5	0.04	0.20	0.38	0.39	0.06	0.21	0.21	0.05	0.35	0.09	0.22	0.23	0.16	0.07	0.07	0.17
	CMCC-ESM2	0.18	0.31	0.32	0.16	0.15	0.23	0.03	0.19	0.40	0.30	0.14	0.06	0.27	0.22	0.27	0.19
	CNRM-CM6-1-HR	0.01	0.10	0.39	0.01	0.06	0.04	0.17	0.06	0.12	0.07	0.39	0.09	0.10	0.00	0.22	0.01
	CNRM-ESM2-1	0.09	0.04	0.27	0.11	0.14	0.17	0.23	0.13	0.16	0.13	0.13	0.05	0.04	0.10	0.36	0.10
	FGOALS-f3-L	0.07	0.39	0.38	0.09	0.25	0.42	0.09	0.10	0.28	0.30	0.18	0.02	0.14	0.12	0.14	0.25
	FIO-ESM-2-0	0.15	0.34	0.33	0.09	0.18	0.21	0.14	0.14	0.40	0.33	0.36	0.10	0.19	0.19	0.16	0.30
	HadGEM3-GC31-LL	0.07	0.16	0.02	0.25	0.32	0.13	0.09	0.38	0.49	0.20	0.01	0.00	0.05	0.19	0.20	0.15
	INM-CM5-0	0.07	0.19	0.46	0.10	0.03	0.07	0.00	0.11	0.34	0.30	0.30	0.02	0.22	0.23	0.01	0.15
	KIOST-ESM	0.07	0.09	0.22	0.08	0.11	0.20	0.02	0.09	0.35	0.14	0.08	0.07	0.52	0.15	0.09	0.15
	MIROC6	0.18	0.40	0.28	0.42	0.09	0.19	0.11	0.57	0.31	0.37	0.14	0.44	0.06	0.46	0.06	0.16
	MIROC-ES2L	0.04	0.27	0.13	0.27	0.12	0.17	0.05	0.35	0.14	0.18	0.04	0.22	0.12	0.23	0.33	0.01
	UKESM1-0-LL	0.04	0.09	0.06	0.30	0.23	0.14	0.06	0.18	0.23	0.00	0.08	0.06	0.05	0.15	0.11	0.06

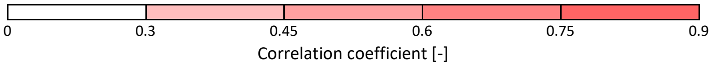

IV. EVALUACIÓN DE LA VARIABILIDAD CLIMÁTICA FUTURA QUE AFECTA A LA ENERGÍA EÓLICA Y SUS IMPLICACIONES PARA LA GENERACIÓN ENERGÉTICA EN AMÉRICA DEL SUR USANDO SIMULACIONES DE CMIP6

Resumen

La energía eólica ha experimentado un rápido desarrollo en las últimas dos décadas, posicionándose como una de las fuentes de energía renovable con mayor participación en la matriz energética global. Sin embargo, las redes eléctricas están cada vez más expuestas a la variabilidad intrínseca de estas fuentes. Este trabajo evalúa los cambios futuros en el potencial eólico y la generación de energía en América del Sur entre 2030 y 2099 y la influencia de diferentes moduladores climáticos de la variabilidad del viento a 100 m, como continuación de un trabajo previo centrado en el período histórico 1980-2014. Consideramos proyecciones de ocho modelos climáticos globales de CMIP6 bajo el escenario SSP2-4.5. Nuestros resultados muestran aumentos significativos en la densidad del potencial eólico de más del 30% para 2099 en el nordeste de Brasil, asociados principalmente a una tendencia positiva en la intensidad del Anticiclón del Atlántico Sur, mientras que se proyecta una disminución de hasta un -20% en la región de la Patagonia asociada a una tendencia positiva en el patrón Patagonia-Antártica. Estos cambios equivalen a un aumento de la generación de energía eólica de hasta un 18 % para 2069 y un 37,6 % para 2099 en el nordeste de Brasil, mientras que se proyecta una disminución de hasta un -33,6 % para 2069 y un -33,8 % para 2099 en la Patagonia. La principal contribución de este trabajo es que permite comprender los mecanismos atmosféricos que influyen en las variaciones a largo plazo del potencial eólico y la generación de energía. Esto es de gran relevancia para la industria eólica en la planificación de sistemas y la evaluación de riesgos de proyectos eólicos actuales y futuros en América del Sur.

RESEARCH ARTICLE

International Journal of Climatology, 2025

Assessing future climate variability affecting wind power and their implications for energy generation in South America using CMIP6 simulations

Ovidio Llompart[1], Héctor H. Sepúlveda[2,3], Martín Jacques-Coper[2,4,5], Marieta Hernández[6]

[1]Doctoral Program in Energy, University of Concepcion, Concepción, Chile
[2]Department of Geophysics, University of Concepcion, Concepción, Chile
[3]Centro de Estudios del Cuaternario de Fuego-Patagonia y Antártica (CEQUA), Punta Arenas, Chile
[4]Center for Oceanographic Research COPAS Coastal, University of Concepcion, Concepción, Chile
[5]Center for Climate and Resilience Research (CR2), Santiago, Chile
[6]Doctoral Program in Environmental Sciences, Mention in Continental Aquatic System, University of Concepcion, Concepción, Chile

Correspondence: Héctor H. Sepúlveda (hectorsepulveda@udec.cl)

Received: 27 August 2025

Keywords: wind power, energy generation, climate variability, CMIP6

Abstract

Wind energy has experienced rapid development over the past two decades, positioning it as one of the renewable energy sources with the largest share in the global energy mix. However, power grids are increasingly exposed to the intrinsic variability of these sources. This paper evaluates future changes in wind power and energy generation over South America between 2030 – 2099 and the influence of different climate modulators of 100m wind variability, as a continuation of a previous work focused on the historical period 1980 - 2014. We consider projections from eight CMIP6 global climate models under the moderate SSP2-4.5 scenario. Our results show significant increases in wind power density of more than 30% by 2099 over northeastern Brazil associated primarily to a positive trend in the South Atlantic Anticyclone intensity, while a decrease up to -20% is projected over Patagonia region associated to a positive trend in the Patagonia-Antarctic pattern. These changes equate to an increase in wind power generation up to 18% by 2069 and 37.6% by 2099 in northeastern Brazil, while a decrease up to -33.6 by 2069 and -33.8% by 2099 is projected for Patagonia. The main contribution of this work is that it allows us to understand the atmospheric mechanisms that influence long-term variations in wind power and energy generation. This is of great relevance for the wind energy industry in system planning and risk assessment in current and future wind projects in South America.

1. Introduction

Uncertainty about future wind power behavior implicate a potential risk to wind energy production, as a changing climate can alter atmospheric dynamics and affect wind patterns (Emodi et al., 2019; Solaun & Cerdá, 2020). A decrease in wind speed will cause a reduction in energy production, which is most noticeably reflected in sites with low mean wind speed values (Watts et al., 2017), while in contrast, a small increase will greatly benefit other regions since wind power directly depends on the wind speed cubed. In this context, it is imperative to assess the susceptibility of wind power and energy generation, with important implications for energy security and the resilience of the electricity system (Doddy Clarke et al., 2022; Peiris et al., 2021; Zhang et al., 2019).

On a global scale, a future reduction in wind power density (WPD) is projected in many regions of the Northern Hemisphere, and an increase in the Southern Hemisphere is considered possible with substantial regional variations (Chen, 2020; Davy et al., 2018; Feng et al., 2024; Karnauskas et al., 2018). Although different authors generally consider +/-10% or more variation in WPD to be significant in terms of wind energy production (De Jong et al., 2019; Tian et al., 2019), different future scenarios lead to a reduction of up to -35% in WPD in northern continental Europe and the central Mediterranean (Martinez & Iglesias, 2021). Although, (Moemken et al., 2018) found that climate change could be beneficial for regions like the Baltic and Aegean Sea.

According to Jung & Schindler (2020), climate change will likely lead to an increase in WPD across most of Brazil, South Africa, and Eastern Australia. At the wind turbine scale (80m–100m), several studies have also been conducted that are in line with these projections and offer practical benefits for assessing WPD under climate change impacts (Gugliani et al., 2021; Islek et al., 2020; Kim et al., 2021; Weber et al., 2018; Wilkie & Galasso, 2020).

According to future projections, WPD in South America is expected to increase substantially across most of Brazil, and in some locations annual energy production (AEP) could even increase by more than 40% by 2080 (De Jong et al., 2019). This result is in line with the study by Karnauskas et al. (2018) which indicates an increase in WPD for eastern Brazil of 21% by 2050 and 42% by 2099. On the other hand, Martinez & Iglesias (2024) found decreases of up to -30% west of the Andes, mainly in the southernmost areas of the Chilean coast.

The aforementioned studies show relatively robust temporal and spatial behavior in wind speed and WPD change on various emission scenarios, future time periods and simulations. Therefore, the effects of climate change should be considered in the development of wind power projects (Devis et al., 2018; Ganea et al., 2018). However, most of these studies are inconclusive regarding the causes of such changes in wind speed and its variability.

Natural climate variability is caused by periodic oscillations (months, years, decades) in the atmospheric circulation that strongly modulate wind speed across different regions of the world.

Electrical grids are increasingly exposed to climate variability due to the incorporation of renewable sources such as wind power (Foley et al., 2012); however, climate oscillations and wind variability are often not taken into account in wind farms campaigns, which is important when considering wind resource assessment and long-term planning (Barbosa De Alencar et al., 2017; Bianchi et al., 2022). Therefore, additional studies are necessary to explore the mechanisms associated with wind power variability (Gao et al., 2019).

1.1. Study area

Due to its considerable southern extent and prominent orography, South America exhibits diverse weather and climate patterns, including tropical, subtropical, and extratropical characteristics. These characteristics in turn reflect on wind and WPD variability in the region. With over 25,000 km of coastline, South America has a great WPD, especially along the coasts of Brazil, Colombia, and southern Chile (Shadman et al., 2023), as shown in Figure 1a.

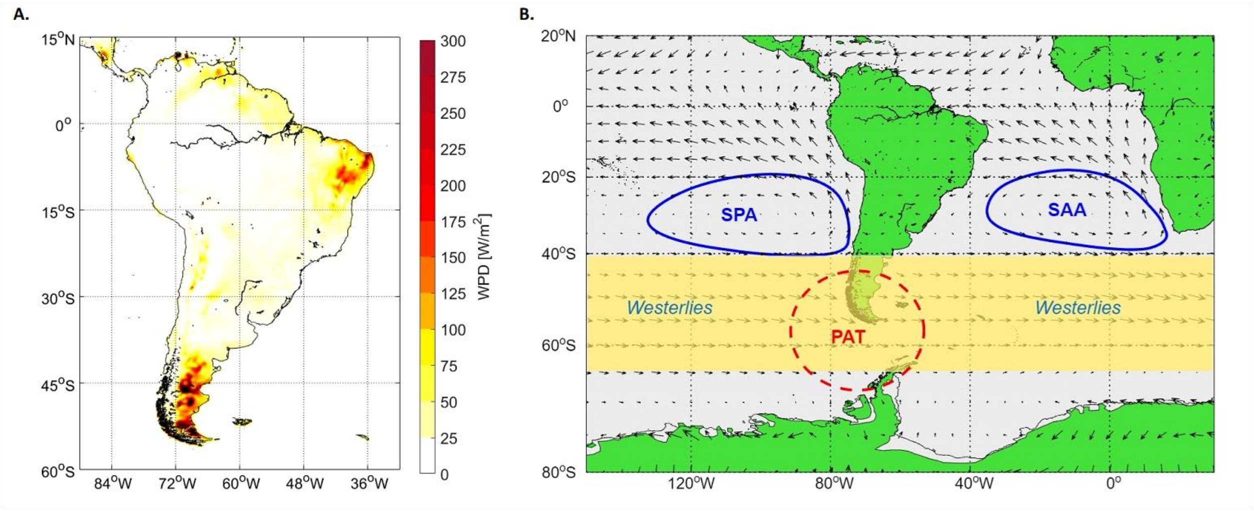

Figure 1. a) Distribution of WPD at 100m in South America. b) Schematic diagram of the mean annual 100m wind field and its main large-scale modulators over South America. Source: ERA5 data 1980–2014.

The Andes extend continuously close to the western coast of the continent and therefore represent a major obstacle to tropospheric flow, with dry conditions to the west and wet conditions to the east in tropical/subtropical latitudes. The Brazilian Plateau also tends to block low-level circulation over subtropical South America. South of 40°S, low-level westerly flow prevails year-round over the adjacent oceans and the continent. Over the southern tip of South America and the adjacent South Pacific, westerly winds are stronger, peaking between 45°S and 55°S (Garreaud et al., 2009).

Different analytical techniques and data sets in South America have produced many atmospheric patterns that influence the region climate variability (Bianchi et al., 2017; Codron, 2005; Montini et al., 2019; Watts et al., 2017). Particularly in the case of WS100 and therefore WPD, most of the variability resides in a few patterns of the sea level pressure (SLP) field: the South Atlantic Anticyclone (SAA), the Southeast Pacific Anticyclone (SPA), the Patagonia-Antarctic Pattern (PAT), and the Antarctic Oscillation (AAO) (Llompart et al., 2025). Both the SAA and the SPA are semi-permanent high-pressure centers (Figure 1b) with a marked annual cycle that peaks during the austral winter and strongly modulates the climate of South America (Ancapichún & Garcés-Vargas, 2015; Cabos et al., 2017). Meanwhile, the PAT and the AAO are patterns that arise from the interaction between flows from the Antarctic polar region and mid-latitudes (Garreaud et al., 2009; Llompart et al., 2025).

The SAA affects the tropical South Atlantic basin, and its seasonal cycle is mainly controlled by convective heat sources over South America and southern Africa, and by the interaction between orography with the easterly trade winds and mid-latitude westerlies (Miyasaka & Nakamura, 2010; Rodwell & Hoskins, 2001). These fundamental mechanisms lead to an SAA that is notably stronger during the austral winter than during the summer (Cabos et al., 2017). SAA is the dominant mode of wind speed variability at 100m height (WS100) in northeastern Brazil and, to our knowledge, the only large-scale pattern with which it presents a significant relationship in that region (Llompart et al., 2025). This relationship is positive and stronger during winter, meaning that as SAA intensity increases, so does WS100 in northeastern Brazil and vice versa.

The SPA is centered over the Southeast Pacific basin and primarily influences the Chilean coast, with a predominant southwesterly flow. The SPA also contributes to the mechanisms that cause variations in the pressure gradient and the intensity of westerlies over the Patagonian region, south of approximately 40°S (Llompart et al., 2025).

PAT is a Drake Passage-centered SLP anomaly pattern, identified in a previous study (Llompart et al., 2025), which is the main modulator of WS100 over the Patagonian region, south of 40°S. Over this region, WS100 increases when a low-pressure center forms west of the Antarctic Peninsula. This situation, in combination with an increased intensity of the SPA, causes an increase in the pressure gradient and the intensity of the westerlies over the Patagonian region; this situation corresponds to a negative PAT index. On the other hand, when the SLP field shows an anticyclonic curvature configuration over the Drake Passage (a positive PAT index), the westerlies shift further south in this area, causing a weakening of WS100 over Patagonia.

The AAO is the main pattern of tropospheric circulation variability south of 20°S and is characterized by pressure anomalies of one sign centered over Antarctica and anomalies of opposite sign in a circumglobally band between 40°S and 50°S (Thompson & Wallace, 2000). The AAO signal extends coherently into the lower stratosphere and appears to arise from the interaction between eddies and the zonal mean flow (Codron, 2005). In a previous study (Llompart et al., 2025), we found that AAO is the second modulator responsible for WS100 variability in Patagonia, mainly in summer. The positive phase of the AAO causes an increase in WS100 in the extreme south of Patagonia and a decrease north of 45°S.

Several studies have investigated the influence of these and other atmospheric patterns on South America climate, but a more robust understanding of their influence in WPD and, consequently in future wind power generation remains lacking. Therefore, the main objective of this research is to describe future WPD behavior and changes in wind power generation, providing better understanding of the fundamental mechanisms that drive that behavior. The insights from our investigation offer valuable perspectives for energy policy, long-term system planning and risk assessment in current and future wind projects in developing regions such as South America.

2. Methodology

2.1. Data

CMIP6 provides climate variables data for historical simulations and daily and monthly global climate projections from many experiments, models, and time periods. These global climate models (GCMs) have been used by several authors to study the behavior of the wind resource (Carvalho et al., 2021; Deng et al., 2022; Qian & Zhang, 2021; Wu et al., 2020; Zhang et al., 2019). The CMIP6 databases are available online from the website of the European Union's Earth observation program, Copernicus (https://cds.climate.copernicus.eu/). CMIP6 represents a substantial expansion over its predecessor, CMIP5, in terms of the number of participating modeling groups, the number of future scenarios examined, and the number of different experiments performed.

For this study, two future time periods were defined: a medium-term period from 2030 to 2069 and a long-term period from 2070 to 2099. The historical period from 1980 to 2014 and the ERA5 reanalysis data were used as a baseline to compare differences with future periods. Eight CMIP6 models were selected (Table 1), which best represent the relationships between WS100 and its climate modulators over South America, analyzed in a previous study (Llompart et al., 2025). Since each model has different map projections and resolution, a homogeneous grid of 1°x1° spatial resolution was defined for convenience when working with and comparing models. The bilinear interpolation method was applied using the software *Climate Data Operators* (CDO) from the Max Planck Institute (Greene et al., 2019). All steps described for data preparation and analysis were implemented using the software Matlab.

Table 1. CMIP6 global models used. (More information at https://pcmdi.llnl.gov/CMIP6/)

CMIP6 model	Resolution (°Lon x °Lat)		Variant label	Reference	Country of origin
	Wind speed	SLP			
ACCESS-CM2	1.88 x 1.25	1.88 x 1.25	r1i1p1f1	Bi et al. (2020)	Australia
CanESM5-CanOE	2.81 x 2.81	2.81 x 2.81	r1i1p2f1	Swart et al. (2019)	Canada
CMCC-CM2-SR5	1.25 x 0.94	1.25 x 0.94	r1i1p1f1	Cherchi et al. (2019)	Italy
CMCC-ESM2	1.25 x 0.94	1.25 x 0.94	r1i1p1f1	Lovato et al. (2022)	Italy
CNRM-CM6-1-HR	0.50 x 0.50	0.50 x 0.50	r1i1p1f2	Voldoire et al. (2019)	France
CNRM-ESM2-1	1.41 x 1.41	1.41 x 1.41	r1i1p1f2	Séférian et al. (2019)	France
FGOALS-f3-L	1.25 x 1.00	1.25 x 1.00	r1i1p1f1	He et al. (2020)	China
FIO-ESM-2-0	1.25 x 0.94	1.25 x 0.94	r1i1p1f1	Bao et al. (2020)	China

CMIP6 models only provide near-surface wind speed data (10m). Power law is a method commonly used by various authors (Manwell, n.d.; Tobin et al., 2015, 2016; Weber et al., 2018) to extrapolate wind speed to turbine height:

$$WS100 = v_0 \left(\frac{z_h}{z_0}\right)^{\alpha} \tag{1}$$

Where v_0[m/s] is the near-surface wind speed, α represents the wind shear exponent, which is typically equal to 0.143 (Li et al., 2022; Tian et al., 2019). It was set as turbine height z_h= 100m, while near surface z_0= 10m. Then, WPD $[W/m^2]$ directly depends on the wind speed (WS100) cubed and was calculated according to the equation:

$$WPD = \frac{1}{2}\rho v^3 \tag{2}$$

where $\rho$$[kg/m^3]$ is the air density which, although some research assumes it as a constant value, in our case and given the extension and complexity of the study area, we estimate it in the following way (De Souza Ferreira et al., 2024; Sawadogo et al., 2021):

$$\rho \cong \frac{353.4\left(1 - \frac{z_h}{45271}\right)^{5.2624}}{T} \tag{3}$$

Where z_h= 100m is the turbine height and $T$is the air temperature [K]. Since climate models do not provide air temperature at 100m, this variable was estimated considering the vertical rate of the saturated adiabatic of the atmosphere, according to which the air temperature decreases at approximately 0.6°C every 100m (De Souza Ferreira et al., 2024):

$$T = T_{2m} - \Gamma_{sat} \tag{4}$$

where T_{2m}[K] is the temperature of the air near the surface (2m) and $\Gamma_{sat}$is the vertical rate of the saturated adiabatic of the atmosphere, which for a height of 100m has a value of Γ_{sat}= 0.6.

2.2. Future WPD variations and selection of regions of interest

After obtaining the spatiotemporal distribution of WPD from WS100 over the entire study area for each model, the differences in mean WPD in each future period with respect to the historical period were calculated. Since our research is primarily focused on the wind industry, it is important to identify regions with significant WPD changes. To do that, we established a threshold of mean WS100 ≥ 3 m/s, given that for lower wind speeds the blades of the reference wind turbine do not move. In this case, 3 m/s is the *cut -in* wind speed, as shown in Figure 2 of section 1.1 of the Introduction. In this way, we ignore those areas where WS100 has values lower than 3 m/s during the historical period and does not show increases in the future. This allows us to consider only the areas that were above this threshold and show changes in the future, as well as possible areas that exceeded this threshold and could be considered new areas of interest.

After calculating the differences, we identified the regions with significant changes in WPD that were consistent with at least 80% of the models analyzed in terms of sign, i.e., increase or decrease. We then constructed the time series of mean WS100 anomalies and compared them with ERA5 over the historical period, considering criteria such as the behavior of the annual cycle and the distribution of the series, to understand the performance of the CMIP6 models in reflecting the behavior of WS100 in the regions of interest. In addition, we constructed the time series of mean WPD anomalies in each region and analyzed their trend for each model until 2099 to compare it with the trend in atmospheric patterns.

2.3. Climate modulators and their influence on WS100 and WPD

To investigate the physical processes of atmospheric circulation and their relationship with WS100 behavior in the regions of interest, four wind climate modulators in the region were considered: SAA, SPA, PAT, and AAO. The index to measure the SPA intensity is calculated from the monthly SLP anomalies within the area between 15°S-50°S and 150°W-70°W (Ancapichún & Garcés-Vargas, 2015; Llompart et al., 2025). A similar index is determined for the SAA in the area between 10°-40°S and 40°W-10°E (Llompart et al., 2025; Lübbecke et al., 2014), and for the PAT, within the region delimited by 40°-70°S and 60°-90°W (Llompart et al., 2025).

To calculate the AAO index (Figure 2, right) we used the definition proposed by Marshall (2003), which is based on the difference of the normalized SLP anomalies between 40°S and 65°S around the globe and we applied the algorithm developed by (Greene et al., 2019) for Mathworks ® Matlab.

For each region of interest detected, we calculated monthly (MON) and seasonal anomalies of WS100 for the summer period from December to February (DJF) and the winter period from June to August (JJA). Then, we calculated the correlation coefficient R between WS100 anomalies and the SAA, SPA, PAT, and AAO indices. Pearson's method was used with a 95% confidence interval, which is independent of the scale of measurement of the variables and is frequently used to measure the degree of relationship between two variables, provided both are quantitative and continuous.

2.4. Estimation of AEP

To calculate the variations in AEP in the future periods 2030–2069 and 2070–2099 with respect to the historical period 1980–2014, it is necessary to know the frequency distribution of the mean hourly wind speed for each of the periods. A large literature has reported that applying the Weibull distribution to model wind speed data adequately reproduces the wind speed regime. The probability density function (PDF) of the Weibull distribution is expressed as follows:

$$f(v_i) = \frac{k}{c}\left(\frac{v_i}{c}\right)^{k-1} exp\left[-\left(\frac{v_i}{c}\right)^{k}\right] \tag{5}$$

Where v_i, c and k are the mean wind speed (WS100), the scale parameter and the shape parameter respectively. However, since the wind speed data provided by the CMIP6 models in most cases have a maximum daily temporal resolution (3 hours in a few cases), it is necessary to estimate the hourly frequency distribution. We use the methodology proposed by Shin et al., 2018 to estimate the parameters of the Weibull PDF from daily data, which are available for the models used, except for CanESM5-CanOE and FGOALS-f3-L.

The method consists of first calculating the 1st and 2nd order cumulative raw moments (CRMs) of the wind speed data corresponding to coarser time scales. For example, if daily mean wind speed data are available (as in our case), the mean wind speeds for coarser time scales (i.e., 2, 3, 4, …, and even 30 days) are calculated by aggregating the daily mean wind speed data. The CRMs are then calculated from the 2, 3, 4, …, and 30-day daily mean wind speed data (converted into sample raw moments):

$$h^{th}\ order\ sample\ raw\ moment = \mu_R^h = \frac{1}{n}\mu_{CR}^h = \frac{1}{n}\sum_{i=1}^{n} v_i^h \tag{6}$$

A linear model is then constructed between the logarithm of the CRMs and the logarithm of the time scales. The CRMs corresponding to the specific time scale of interest, for example, 1 h (as in our study), are then estimated from the linear model generated previously. The CRM estimates are then converted into central moments. Since CRMs cannot be directly applied to fit the probability distribution, they must be converted into the central moments commonly used in the method of moments.

$$1^{st}\ order\ sample\ central\ moment = \mu_C^1 = \mu_R^1 \tag{7}$$

$$2^{nd}\ order\ sample\ central\ moment = \mu_C^2 = \mu_R^2 - (\mu_C^1)^2 \tag{8}$$

Finally, the parameters of the Weibull PDF are estimated using the method of moments with central moment estimates. The theoretical 1st and 2nd order central moments of the Weibull distribution are expressed as follows:

$$\mu_C^1 = c\Gamma\left(1 + {}^{1}/_{k}\right) \tag{9}$$

$$\mu_C^2 = c^2\left[\Gamma\left(1 + {}^{2}/_{k}\right) - \Gamma^2\left(1 + {}^{1}/_{k}\right)\right] \tag{10}$$

Where Γ() is the gamma function. The method of moments for the Weibull distribution identifies the parameters that produce theoretical 1st and 2nd order moments equivalent to the 1st and 2nd order sample moments. This problem was solved using a numerical optimization method in Matlab. Then, once the Weibull PDF is known, AEP was calculated according to the equation:

$$E = T\sum_{i=1}^{N} P(v_i)f(v_i)\Delta v_i \tag{11}$$

Where $P(v_i)$[W] is the power at speed v_i, $f(v_i)$is the probability of the wind having the speed $v_i$according to the Weibull distribution, $\Delta v_i$is the width of the speed interval, that is, the difference between the values of $v_i$adjacent , and T is the total time (considering one year: T = 8760 hours). The values of $P(v_i)$, as shown in Figure 2, were obtained from the characteristic power curve of the Vestas wind turbine V126-3.45MW, commonly used as a reference in studies focused on onshore wind generation (Bianchi et al., 2022; De Jong et al., 2019; Russo et al., 2023). This turbine has a cut -in speed of 3 m/s, cut - out of 22.2 m/s, and a nominal power of 3.45 MW (*https://www.vestas.com*).

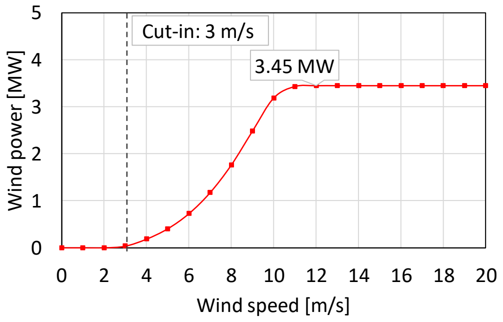

Figure 2. Power curve of the Vestas V126-3.45 MW wind turbine used as a reference for calculating AEP.

3. Results

3.1. WPD changes in the future compared to the historical period

As shown in Figure 3 and Figure 4, as a result of averaging the WPD obtained for each model, the highest WPD in the future are over the northeast and southeast of Brazil with values of up to 300 W/m^2 near the coast, Uruguay, the central east and southeast of Argentina, increasing towards the extreme south of the country over Patagonia with values exceeding 300 W/m^2. Chilean Patagonia also shows high WPD values and towards the north of Chile over the Andes on the border with Argentina, which is best appreciated in winter with values of up to 300 W/m^2.

Regarding the differences of WPD in the future compared to the historical period, there are areas with significant variations. For the period 2030-2069, increases of up to 30 W/m^2 are observed, mainly in winter, over northeastern Brazil and the northern Andes Mountains on the border of Chile and Argentina, representing an increase of up to 30% for these regions. Over northeastern Argentina, an increase of up to 20 W/m^2 is also observed, representing a 20% increase compared to the historical period. In contrast, for the Patagonia region, approximately between 40°S - 50°S, areas with a difference of -30 W/m^2 are observed, representing a decrease of up to 15% in WPD.

For the period 2070-2099, the changes observed during 2030-2069 are accentuated. Largely, increases are sustained in most of Brazil, northern Chile, and northwestern Argentina, with northeastern Brazil in particular showing increases of more than 30%. The decrease prevails over much of Patagonia, central Argentina, and parts of Uruguay, with values as low as -20%. It is important to note that the areas with decreasing WPD previously showed wind speeds of at least 3 m/s, including the Patagonian region, which is currently one of the areas with the highest WPD values. This is also why the Patagonian region, although showing changes of similar magnitude (albeit opposite in sign) to those in northeastern Brazil, represents a smaller percentage of variation compared to the historical period.

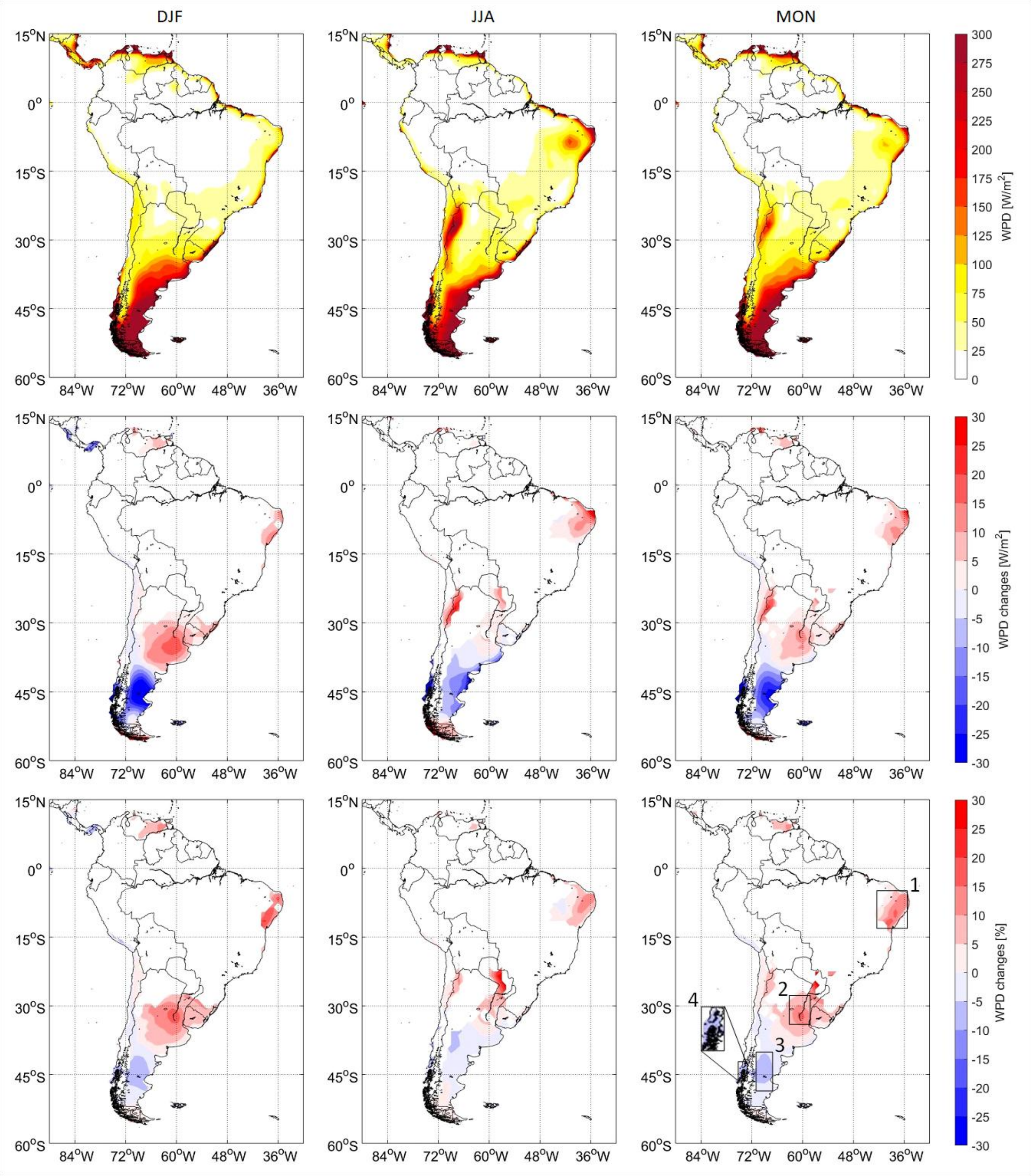

Figure 3. (Top panels) Mean WPD for the period 2030-2069, (middle panels) changes in WPD for 2030-2069 with respect to 180-2014, and (bottom panels) changes in WPD expressed as percentage with respect to the mean WPD from 1980-2014. These figures show the ensemble signal of all CMIP6 models used in this study.

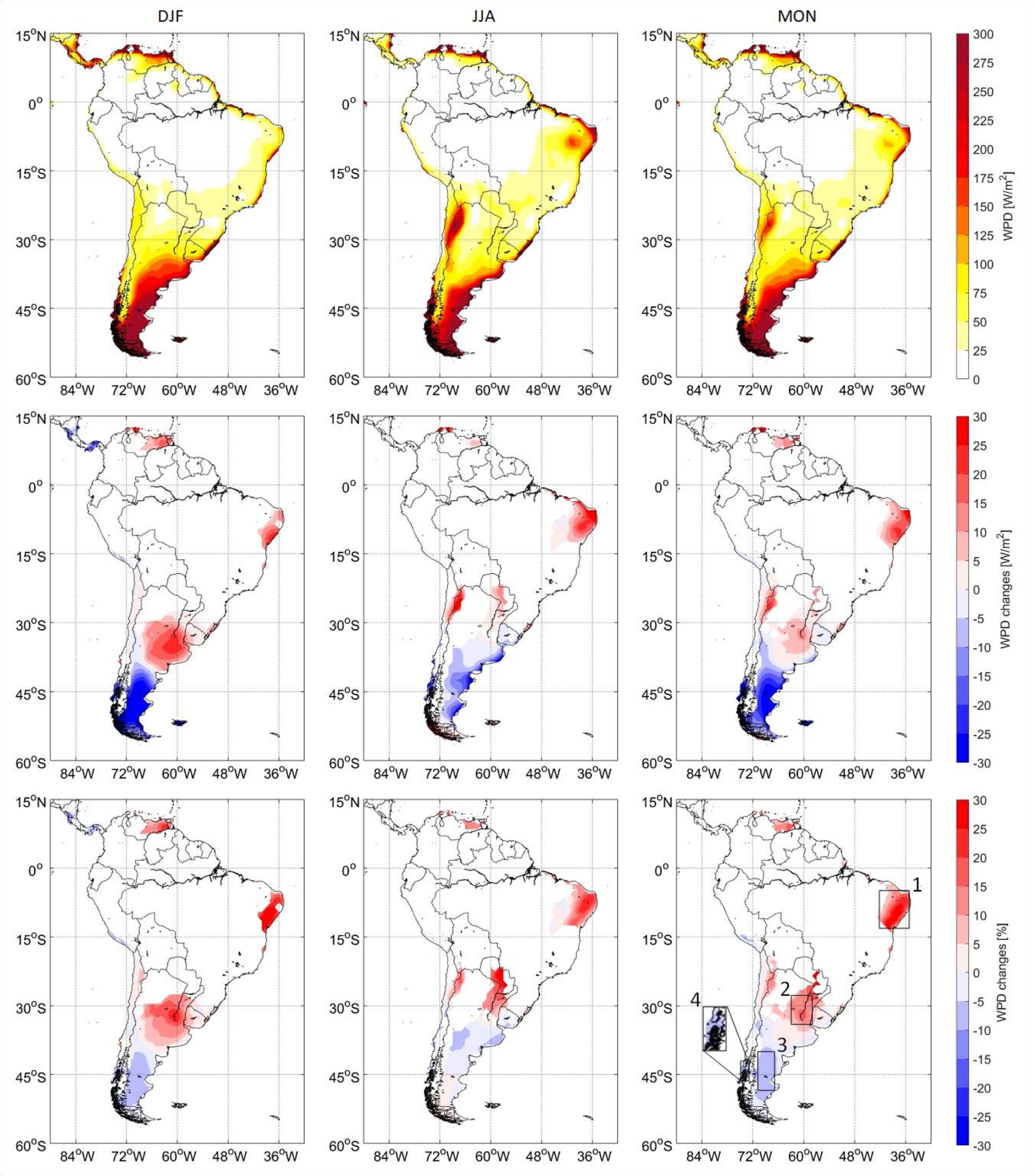

Figure 4. (Top panels) Mean WPD for the period 2070-2099, (middle panels) changes in WPD for 2070-2099 with respect to 180-2014, and (bottom panels) changes in WPD expressed as percentage with respect to the mean WPD from 1980-2014. These figures show the ensemble signal of all CMIP6 models used in this study.

After analyzing the most significant WPD changes, we selected four regions of interest as shown in the lower right panel of Figures 3 and 4. Region 1 comprises the most extreme portion of northeastern Brazil between 5°S – 13°S and 35°W – 42°W, region 2 comprises northeastern Argentina near the borders with Uruguay and Paraguay between 28°S – 34°S and 58°W – 63°W, region 3 comprises the portion of Argentine Patagonia between 40°S – 48°S and 67°W - 71°W, and finally region 4 comprises a small portion of Chilean Patagonia delimited by 42°S – 46°S and 73°W – 76°W. The most significant appreciable WPD changes are concentrated in each of these regions, of at least +/-10% with respect to the historical period. In addition, numerous wind farms are currently operating in these areas.

Other regions with significant increases in WPD, such as the extreme north of Chile on the border with Argentina and parts of the extreme northwest of Argentina, were not considered because they are areas with complex topography crossed by the Andes, where CMIP6 models do not accurately reflect wind behavior and its interaction with atmospheric patterns (Llompart et al., 2025). Increases in WPD have also been observed in northern Venezuela, but to date, there are no data on wind farms in operation or projected in this region.

3.2. WS100 behavior in the regions of interest during the historical period

As shown in Figure 5, the behavior of the WS100 annual cycle over the historical period is quite similar between models and compared to ERA5 for each of the regions of interest. In the case of northeastern Brazil and northeastern Argentina, the maximum is observed towards the end of winter and beginning of spring, while the minimum occurs towards the end of summer and beginning of autumn, with anomalies that oscillate on average between -3 and 3 m/s throughout the year. In the case of Argentinean Patagonia, WS100 reaches its maximum during summer, between the months of December and February, and decreases during autumn and winter, between the months of March and August, and then begins to rise again in spring from September, with anomalies that oscillate on average between -3 and 3 m/s throughout the year. Finally, in Chilean Patagonia, a main maximum is observed in winter between the months of June and August and a secondary maximum in summer between December and February, with minimums during the spring and autumn seasons, with anomalies that oscillate on average between -3 and 3 m/s throughout the year.

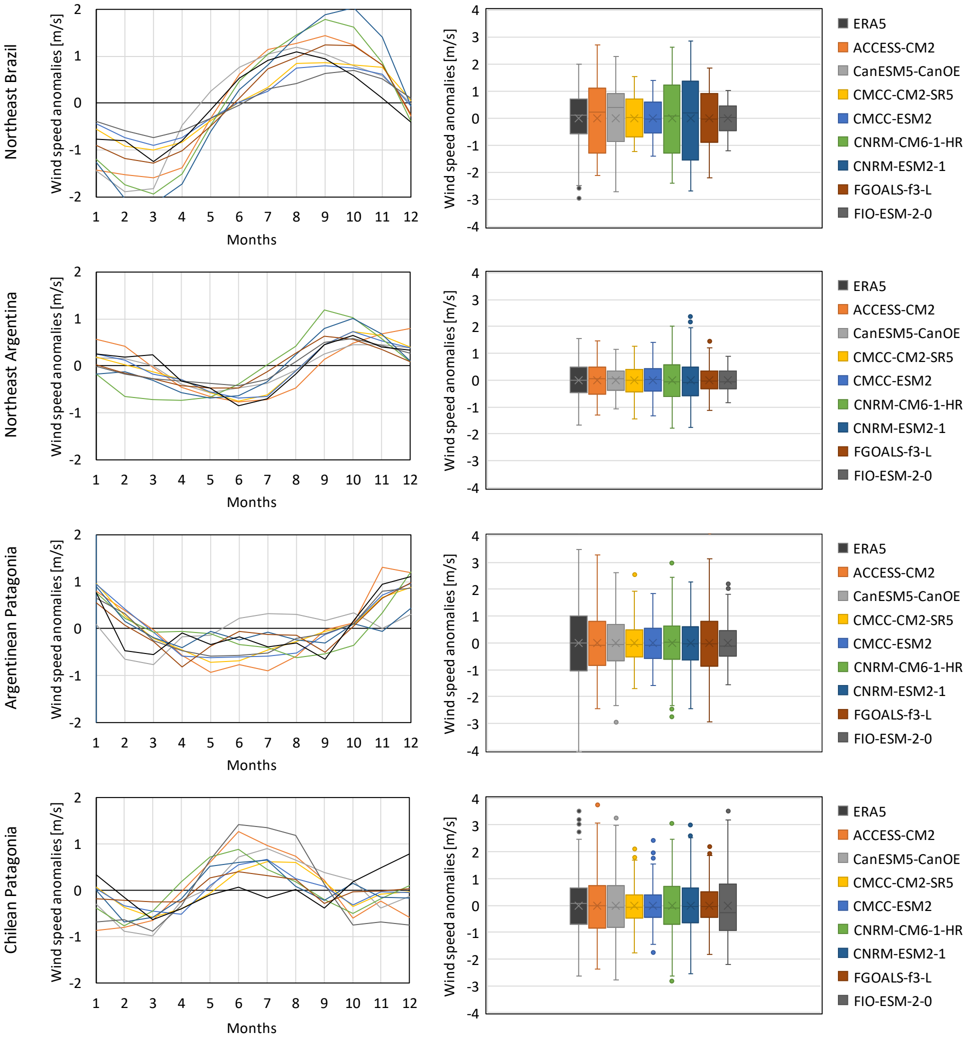

Figure 5. Annual cycle of WS100 anomalies (left panels) and boxplots showing the distribution of the WS100 monthly anomalies (right panels) during the historical period 1980-2014 for all CMIP6 models used in this study; each line shows a region of interest.

3.3. Climate modulators behavior in the future and influence on WPD in the regions of interest

In the case of the climatic indices analyzed, the CMIP6 models show great similarities in their behavior during the future period 2015 - 2099 as shown in Figure 6. The positive and negative phases of both the SAA and the SPA show a frequency-lock to the annual cycle with a maximum/minimum during the winter between the months of June and August, while the anomalies oscillate mainly in the range of -4 to 4 hPa for the SAA and -6 to 6 hPa for the SPA.

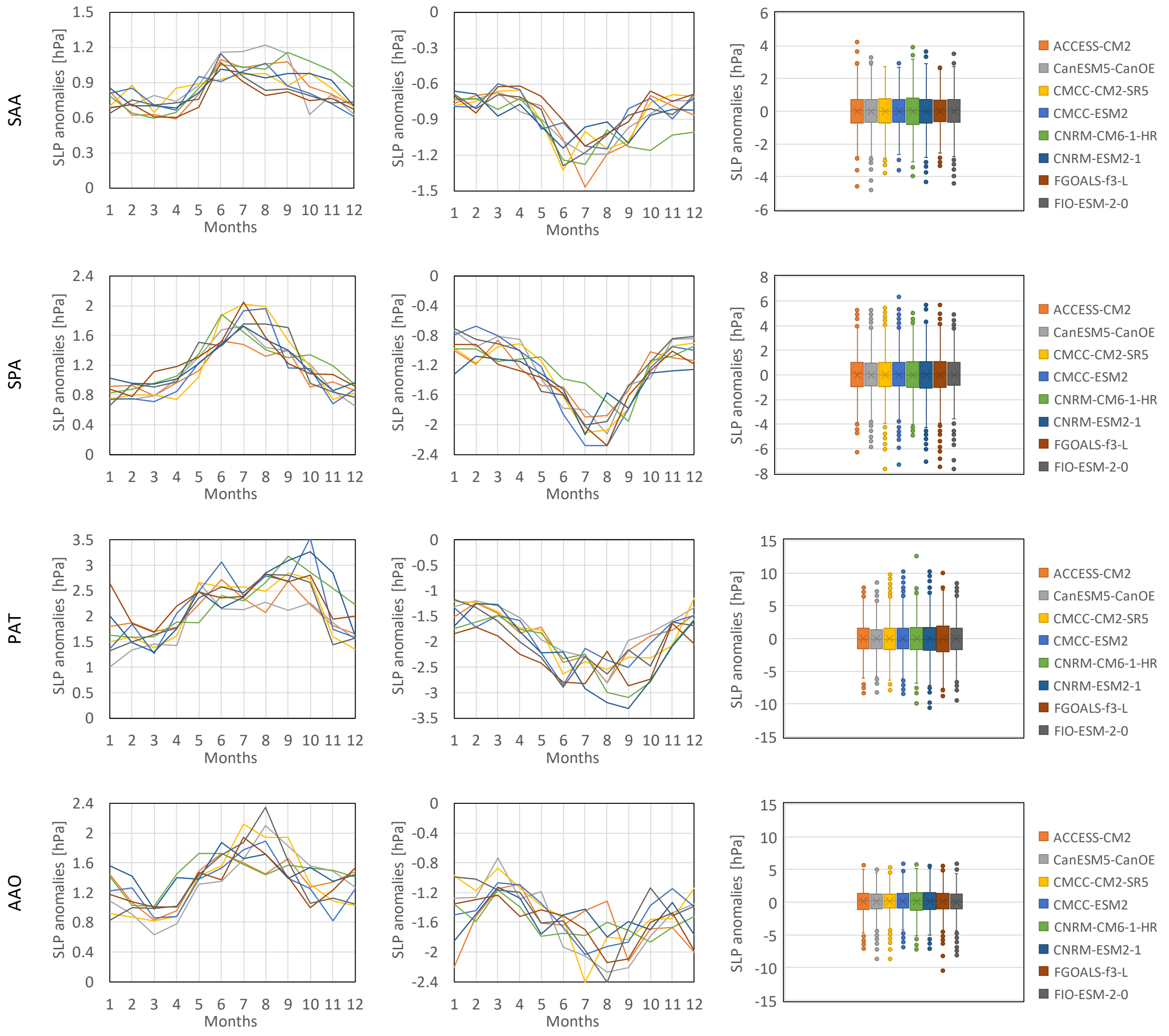

Figure 6. Behavior of the mean annual cycle of SLP during opposite phases of the climate indices analyzed during the period 2015-2099: (left column) positive phase, (center column) negative phase, and (right column) boxplots for the distribution of the monthly anomalies. Each line corresponds to a single climate modulator, as defined in the text.

In the case of PAT, a frequency-lock to the annual cycle is also observed, with maximum/minimum values for the positive/negative phase extending from late autumn to mid-spring, and anomalies that oscillate mainly between -10 and 10 hPa. Finally, the AAO exhibits two maximum/minimum peaks for its positive/negative phase: a main peak during winter and early spring, between June and September, and a secondary peak during winter, between December and February, with anomalies that oscillate mainly between -5 and 5 hPa throughout the year.

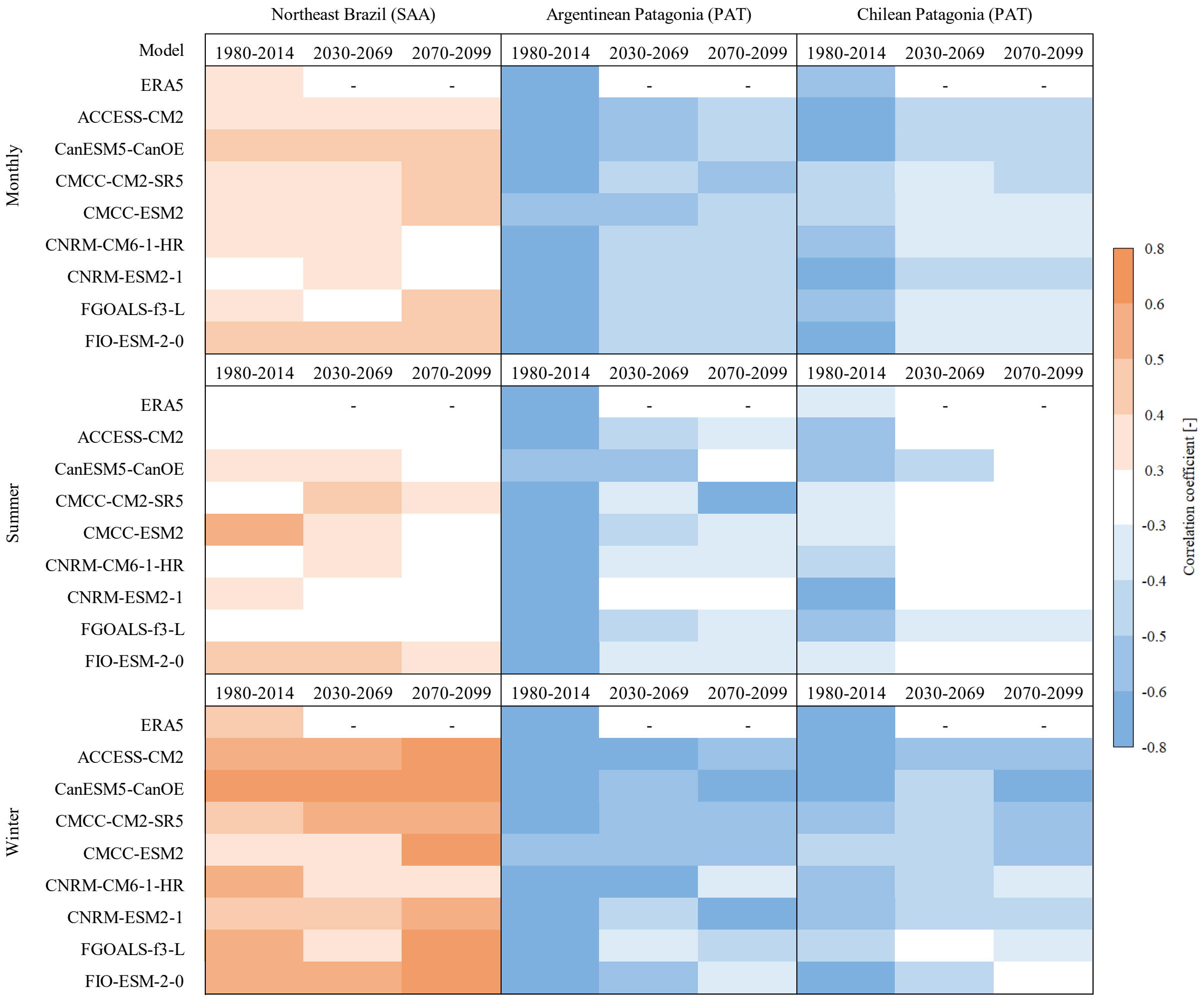

Figure 7. Correlation coefficient R between WS100 and the climate modulators that influence each region.

To assess the influence of the analyzed atmospheric patterns on the behavior of WS100 and verify the persistence of this influence over time, correlation coefficient R between the climate indices and WS100 were calculated for each region of interest, as shown in Figure 7. The correlations between SAA and WS100 are shown over northeastern Brazil, and the correlations between PAT and WS100 over Argentine and Chilean Patagonia. As can be seen, in most cases, the influence of these patterns is more pronounced during winter than in summer, even disappearing almost completely in some cases. The northeastern region of Argentina (not shown) did not present significant correlations with any of the analyzed patterns. The AAO only presented very low correlations with the regions of Patagonia, which is probably because it is a secondary modulator.

Over northeastern Brazil, the influence of the SAA increases considerably toward the future, especially in winter, increasing from R ~ 0.5 to 0.62. For the monthly series, R increases from ~ 0.37 to 0.41. In summer, the correlation coefficients are quite low in most cases. In the case of both Argentine and Chilean Patagonia, the influence of the PAT decreases considerably toward the future, especially in summer, where R changes from ~ -0.68 to -0.36 on the Argentinean side and from R ~ -0.48 to -0.16 on the Chilean side. During winter, the change is also noticeable, although not as drastic as in summer, increasing from R ~ -0.65 to -0.51 on the Argentinean side and from R ~ -0.6 to -0.46 on the Chilean side. Regarding the monthly series, for Argentina R changed from ~ -0.66 to -0.47, while for Chile R went from ~ -0.59 to -0.41. The northeastern region of Argentina did not show significant correlations with any of the patterns analyzed.

Regarding the future trend of climate indices between 2015 and 2099, as observed in Figure 8, all models show a positive trend with little change in variance and a shift in the mean between 0.5 and 1 HPa in most cases. On the other hand, regarding the future trend of WPD shown by the models between 2015 and 2099, as observed in Figure 8, the northeastern region of Brazil shows a significant upward trend, which is more noticeable in winter, while the variance is conserved with a change in the mean of approximately 0.4 m/s. In the case of northeastern Argentina, the trend is not as evident, except for some models such as CanESM-CanOE, which show an increase with a change in the mean of 0.8 m/s, while the variance remains unchanged for most models. In both Argentine and Chilean Patagonia, a downward trend is observed, with an approximate change in the mean of 0.4 m/s and no appreciable variance.

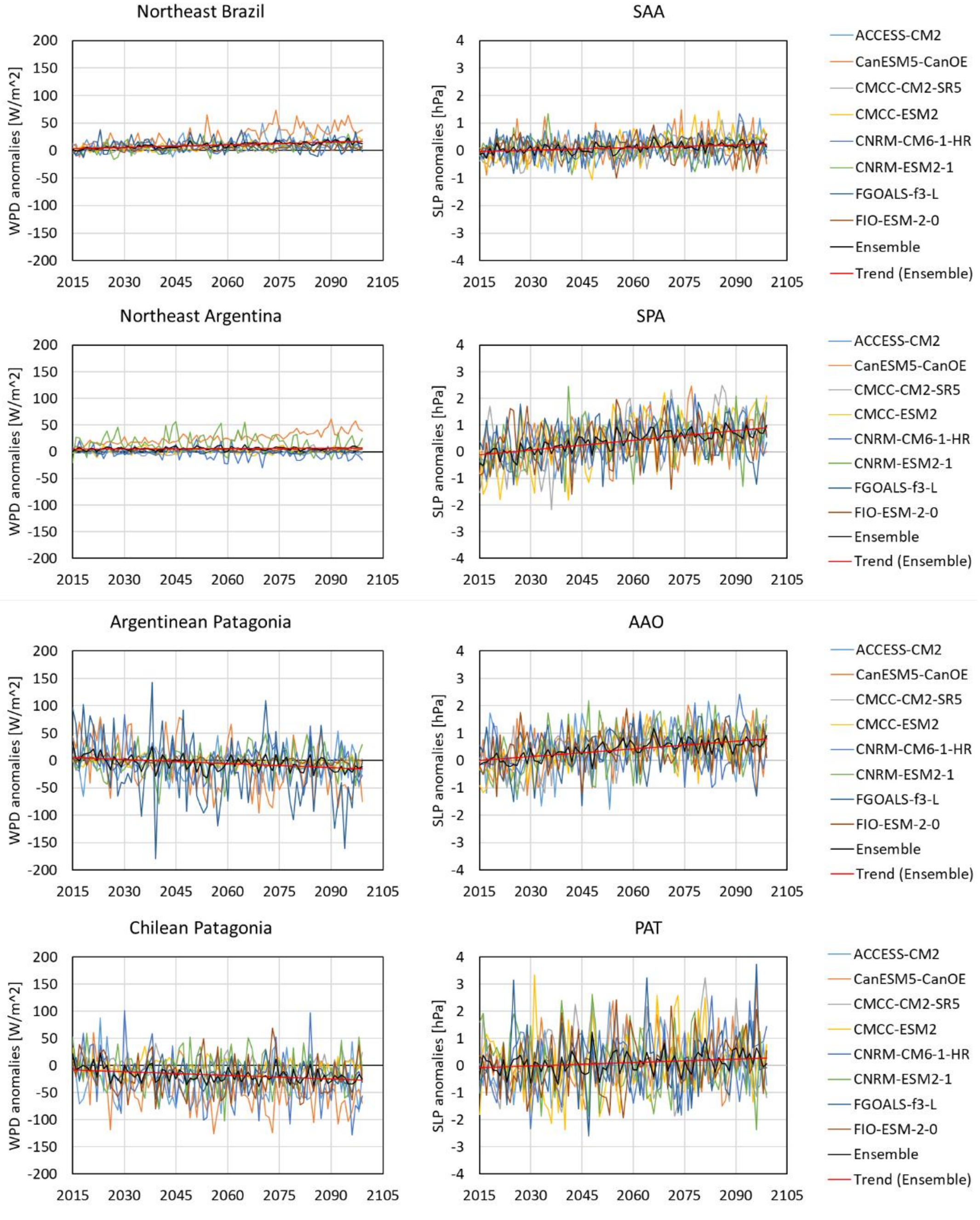

Figure 8. Trend in the annual WPD series (left panels) and in the climate modulators (right panels) over the period 2015-2099 (the mean value of the historical period 1980-2014 was set as 0 for 2015).

If we compare the trends between atmospheric patterns and WPD for each region, some important points can be seen. In the case of SAA, the trend is positive, as is the WPD over northeastern Brazil, which makes sense since it is the main modulator of WPD over that region with a positive influence. In the case of both Chilean and Argentine Patagonia, the WPD trend is negative, while the PAT trend is positive. This is also consistent since PAT is the main modulator of WPD over these regions with a negative influence. Therefore, it makes sense that if the PAT trend is positive, the WPD trend is decreasing.

3.4. Estimation of Weibull PDFs and future changes in AEP

To measure the accuracy of (Shin et al., 2018) method in estimating Weibull PDFs, we calculated the WS100 daily mean from hourly ERA5 data and applied the proposed methodology. We then compared the estimated PDFs with those obtained directly from the hourly data (Figure 9). As can be seen, there are differences that change the frequency distribution of wind speeds for each region, the most notable being an underestimation of the mean and a slight increase in the variance. This, in turn, influences the AEP, which in all cases is lower than the "true" annual generation. Table 2 shows the total AEP for each region and the associated error resulting from the estimation. In the case of northeast Brazil, the error is -5.4%, in the case of northeast Argentina it is -11.2%, while for the Argentinean and Chilean parts of Patagonia the error is -17.1% and -16.6% respectively.

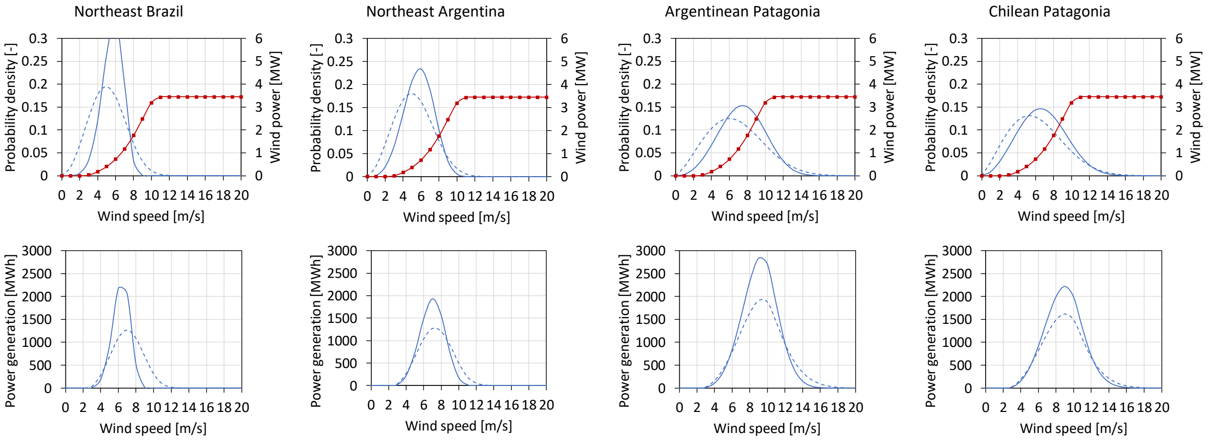

Figure 9. Weibull PDFs of annual wind speed estimated through the method of moments from (dashed lines) daily mean data and (solid lines) those calculated from hourly data, using ERA5 for each of the regions of interest during 1980–2014; the red curve represents the power curve of the of the Vestas V126-3.45 MW wind turbine. (Bottom panels) Annual wind generation curves (bottom panels) calculated from PDFs estimated using the method of moments (dashed lines) and those calculated from hourly data (solid lines).

Table 2. Differences in AEP (one turbine) and capacity factor (CF) calculated from hourly ERA5 data and those calculated from estimated PDFs.

ERA5 reanalysis	Northeast Brazil		Northeast Argentina		Argentinean Patagonia		Chilean Patagonia	
	AEP (GWh)	CF (%)	AEP (GWh)	CF (%)	AEP (GWh)	CF (%)	AEP (GWh)	CF (%)
Hourly data	5.9	19.6	6.9	22.8	14.2	47.0	11.8	39.0
Estimated PDFs	5.6	18.5	6.1	20.2	11.8	39.0	9.8	32.5
Error	-0.3	-5.4	-0.8	-11.2	-2.4	-17.1	-2.0	-16.6

Figure 10 shows the evolution of the estimated Weibull curves for each model during the historical and future periods, while Figure 11 shows the AEP curves for each region, which is summarized in Table 3. As can be seen in the case of northeast Brazil, there is an increase in AEP between 0.8 and 18.0 % for the period 2030 - 2069, while for the period 2070 - 2099 the increase doubles with values between 3.3 and 37.6 %, except for the CNRM-CM6-1-HR model, which shows a decrease in both periods.

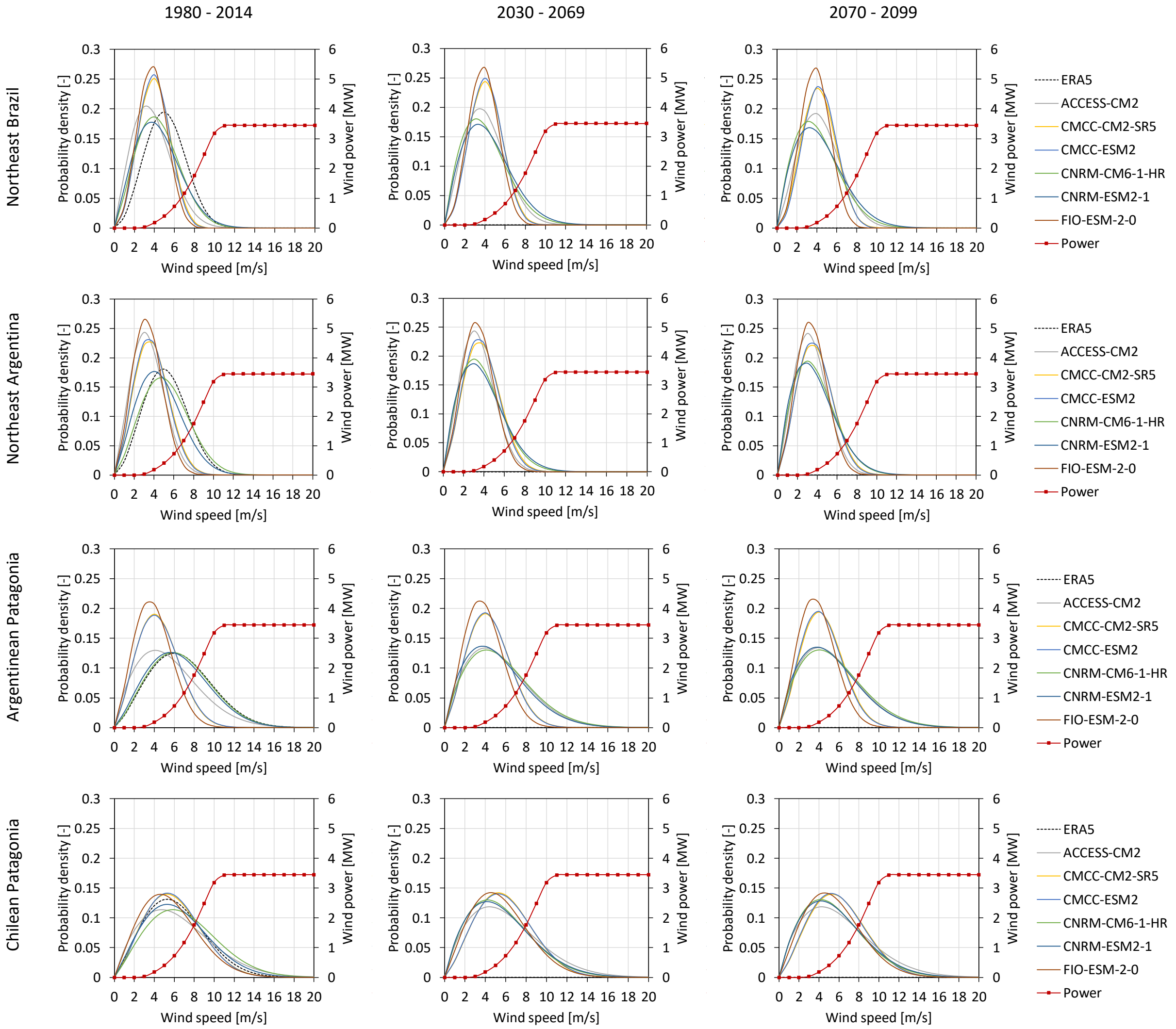

Figure 10. Weibull PDFs of annual wind speed estimated through the method of moments for each region (left panels) during the historical period 1980–2014, (center panels) the period 2030–2069, and (right panels) the period 2070–2099.

In the case of northeastern Argentina, an increase between 0.3 and 9.8% is observed for the period 2030-2069, while for the period 2070-2099 the increase is 1.6 to 8.2%, except for the CNRM-CM6-1-HR and CNRM-ESM2-1 models, which show a decrease in both periods. In the case of Patagonia, both in Argentina and Chile, all models show a decrease in annual wind power generation, although with significant differences. In the case of the Argentinean side, the ACCESS-

CM2, CMCC-CM2-SR5, CMCC-ESM2 and FIO-ESM-2-0 models show more moderate differences with respect to the historical period, ranging between -1.4 and -6.1 % for the period 2030 - 2069 and between -3.3 and -6.7 % for 2070 - 2099. In contrast, the CNRM-CM6-1-HR and CNRM-ESM2-1 models show much larger differences, of -29.3 and -33.6 % for 2030 - 2069 and -29.6 and -31.5 % for 2070 - 2099.

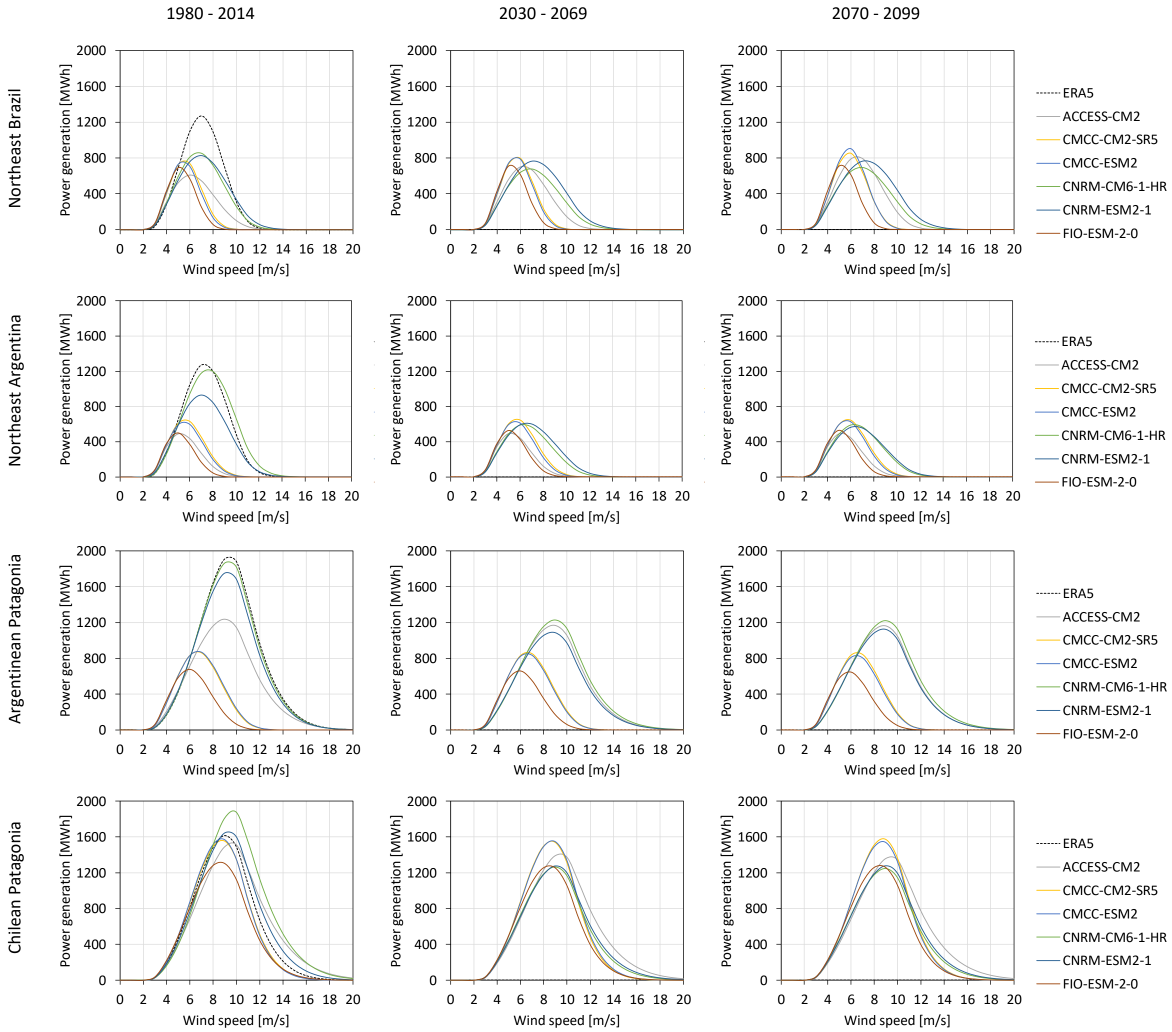

Figure 11. Annual wind power generation curves for each region during (left panels) the historical period 1980-2014, (center panels) the period 2030-2069 and (right panels) the period 2070-2099.

A similar behavior occurs in the case of Chilean Patagonia, on the one hand, the ACCESS-CM2, CMCC-CM2-SR5, CMCC-ESM2 and FIO-ESM-2-0 models show more moderate differences with respect to the historical period, ranging from -0.7 to -8.9 % for the period 2030 - 2069 and between -1.5 and -9.9 % for 2070 - 2099. In contrast, the CNRM-CM6-1-HR and CNRM-ESM2-1 models show much larger differences, of -19.4 and -32.9 % for 2030 – 2069 and of -19.8 and -33.8 % for 2070 – 2099.

Table 3. Future percentage differences in AEP compared to the historical period 1980-2014. Estimated values are shown in bold, and the associated error is shown in the adjacent column (based on ERA5 estimations over the historical period).

	Northeast Brazil				Northeast Argentina				Argentinean Patagonia				Chilean Patagonia			
Model	2030 - 2069 (%)		2070 - 2099 (%)		2030 - 2069 (%)		2070 - 2099 (%)		2030 - 2069 (%)		2070 - 2099 (%)		2030 - 2069 (%)		2070 - 2099 (%)	
ACCESS-CM2	**18.0**	+1.0	**37.6**	+2.0	**0.3**	+0.0	**1.6**	+0.2	**-6.1**	-1.0	**-6.7**	-1.1	**-8.9**	-1.5	**- 9. 9**	-1.6
CMCC-CM2-SR5	**8.6**	+0.5	**19.0**	+1.0	**4.0**	+0.4	**5.1**	+0.6	**-1.4**	-0.2	**-3.3**	-0.6	**-1.7**	-0.3	**0.8**	0.1
CMCC-ESM2	**10.9**	+0.6	**29.5**	+1.6	**2.6**	+0.3	**6.2**	+0.7	**-4.9**	-0.8	**-8.5**	-1.5	**-0.7**	-0.1	**- 1.5**	-0.2
CNRM-CM6-1-HR	**-10.8**	-0.6	**-8.5**	-0.5	**-52.9**	-5.9	**-52.7**	-5.9	**-29.3**	-5.0	**-29.6**	-5.1	**-32.9**	-5.4	**-33.8**	-5.6
CNRM-ESM2-1	**0.8**	+0.0	**3.3**	+0.2	**-31.2**	-3.5	**-36.4**	-4.1	**-33.6**	-5.7	**-31.5**	-5.4	**-19.4**	-3.2	**-19.8**	-3.3
FIO-ESM-2-0	**5.9**	+0.3	**5.4**	+0.3	**9.8**	+1.1	**8.2**	+0.9	**-3.0**	-0.5	**-6.7**	-1.1	**-3.9**	-0.6	**-3 .5**	-0.6
Ensemble	**5.6**	+0.3	**14.4**	+0.8	**-11.2**	-1.3	**-11.3**	-1.3	**-13.0**	-2.2	**-14.4**	-2.5	**-11.2**	-1.9	**-11.3**	-1.9

4. Discussion

4.1. Future changes in WPD and influence of climate modulators

In this research we found that the main changes in WPD over South America for the periods 2030-2069 and 2070-2099 under the SSP2-4.5 scenario, with respect to the historical period 1980-2014, are concentrated in four key regions: northeast Brazil, northeast Argentina near the borders with

Uruguay and Paraguay, a portion of Argentinean Patagonia south of 40°S and finally a small portion of Chilean Patagonia between by 42°S – 46°S. These regions are of great interest for wind power generation since they have mean WS100 values greater than 3 m/s and they also have numerous wind farm locations (De Araujo Lima & Bezerra Filho, 2010; De Jong et al., 2019; Filgueiras & Silva, 2003).

We compared the WS100 behavior of each CMIP6 model with ERA5 over the historical period and found that the models largely represent the WS100 characteristics of each region of interest, such as the annual cycle and the oscillation range of the anomalies. Although the CMIP6 models have improved their performance compared to their predecessor CMIP5, they still have difficulties in correctly representing wind behavior, especially in regions with complex orography (De Souza Ferreira et al., 2024; Llompart et al., 2025). The performance of the models in simulating the behavior of the analyzed atmospheric patterns in the future shows great consistency, representing in a very similar way characteristics such as the annual cycle of the positive and negative phases, as well as the distribution of anomalies for each of the indices.

Over the northeast region of Brazil, a significant increase in WPD is expected, up to 20% for the period 2030-2069 and more than 30% for the period 2070-2099. This is consistent with the results of Karnauskas et al. (2018) who found WPD increases for eastern Brazil of 21% by 2050 and 42% by 2099, as well as de De Jong et al. (2019), who suggest an increase of 40% by 2080 under the SSP5-8.5 scenario. On the other hand, Martinez & Iglesias (2024) found that the largest increase in WPD in South America, up to 100%, will occur over southern Brazil, Uruguay and Paraguay under the SSP2-4.5 scenario, and will extend towards the extreme east of Brazil in the SSP5-8.5 scenario. Also Jung & Schindler (2020, 2022) highlight an increase over southern Brazil. This increase appears to be directly associated with a positive trend in the SAA, which remains the main modulator of WS100 over the region in the future, and therefore its influence is also reflected in WPD. Our results show this relationship is stronger during winter, which makes sense given that the SAA intensity increases in winter. Furthermore, an increase in the correlation is observed from one period to the next in the future, further demonstrating the influence of SAA on WS100 and thus, that the increase in WPD is even greater for the period 2070–2099.

Over northeastern Argentina, an increase in WPD of up to 20% is also expected for 2030–2069, slightly higher for 2070–2099. However, for this specific region, we found no significant correlations with the SAA or with any of the patterns analyzed. In a previous study (Llompart et al., 2025), we conducted a more in-depth analysis of this region, even incorporating other modulators such as ENSO, but no significant relationships emerged either. In contrast, for the Patagonia region, approximately between 40°S - 50°S, on both the Chilean and Argentine sides, WPD decreases of up to -20% are expected for both periods, 2030-2069 and 2070-2099. This is consistent with the results of Martinez & Iglesias (2024), who found decreases of up to -30% west of the Andes for the SSP2-4.5 scenario, mainly in the southernmost areas of the Chilean coast.

Although we did not find specific studies that reveal the reason for the decrease in WPD for the southernmost tip of South America, the results of Watts et al. (2017) reveal that the average wind speed can decrease by around 20% in central and southern Chile associated with patterns such as ENSO, although in a previous study (Llompart et al., 2025) we found that the influence of ENSO on the wind in that region is very weak. However, the PAT does show a significant influence on WS100 in the region, which is inversely proportional as we demonstrated in a previous study (Llompart et al., 2025), and which continues to manifest itself in the future. The PAT also presents a positive trend, which is consistent with the negative trend shown by WPD. This relationship is more evident in winter, although our results reflect a tendency to weaken towards the future, even almost completely disappearing during the summer for the period 2070-2099.

The AAO also influences WS100 in the Patagonian region, albeit to a lesser extent (Llompart et al., 2025), with a negative/positive relationship above/below 45°S, which affects the behavior of the westerly flow over the region. However, our results indicate that this relationship is not as robust, since no significant correlations were found, nor did changes in WPD reflect the aforementioned characteristic dipole of the AAO.

4.2. Future changes in AEP

The aforementioned relationships and changes in WPD toward the future directly influence AEP. According to our results, increasing WPD over northeast Brazil leads to an increase in AEP up to 18% for the period 2030–2069, which doubles to reach up to 37.6% for the period 2070–2099. This largely coincides with the results of De Jong et al. (2019), who found an increase in wind generation of up to 18.2% for the period 2021–2050 and up to 44.8% for the period 2070–2099. In contrast, Esnaola et al. (2024) found that the largest increase in the South American will be in southeastern Brazil, with up to 50% over the entire period 2015-2099.

In the case of northeastern Argentina, we find that most models show an increase up to 9.8% for 2030-2069 and up to 8.2% for 2070-2099, indicating a small decrease between these two periods. The CNRM-CM6-1-HR and CNRM-ESM2-1 models, on the other hand, show a decrease of up to -52.9% for 2030-2069 and up to -52.7% for 2070-2099. In this region, we did not find information from previous studies on a significant increase or decrease. Furthermore, in our case, it is the region with the greatest differences between models, mainly in terms of the sign of the change. Therefore, it is a region in which more dedicated work would have to be done with greater spatial resolution in future research to obtain better insights on the behavior of WPD and AEP in the future.

For the Argentinean side of Patagonia, most models project a decrease of up to -6.1% for the period 2030-2069, and up to -8.5% for the period 2070-2099. The CNRM-CM6-1-HR and CNRM-ESM2-1 models project an even larger decrease, of up to -33.6% for the period 2030-2069 and up to -31.5% for the period 2070-2099. For the Chilean side of Patagonia, most models project a decrease of up to -8.9% for the period 2030-2069 and up to -9.9% for the period 2070-2099. Here too, the CNRM-CM6-1-HR and CNRM-ESM2-1 models show an even larger decrease, of up to -32.9% for 2030-2069 and up to -33.8% for 2070-2099. These results are somewhat consistent with those found by Esnaola et al. (2024), whose study shows a decrease of up to -20% over Patagonia for the period 2015-2099 under the same SSP2-4.5 scenario.

5. Conclusions

In this work, we investigate the future behavior of WS100, WPD, and AEP in South America over the medium-term (2030–2069) and long-term (2070–2099) future. We also explore the influence of four climate modulators on this behavior and their future trend. We use monthly and daily wind speed and SLP data from eight CMIP6 global models over the SSP2-4.5 medium emissions scenario. We also compare monthly, daily, and hourly ERA5 reanalysis data with CMIP6 simulations for the historical period of 1980–2014, which is used as a baseline for calculating future differences. According to our results, the areas with the highest WPD in the future will continue to be northeast and southeast Brazil, with values of up to 300 W/m2 near the coast, Uruguay, and the central-eastern and southeastern parts of Argentina, increasing towards the extreme south of the country over Patagonia with values exceeding 300 W/m2. Chilean Patagonia also shows high WPD values, and towards the north of Chile over the Andes on the border with Argentina, which is best appreciated in winter, with values of up to 300 W/m2.

Over the northeast region of Brazil, a significant increase in WPD is expected, up to 20% for the period 2030-2069 and over 30% for the period 2070-2099. This results in an increase in AEP up to 18% for the period 2030-2069, which doubles to reach up to 37.6% for the period 2070-2099. This increase seems to be directly associated with a positive trend in SAA, which will prevail in the future as the main modulator of WS100 over this region and therefore its influence is also reflected in WPD. Furthermore, an increase in the correlation coefficient R between the SAA index and WS100 in this region is observed, especially in winter: R increases, from 0.5 during the historical period to 0.62 during 2070-2099. This result further demonstrates the influence of SAA on WS100.

In contrast, for Patagonia, spanning approximately between 40°S and 50°S, both on the Chilean and Argentinean sides, WPD decreases up to -20% are expected for both the 2030–2069 and 2070–2099 periods. For the Argentinean side of Patagonia, a decrease in AEP up to -33.6% is projected for the 2030–2069 period, and up to -31.5% for 2070–2099. For the Chilean side of Patagonia, a decrease up to -32.9% is projected for 2030–2069 and up to -33.8 % for 2070–2099. The PAT signal shows a significant influence on WS100 in the region, which is projected to continue in the future. The PAT signal also shows a positive trend, which is consistent with the negative trend shown by the WPD. This relationship is most pronounced in winter, although we found that it tends to weaken toward 2099, dropping from R ~ -0.65 to -0.51 on the Argentine side and from R ~ -0.6 to -0.46 on the Chilean side, and even disappears almost completely during the summer.

In northeastern Argentina, we found significant differences between single models, primarily in the sign of future WPD change and AEP. We also found no clear relationship with any atmospheric pattern influencing WS100 in the area, perhaps largely due to the limitations still present in CMIP6. This is therefore a region that warrants further investigation using higher spatial resolution models. The main contribution of this work is a better understanding of the projected impact of different climate modulators on wind speed variability and wind potential in regions of interest for wind generation in South America. This is essential for wind resource evaluation, long-term system planning and risk assessment in current and future wind projects.

Declaration of interests

The authors declare that they have no conflict of interests.

Funding

This work was supported by the National Agency for Research and Development (ANID) of Chile [grant number 21210309] to OL. MJC acknowledges the support of the Center for Climate and Resilience Research (CR)2, ANID/FONDAP/1523A0002, and Center for Oceanographic Research COPAS Coastal, ANID/FB209921.

Author contributions

Ovidio Llompart: Conceptualization, Methodology, Investigation, Formal Analysis, Visualization, Writing – original draft, Writing – review & editing. **Héctor H. Sepúlveda:** Conceptualization, Methodology, Investigation, Supervision, Writing – review & editing. **Martín**

Jacques-Coper: Conceptualization, Methodology, Investigation, Writing – review & editing. **Marieta Hernández:** Conceptualization, Writing – review & editing. All the authors discussed the results and reviewed the manuscript.

Data availability statement

All datasets used in this study are freely accessible. The ERA5 reanalysis products are available at https://cds.climate.copernicus.eu/cdsapp#!/dataset/reanalysis-era5-single-levels-monthly-means (last access on 1 February 2025). CMIP6 data is available at https://cds.climate.copernicus.eu/cdsapp#!/dataset/projections-cmip6 (last access on 1 February 2025).

References

Ancapichún, S., & Garcés-Vargas, J. (2015). Variability of the Southeast Pacific Subtropical Anticyclone and its impact on sea surface temperature off north-central Chile. *Ciencias Marinas*, *41*(1), 1–20. https://doi.org/10.7773/cm.v41i1.2338

Bao, Y., Song, Z., & Qiao, F. (2020). FIO-ESM Version 2.0: Model Description and Evaluation. *Journal of Geophysical Research: Oceans*, *125*(6), e2019JC016036. https://doi.org/10.1029/2019JC016036

Barbosa De Alencar, D., De Mattos Affonso, C., Limão De Oliveira, R., Moya Rodríguez, J., Leite, J., & Reston Filho, J. (2017). Different Models for Forecasting Wind Power Generation: Case Study. *Energies*, *10*(12), 1976. https://doi.org/10.3390/en10121976

Bi, D., Dix, M., Marsland, S., O'Farrell, S., Sullivan, A., Bodman, R., Law, R., Harman, I., Srbinovsky, J., Rashid, H. A., Dobrohotoff, P., Mackallah, C., Yan, H., Hirst, A., Savita, A., Dias, F. B., Woodhouse, M., Fiedler, R., & Heerdegen, A. (2020). Configuration and spin-up of ACCESS-CM2, the new generation Australian Community Climate and Earth System Simulator Coupled Model. *Journal of Southern Hemisphere Earth Systems Science*, *70*(1), 225–251. https://doi.org/10.1071/ES19040

Bianchi, E., Guozden, T., & Kozulj, R. (2022). Assessing low frequency variations in solar and wind power and their climatic teleconnections. *Renewable Energy*, *190*, 560–571. https://doi.org/10.1016/j.renene.2022.03.080

Cabos, W., Sein, D. V., Pinto, J. G., Fink, A. H., Koldunov, N. V., Alvarez, F., Izquierdo, A., Keenlyside, N., & Jacob, D. (2017). The South Atlantic Anticyclone as a key player for the representation of the tropical Atlantic climate in coupled climate models. *Climate Dynamics*, *48*(11–12), 4051–4069. https://doi.org/10.1007/s00382-016-3319-9

Carvalho, D., Rocha, A., Costoya, X., deCastro, M., & Gómez-Gesteira, M. (2021). Wind energy resource over Europe under CMIP6 future climate projections: What changes from CMIP5 to CMIP6. *Renewable and Sustainable Energy Reviews*, *151*, 111594. https://doi.org/10.1016/j.rser.2021.111594

Chen, L. (2020). Impacts of climate change on wind resources over North America based on NA-CORDEX. *Renewable Energy*, *153*, 1428–1438. https://doi.org/10.1016/j.renene.2020.02.090

Cherchi, A., Fogli, P. G., Lovato, T., Peano, D., Iovino, D., Gualdi, S., Masina, S., Scoccimarro, E., Materia, S., Bellucci, A., & Navarra, A. (2019). Global Mean Climate and Main Patterns of Variability in the CMCC-CM2 Coupled Model. *Journal of Advances in Modeling Earth Systems*, *11*(1), 185–209. https://doi.org/10.1029/2018MS001369

Codron, F. (2005). Relation between Annular Modes and the Mean State: Southern Hemisphere Summer. *Journal of Climate*, *18*(2), 320–330. https://doi.org/10.1175/JCLI-3255.1

Davy, R., Gnatiuk, N., Pettersson, L., & Bobylev, L. (2018). Climate change impacts on wind energy potential in the European domain with a focus on the Black Sea. *Renewable and Sustainable Energy Reviews*, *81*, 1652–1659. https://doi.org/10.1016/j.rser.2017.05.253

De Araujo Lima, L., & Bezerra Filho, C. R. (2010). Wind energy assessment and wind farm simulation in Triunfo – Pernambuco, Brazil. *Renewable Energy*, *35*(12), 2705–2713. https://doi.org/10.1016/j.renene.2010.04.019

De Jong, P., Barreto, T. B., Tanajura, C. A. S., Kouloukoui, D., Oliveira-Esquerre, K. P., Kiperstok, A., & Torres, E. A. (2019). Estimating the impact of climate change on wind and solar energy in Brazil using a South American regional climate model. *Renewable Energy*, *141*, 390–401. https://doi.org/10.1016/j.renene.2019.03.086

De Souza Ferreira, G. W., Reboita, M. S., Ribeiro, J. G. M., Carvalho, V. S. B., Santiago, M. E. V., Silva, P. L. L. S., Baldoni, T. C., & De Souza, C. A. (2024). Assessment of the wind power density over South America simulated by CMIP6 models in the present and future climate. *Climate Dynamics*, *62*(3), 1729–1763. https://doi.org/10.1007/s00382-023-06993-3

Deng, K., Azorin-Molina, C., Yang, S., Hu, C., Zhang, G., Minola, L., & Chen, D. (2022). Changes of Southern Hemisphere westerlies in the future warming climate. *Atmospheric Research*, *270*, 106040. https://doi.org/10.1016/j.atmosres.2022.106040

Devis, A., Van Lipzig, N. P. M., & Demuzere, M. (2018). Should future wind speed changes be taken into account in wind farm development? *Environmental Research Letters*, *13*(6), 064012. https://doi.org/10.1088/1748-9326/aabff7

Doddy Clarke, E., Sweeney, C., McDermott, F., Griffin, S., Correia, J. M., Nolan, P., & Cooke, L. (2022). Climate change impacts on wind energy generation in Ireland. *Wind Energy*, *25*(2), 300–312. https://doi.org/10.1002/we.2673

Emodi, N. V., Chaiechi, T., & Beg, A. B. M. R. A. (2019). The impact of climate variability and change on the energy system: A systematic scoping review. *Science of The Total Environment*, *676*, 545–563. https://doi.org/10.1016/j.scitotenv.2019.04.294

Esnaola, G., Ulazia, A., Sáenz, J., & Ibarra-Berastegi, G. (2024). Future changes of global Annual and Seasonal Wind-Energy Production in CMIP6 projections considering air density variation. *Energy*, *307*, 132706. https://doi.org/10.1016/j.energy.2024.132706

Feng, S., Wang, W., Wang, Z., Song, Z., Yang, Q., & Wang, B. (2024). Global Wind-Power Generation Capacity in the Context of Climate Change. *Engineering*, S2095809924005873. https://doi.org/10.1016/j.eng.2024.09.018

Filgueiras, A., & Silva, T. M. V. e. (2003). Wind energy in Brazil—Present and future. *Renewable and Sustainable Energy Reviews*, *7*(5), 439–451. https://doi.org/10.1016/S1364-0321(03)00068-6

Foley, A. M., Leahy, P. G., Marvuglia, A., & McKeogh, E. J. (2012). Current methods and advances in forecasting of wind power generation. *Renewable Energy*, *37*(1), 1–8. https://doi.org/10.1016/j.renene.2011.05.033

Ganea, D., Mereuta, E., & Rusu, L. (2018). Estimation of the Near Future Wind Power Potential in the Black Sea. *Energies*, *11*(11), 3198. https://doi.org/10.3390/en11113198

Gao, Y., Ma, S., & Wang, T. (2019). The impact of climate change on wind power abundance and variability in China. *Energy*, *189*, 116215. https://doi.org/10.1016/j.energy.2019.116215

Garreaud, R. D., Vuille, M., Compagnucci, R., & Marengo, J. (2009). Present-day South American climate. *Palaeogeography, Palaeoclimatology, Palaeoecology*, *281*(3–4), 180–195. https://doi.org/10.1016/j.palaeo.2007.10.032

Greene, C. A., Thirumalai, K., Kearney, K. A., Delgado, J. M., Schwanghart, W., Wolfenbarger, N. S., Thyng, K. M., Gwyther, D. E., Gardner, A. S., & Blankenship, D. D. (2019). The Climate Data Toolbox for

MATLAB. *Geochemistry, Geophysics, Geosystems*, *20*(7), 3774–3781. https://doi.org/10.1029/2019GC008392

Gugliani, G. K., Sarkar, A., Ley, C., & Matsagar, V. (2021). Identification of optimum wind turbine parameters for varying wind climates using a novel month-based turbine performance index. *Renewable Energy*, *171*, 902–914. https://doi.org/10.1016/j.renene.2021.02.141

He, B., Yu, Y., Bao, Q., Lin, P., Liu, H., Li, J., Wang, L., Liu, Y., Wu, G., Chen, K., Guo, Y., Zhao, S., Zhang, X., Song, M., & Xie, J. (2020). CAS FGOALS-f3-L model dataset descriptions for CMIP6 DECK experiments. *Atmospheric and Oceanic Science Letters*, *13*(6), 582–588. https://doi.org/10.1080/16742834.2020.1778419

Islek, F., Yuksel, Y., & Sahin, C. (2020). Spatiotemporal long-term trends of extreme wind characteristics over the Black Sea. *Dynamics of Atmospheres and Oceans*, *90*, 101132. https://doi.org/10.1016/j.dynatmoce.2020.101132

Jung, C., & Schindler, D. (2020). Introducing a new approach for wind energy potential assessment under climate change at the wind turbine scale. *Energy Conversion and Management*, *225*, 113425. https://doi.org/10.1016/j.enconman.2020.113425

Jung, C., & Schindler, D. (2022). A review of recent studies on wind resource projections under climate change. *Renewable and Sustainable Energy Reviews*, *165*, 112596. https://doi.org/10.1016/j.rser.2022.112596

Karnauskas, K. B., Lundquist, J. K., & Zhang, L. (2018). Southward shift of the global wind energy resource under high carbon dioxide emissions. *Nature Geoscience*, *11*(1), 38–43. https://doi.org/10.1038/s41561-017-0029-9

Kim, D.-Y., Kim, Y.-H., & Kim, B.-S. (2021). Changes in wind turbine power characteristics and annual energy production due to atmospheric stability, turbulence intensity, and wind shear. *Energy*, *214*, 119051. https://doi.org/10.1016/j.energy.2020.119051

Li, X., Li, Q.-P., Ding, Y.-H., & Wang, M. (2022). Near-surface wind speed changes in eastern China during 1970–2019 winter and its possible causes. *Advances in Climate Change Research*, *13*(2), 228–239. https://doi.org/10.1016/j.accre.2022.01.003

Llompart, O., Sepúlveda, H. H., Jacques-Coper, M., & Hernández, M. (2025). Evaluating Wind Speed Variability and Its Climate Modulators in South America Using CMIP6 Simulations (1980–2014). *International Journal of Climatology*, e8921. https://doi.org/10.1002/joc.8921

Lovato, T., Peano, D., Butenschön, M., Materia, S., Iovino, D., Scoccimarro, E., Fogli, P. G., Cherchi, A., Bellucci, A., Gualdi, S., Masina, S., & Navarra, A. (2022). CMIP6 Simulations With the CMCC Earth System Model

(CMCC-ESM2). *Journal of Advances in Modeling Earth Systems*, *14*(3), e2021MS002814. https://doi.org/10.1029/2021MS002814

Lübbecke, J. F., Burls, N. J., Reason, C. J. C., & McPhaden, M. J. (2014). Variability in the South Atlantic Anticyclone and the Atlantic Niño Mode*. *Journal of Climate*, *27*(21), 8135–8150. https://doi.org/10.1175/JCLI-D-14-00202.1

Manwell, J. F. (n.d.). *Wind Energy Explained: Theory, Design and Application*.

Marshall, G. J. (2003). Trends in the Southern Annular Mode from Observations and Reanalyses. *Journal of Climate*, *16*(24), 4134–4143. https://doi.org/10.1175/1520-0442(2003)016<4134:TITSAM>2.0.CO;2

Martinez, A., & Iglesias, G. (2021). Wind resource evolution in Europe under different scenarios of climate change characterised by the novel Shared Socioeconomic Pathways. *Energy Conversion and Management*, *234*, 113961. https://doi.org/10.1016/j.enconman.2021.113961

Martinez, A., & Iglesias, G. (2024). Climate change and wind energy potential in South America. *Science of The Total Environment*, *957*, 177675. https://doi.org/10.1016/j.scitotenv.2024.177675

Miyasaka, T., & Nakamura, H. (2010). Structure and Mechanisms of the Southern Hemisphere Summertime Subtropical Anticyclones. *Journal of Climate*, *23*(8), 2115–2130. https://doi.org/10.1175/2009JCLI3008.1

Moemken, J., Reyers, M., Feldmann, H., & Pinto, J. G. (2018). Future Changes of Wind Speed and Wind Energy Potentials in EURO-CORDEX Ensemble Simulations. *Journal of Geophysical Research: Atmospheres*, *123*(12), 6373–6389. https://doi.org/10.1029/2018JD028473

Peiris, A. T., Jayasinghe, J., & Rathnayake, U. (2021). Forecasting Wind Power Generation Using Artificial Neural Network: “Pawan Danawi”—A Case Study from Sri Lanka. *Journal of Electrical and Computer Engineering*, *2021*, 1–10. https://doi.org/10.1155/2021/5577547

Qian, H., & Zhang, R. (2021). Future changes in wind energy resource over the Northwest Passage based on the CMIP6 climate projections. *International Journal of Energy Research*, *45*(1), 920–937. https://doi.org/10.1002/er.5997

Rodwell, M. J., & Hoskins, B. J. (2001). Subtropical Anticyclones and Summer Monsoons. *Journal of Climate*, *14*(15), 3192–3211. https://doi.org/10.1175/1520-0442(2001)014<3192:SAASM>2.0.CO;2

Russo, M. A., Carvalho, D., Martins, N., & Monteiro, A. (2023). Future perspectives for wind and solar electricity production under high-resolution climate change scenarios. *Journal of Cleaner Production*, *404*, 136997. https://doi.org/10.1016/j.jclepro.2023.136997

Sawadogo, W., Reboita, M. S., Faye, A., Da Rocha, R. P., Odoulami, R. C., Olusegun, C. F., Adeniyi, M. O., Abiodun, B. J., Sylla, M. B., Diallo, I., Coppola, E., & Giorgi, F. (2021). Current and future potential of solar and wind energy over Africa using the RegCM4 CORDEX-CORE ensemble. *Climate Dynamics*, *57*(5–6), 1647–1672. https://doi.org/10.1007/s00382-020-05377-1

Séférian, R., Nabat, P., Michou, M., Saint-Martin, D., Voldoire, A., Colin, J., Decharme, B., Delire, C., Berthet, S., Chevallier, M., Sénési, S., Franchisteguy, L., Vial, J., Mallet, M., Joetzjer, E., Geoffroy, O., Guérémy, J., Moine, M., Msadek, R., … Madec, G. (2019). Evaluation of CNRM Earth System Model, CNRM-ESM2-1: Role of Earth System Processes in Present-Day and Future Climate. *Journal of Advances in Modeling Earth Systems*, *11*(12), 4182–4227. https://doi.org/10.1029/2019MS001791

Shadman, M., Roldan-Carvajal, M., Pierart, F. G., Haim, P. A., Alonso, R., Silva, C., Osorio, A. F., Almonacid, N., Carreras, G., Maali Amiri, M., Arango-Aramburo, S., Rosas, M. A., Pelissero, M., Tula, R., Estefen, S. F., Pastor, M. L., & Saavedra, O. R. (2023). A Review of Offshore Renewable Energy in South America: Current Status and Future Perspectives. *Sustainability*, *15*(2), 1740. https://doi.org/10.3390/su15021740

Shin, J.-Y., Jeong, C., & Heo, J.-H. (2018). A Novel Statistical Method to Temporally Downscale Wind Speed Weibull Distribution Using Scaling Property. *Energies*, *11*(3), 633. https://doi.org/10.3390/en11030633

Solaun, K., & Cerdá, E. (2020). Impacts of climate change on wind energy power – Four wind farms in Spain. *Renewable Energy*, *145*, 1306–1316. https://doi.org/10.1016/j.renene.2019.06.129

Swart, N. C., Cole, J. N. S., Kharin, V. V., Lazare, M., Scinocca, J. F., Gillett, N. P., Anstey, J., Arora, V., Christian, J. R., Hanna, S., Jiao, Y., Lee, W. G., Majaess, F., Saenko, O. A., Seiler, C., Seinen, C., Shao, A., Sigmond, M., Solheim, L., … Winter, B. (2019). The Canadian Earth System Model version 5 (CanESM5.0.3). *Geoscientific Model Development*, *12*(11), 4823–4873. https://doi.org/10.5194/gmd-12-4823-2019

Thompson, D. W. J., & Wallace, J. M. (2000). Annular Modes in the Extratropical Circulation. Part I: Month-to-Month Variability*. *Journal of Climate*, *13*(5), 1000–1016. https://doi.org/10.1175/1520-0442(2000)013<1000:AMITEC>2.0.CO;2

Tian, Q., Huang, G., Hu, K., & Niyogi, D. (2019). Observed and global climate model based changes in wind power potential over the Northern Hemisphere during 1979–2016. *Energy*, *167*, 1224–1235. https://doi.org/10.1016/j.energy.2018.11.027

Tobin, I., Jerez, S., Vautard, R., Thais, F., Van Meijgaard, E., Prein, A., Déqué, M., Kotlarski, S., Maule, C. F., Nikulin, G., Noël, T., & Teichmann, C. (2016). Climate change impacts on the power generation potential of a European mid-century wind farms scenario. *Environmental Research Letters*, *11*(3), 034013. https://doi.org/10.1088/1748-9326/11/3/034013

Tobin, I., Vautard, R., Balog, I., Bréon, F.-M., Jerez, S., Ruti, P. M., Thais, F., Vrac, M., & Yiou, P. (2015). Assessing climate change impacts on European wind energy from ENSEMBLES high-resolution climate projections. *Climatic Change*, *128*(1–2), 99–112. https://doi.org/10.1007/s10584-014-1291-0

Voldoire, A., Saint-Martin, D., Sénési, S., Decharme, B., Alias, A., Chevallier, M., Colin, J., Guérémy, J. -F., Michou, M., Moine, M. -P., Nabat, P., Roehrig, R., Salas Y Mélia, D., Séférian, R., Valcke, S., Beau, I., Belamari, S., Berthet, S., Cassou, C., … Waldman, R. (2019). Evaluation of CMIP6 DECK Experiments With CNRM-CM6-1. *Journal of Advances in Modeling Earth Systems*, *11*(7), 2177–2213. https://doi.org/10.1029/2019MS001683

Watts, D., Durán, P., & Flores, Y. (2017). How does El Niño Southern Oscillation impact the wind resource in Chile? A techno-economical assessment of the influence of El Niño and La Niña on the wind power. *Renewable Energy*, *103*, 128–142. https://doi.org/10.1016/j.renene.2016.10.031

Weber, J., Gotzens, F., & Witthaut, D. (2018). Impact of strong climate change on the statistics of wind power generation in Europe. *Energy Procedia*, *153*, 22–28. https://doi.org/10.1016/j.egypro.2018.10.004

Wilkie, D., & Galasso, C. (2020). Impact of climate-change scenarios on offshore wind turbine structural performance. *Renewable and Sustainable Energy Reviews*, *134*, 110323. https://doi.org/10.1016/j.rser.2020.110323

Wu, J., Shi, Y., & Xu, Y. (2020). Evaluation and Projection of Surface Wind Speed Over China Based on CMIP6 GCMs. *Journal of Geophysical Research: Atmospheres*, *125*(22), e2020JD033611. https://doi.org/10.1029/2020JD033611

Zhang, D., Xu, Z., Li, C., Yang, R., Shahidehpour, M., Wu, Q., & Yan, M. (2019). Economic and sustainability promises of wind energy considering the impacts of climate change and vulnerabilities to extreme conditions. *The Electricity Journal*, *32*(6), 7–12. https://doi.org/10.1016/j.tej.2019.05.013

V. DISCUSIÓN GENERAL

En este estudio, analizamos la influencia de los moduladores climáticos SPA, SAA, ENSO, AAO en el comportamiento del recurso eólico en América del Sur mediante simulaciones de velocidad del viento, SLP y SST de 14 modelos de CMIP6. Investigamos el comportamiento futuro de WS100, WPD y AEP a mediano plazo (2030-2069) y largo plazo (2070-2099) bajo el escenario medio de emisiones SSP2-4.5. Además, utilizamos datos mensuales, diarios y horarios de reanálisis del ERA5 como referencia para comparar con los resultados de los modelos de CMIP6 durante el período histórico de 1980-2014, utilizado como base para calcular las diferencias futuras.

Los modelos CMIP6 en su mayoría reflejaron de forma razonable características de los patrones atmosféricos analizados, como la amplitud de las oscilaciones, el período de retorno y la huella espacial sobre los campos de SST y SLP. Los modelos ACCESS-CM2 y CanESM5-CanOE destacan por su capacidad para capturar la señal de los patrones analizados y su influencia en WS100. No obstante, el rendimiento general de los modelos CMIP6 para representar el forzamiento local y regional continúa siendo limitado, especialmente en regiones con orografía compleja (De Souza Ferreira et al., 2024; Wu et al., 2020).

A pesar de estas limitantes, los resultados encontrados en la presente investigación permiten establecer de manera consistente, a escala regional, la relación entre WS100 y sus principales moduladores climáticos a gran escala, así como los impactos sobre WPD y AEP en el futuro. Adicionalmente descubrimos otro modulador de WS100, el cual nombramos Patrón Patagonia-Antártica (PAT). Este hallazgo reviste gran relevancia para la planificación y explotación del recurso eólico en América del Sur, ya que posibilita la identificación de las zonas con mayor o menor potencial eólico en función de las variaciones proyectadas de dichos patrones.

V.1. Influencia de los moduladores climáticos sobre WS100 durante el período histórico

El análisis EOF aplicado, en combinación con el método de correlación de Pearson, constituye una herramienta robusta para detectar la influencia de los moduladores climáticos sobre el campo de

WS100, en las tres subregiones analizadas: REG1 (nordeste de Brasil), REG2 (norte de Chile y Argentina), y REG3 (Patagonia). Los EOF se destacan por aislar las señales coherentes con diferentes patrones atmosféricos sobre el recurso eólico en este caso, permitiendo identificar las regiones donde WS100 se incrementa o disminuye según la fase de cada patrón. Es una técnica que logra reducir la dimensionalidad de campos atmosféricos complejos, resumiendo la información en unos pocos modos representativos o componentes principales (PC), lo que facilita la interpretación física de la relación entre el viento y sus moduladores climáticos (Farjami & Hesari, 2020; Sinha et al., 2020; Wang et al., 2024; Watts et al., 2017; Zhou et al., 2022).

Nuestros resultados revelan que el SAA es el principal modulador de WS100 en el nordeste de Brasil (REG1), dado por una relación positiva, con coeficientes de correlación de hasta 0,55 en la serie mensual (0,54 en invierno y 0,46 en verano), entre la intensidad del SAA y la PC1 para REG1, que explica el 59,1% de la varianza total en dicha región. Esta correlación, más fuerte en invierno que en verano, también coincide con la intensificación del SAA durante el invierno (Cabos et al., 2017), lo cual demuestra su influencia sobre WS100 en esta región.

En la Patagonia (REG3), encontramos que el comportamiento de WS100 está dominado principalmente por un patrón de anomalías del SLP, al que denominamos Patrón Patagonia-Antártica (PAT), centrado alrededor del Pasaje de Drake y que afecta el flujo de los vientos del oeste en la región. Al sur de los 40° S, el flujo del oeste prevalece en niveles bajos durante todo el año (Garreaud et al., 2009), por lo que la variabilidad del viento en la Patagonia responde fundamentalmente a las variaciones en el viento del oeste. Encontramos correlaciones negativas significativas, de hasta -0,83 en verano y -0,75 en invierno (-0,81 en la serie mensual), entre PAT y PC1 para la REG3, que explica el 52,2% de la varianza total en la región. Esto significa que la fase positiva del índice PAT provoca una disminución de WS100 sobre la Patagonia y un incremento durante la fase negativa.

La AAO es responsable en segundo lugar de la variabilidad de WS100 sobre la Patagonia, principalmente en verano, lo cual está determinado por coeficientes de correlación positivos de hasta 0,52 (0,42 en invierno y 0,46 en la serie mensual), entre el índice AAO y la PC2 para la REG3, que explica el 22,8% de la varianza total. La fase positiva de la AAO provoca un aumento de WS100 en el extremo sur de la Patagonia y una disminución al norte de los 45° S, lo cual coincide con los resultados de Bianchi et al. (2017, 2022).

Además, para la zona chilena de la Patagonia se encontró cierta influencia de la SPA, que se manifiesta con mayor claridad en invierno, con coeficientes de correlación de hasta 0,49 (0,4 en verano). El SPA influye en los mecanismos que causan variaciones en el gradiente de presión y la intensidad de los vientos del oeste sobre la región de la Patagonia, y también presenta una correlación negativa con el ENSO (Gómez-Fontealba et al., 2022). Esta relación debería explorarse con mayor detalle en el futuro, puesto que no encontramos relaciones significativas entre el ENSO y el comportamiento de WS100 en ninguna de las regiones analizadas.

En el caso del norte de Chile y Argentina (REG2), solo se encontró un coeficiente de correlación débil de 0,3 para el ERA5 entre la intensidad de la SPA y la WS100 en los casos extremos de WS100, principalmente durante la primavera. Un futuro análisis con mayor resolución espacial sobre esta región permitiría comprender mejor el comportamiento del recurso eólico y sus moduladores climáticos, dadas las limitantes mencionadas anteriormente de los modelos de CMIP6 para capturar las características del viento en regiones con orografía compleja.

V.2. Variaciones futuras de WPD y AEP e influencia de los moduladores climáticos

Según nuestros resultados, las áreas con mayor WPD en el futuro permanecen sobre el nordeste y sureste de Brasil, con valores de hasta 300 W/m² cerca de la costa, Uruguay, el centro-este y sureste de Argentina, aumentando hacia el extremo sur del país sobre la Patagonia con valores superiores a 300 W/m². La Patagonia chilena también muestra altos valores de WPD, y hacia el norte de Chile, sobre los Andes en la frontera con Argentina, los cuales se aprecian mejor en invierno, con valores de hasta 300 W/m². Encontramos que los principales cambios en WPD y AEP se concentran en dos regiones fundamentales: el nordeste de Brasil y la Patagonia.

En la región nordeste de Brasil, se espera un aumento significativo de WPD, de hasta un 20 % para el período 2030-2069 y superior al 30 % para el período 2070-2099, lo que coincide en gran medida con los resultados de De Jong et al. (2019) y Karnauskas et al. (2018). Esto resulta en un aumento de AEP de hasta un 18 % para el período 2030-2069, que se duplica hasta alcanzar el 37,6 % para el período 2070-2099, coincidiendo con De Jong et al. (2019). Este aumento parece estar directamente asociado con una tendencia positiva en el SAA, que prevalecerá en el futuro como el principal modulador de WS100 en esa región y, por lo tanto, su influencia también se refleja en WPD. Además, se observa un aumento en el coeficiente de correlación, especialmente en invierno, de 0,5 durante el período histórico a 0,62 durante 2070-2099, lo que demuestra aún más la influencia del SAA en WS100, puesto que su intensidad aumenta en invierno (Cabos et al., 2017).

En contraste, para la región de la Patagonia, aproximadamente entre 40°S y 50°S, tanto en el lado chileno como en el argentino, se esperan disminuciones de WPD de hasta un -20% para los períodos 2030-2069 y 2070-2099. Para el lado argentino de la Patagonia, se proyecta una disminución de AEP de hasta un -33,6% para el período 2030-2069 y de hasta un -31,5% para el período 2070-2099. Mientras que, para el lado chileno de la Patagonia, se proyecta una disminución de hasta -32,9 % para el período 2030-2069 y de hasta -33,8 % para el período 2070-2099. Estos resultados son consistentes en cierta medida con los encontrados por Esnaola et al. (2024).

El PAT muestra una influencia significativa sobre WS100 en la región de la Patagonia, la cual es inversamente proporcional y continúa manifestándose en el futuro. WPD muestra una tendencia negativa, consistente con la tendencia positiva mostrada por el PAT. Esta relación es más pronunciada en invierno, aunque nuestros resultados muestran que tiende a debilitarse desde 1980 hasta 2099, pasando de un coeficiente de correlación -0,65 a -0,51 en el lado argentino y de -0,6 a -0,46 en el lado chileno, e incluso desaparece casi por completo durante el verano.

En el noreste de Argentina, encontramos diferencias significativas entre los modelos, principalmente en el signo del cambio en el futuro de WPD y AEP. Tampoco encontramos una relación clara con ningún patrón atmosférico que influya en WS100 en esta región, posiblemente debido en gran medida a las limitaciones aún presentes en los modelos CMIP6, como mencionan varios autores (De Souza Ferreira et al., 2024; Wu et al., 2020). Por lo tanto, esta es una región que justifica una mayor investigación utilizando modelos con mayor resolución espacial. También tenemos en cuenta que es importante centrarse por separado en regiones de interés más pequeñas, dada la diversa orografía de América del Sur, y trabajar con datos de mayor resolución temporal para obtener resultados más precisos.

Los resultados obtenidos permiten aprobar parcialmente la hipótesis de investigación, dado que se comprobó que la variabilidad del viento en América del Sur está efectivamente modulada por patrones climáticos de gran escala, principalmente el SAA y el PAT, este último encontrado a raíz del presente estudio. Estos moduladores ejercen un impacto significativo sobre el potencial eólico en regiones clave del continente, como el nordeste de Brasil (+30%) y la Patagonia (-20%) hacia finales de siglo. Sin embargo, la influencia de otros moduladores como el SPA, la AAO y el ENSO fue débil o inconsistente en algunas regiones, lo que limita la confirmación total de la hipótesis para toda América del Sur.

Las implicancias de estos resultados son relevantes para el desarrollo estratégico de la energía eólica en la región. El fortalecimiento del SAA sugiere que el nordeste de Brasil consolidará su rol como una de las zonas con mayor WPD del continente, con un aumento en AEP de hasta +37,6%, favoreciendo la expansión de parques eólicos y la planificación de infraestructura energética en esa región. En contraste, la tendencia negativa de WPD en la Patagonia, con disminuciones de AEP cercanas a -33%, vinculada a la influencia del PAT, indica que será necesario ajustar las estrategias de inversión y operación en esa zona, sobre todo durante los meses de verano. En conjunto, este estudio demuestra que el impacto y evolución de los moduladores climáticos debe considerarse como un factor clave en la planificación a largo plazo del sector eólico sudamericano, especialmente bajo los efectos del cambio climático.

VI. CONCLUSIONES GENERALES

Los resultados obtenidos en esta investigación muestran que el Anticiclón del Atlántico Sur (SAA) es el principal modulador de WS100 sobre el nordeste de Brasil, dado por una correlación positiva. Esto significa que un aumento en la intensidad del SAA, provoca un aumento de WS100, mientras que este disminuye con un debilitamiento del SAA. Esta relación tiende a hacerse más fuerte hacia el futuro, especialmente en invierno durante el período 2070 – 2099. Descubrimos además un patrón de anomalías de SLP con centro en el Pasaje de Drake, al que denominamos patrón Patagonia - Antártica (PAT), y que constituye el principal modulador de WS100 sobre la Patagonia, dado por una correlación negativa. Esto significa que la fase positiva del PAT provoca una disminución de WS100 sobre la Patagonia y un aumento durante su fase negativa. Esta relación tiende a debilitarse hacia el futuro, particularmente en verano durante el período 2070 – 2099.

Los principales cambios en la densidad del potencial eólico (WPD) y la producción anual de energía eólica (AEP) en el futuro se concentran en dos regiones fundamentales: el nordeste de Brasil y la Patagonia. Se prevé un aumento significativo de WPD de más del 30% para 2099 en el nordeste de Brasil, asociado principalmente a una tendencia positiva del SAA. Por otra parte, se proyecta una disminución de WPD de hasta un -20% en la Patagonia asociada a una tendencia positiva en el PAT y su relación negativa con WS100 sobre esta región. Estos cambios equivalen a un aumento de AEP de hasta un 18% para 2069 y un 37,6% para 2099 en el nordeste de Brasil, mientras que en la Patagonia se proyecta una disminución de hasta un -33,6% para 2069 y un -33,8% para 2099.

Es importante tener en cuenta, para futuras investigaciones, la necesidad de definir regiones de interés más pequeñas, dada la diversa orografía de América del Sur. Además, es necesario incorporar modelos regionales con mayor resolución espacial que permitan obtener resultados más precisos. La principal contribución de este trabajo es que brinda un mayor conocimiento sobre el impacto de diferentes patrones atmosféricos en la variabilidad de la velocidad del viento y el potencial eólico terrestre en regiones de interés para la generación eólica en América del Sur. Esto es esencial para la evaluación del recurso eólico, la planificación del sistema a largo plazo y la evaluación de riesgos en proyectos eólicos. Este trabajo además puede ser replicado en otras regiones del mundo para contribuir al manejo eficiente del recurso eólico terrestre en el futuro.

VI.1 Continuidad de la investigación

La región de América del Sur con más de 25.000 km de costa tiene un gran potencial eólico marino (off-shore), especialmente a lo largo de las costas de Brasil, Colombia y el sur de Chile (Shadman et al., 2023). La zona centro sur de Chile en particular tiene un alto potencial para implementar la energía eólica off-shore, con valores que oscilan entre 745 y 1240 W/m2 sobre el mar (Mattar &

Borvarán, 2016). Según Mattar & Guzmán-Ibarra (2017) el área entre 30 y 32°S es la más adecuada para implementar un proyecto eólico off-shore debido a su densidad de potencial eólico (entre 700 W/m2 y 900 W/m2), factores de capacidad entre 40% y 60% y costo nivelado de energía entre 100 y 114 USD$/MWh.

Los resultados de Mattar et al. (2021) muestran que hasta el 80% de la costa chilena presenta resultados favorables para la explotación del recurso eólico, basándose en estimaciones del costo nivelado de energía de 2000 a 2054 utilizando las proyecciones climáticas RCP4.5 y RCP8.5. Sin embargo, hasta el momento, estos recursos no han sido explotados comercialmente en Chile, ni en el resto de América del Sur (Shadman et al., 2023). Aunque en el caso de las costas de Chile ya se encuentran en fase de concesión marítima tres proyectos a cargo de las empresas de inversión extranjera Deep Wind Offshore (*https://www.deepwindoffshore.com*) y Viento Azul Biobío (*https://www.vientoazulbiobio.cl*), que comenzarían a operar en la década de 2030 en las costas de la Región del Biobío.

Es por ello por lo que, como continuación del presente estudio pretendemos extender la investigación sobre el futuro del potencial eólico off-shore en América del Sur, con énfasis sobre las costas de Chile. Para ello utilizaremos modelos regionales con mayor resolución espacial, que permitirán obtener resultados más detallados, teniendo en cuenta la complejidad de la línea de costa. Estos resultados contribuirán a la eficiencia en la futura explotación del recurso eólico en los proyectos mencionados anteriormente y a incentivar el desarrollo de nuevos proyectos de este tipo en la región de América del Sur, en aras de alcanzar el objetivo de cero emisiones netas propuesto por el IPCC en el marco de las Naciones Unidas.

REFERENCIAS GENERALES

Akinsanola, A. A., Ogunjobi, K. O., Abolude, A. T., & Salack, S. (2021). Projected changes in wind speed and wind energy potential over West Africa in CMIP6 models. Environmental Research Letters, 16(4). https://doi.org/10.1088/1748-9326/abed7a

Alonzo, B., Ringkjob, H.-K., Jourdier, B., Drobinski, P., Plougonven, R., & Tankov, P. (2017). Modelling the variability of the wind energy resource on monthly and seasonal timescales. Renewable Energy, 113, 1434–1446. https://doi.org/10.1016/j.renene.2017.07.019

An, S. I., & Jin, F. F. (2004). Nonlinearity and Asymmetry of ENSO. Journal of Climate, 17 (12), 2399–2412. https://doi.org/10.1175/1520-0442(2004)017<2399:NAAOE>2.0.CO;2

Ancapichún, S., & Garcés-Vargas, J. (2015). Variability of the Southeast Pacific Subtropical Anticyclone and its impact on sea surface temperature off north-central Chile. Ciencias Marinas, 41(1), 1–20. https://doi.org/10.7773/cm.v41i1.2338

Andrews, M. B., Ridley, J. K., Wood, R. A., Andrews, T., Blockley, E. W., Booth, B., Burke, E., Dittus, A. J., Florek, P., Gray, L. J., Haddad, S., Hardiman, S. C., Hermanson, L., Hodson, D., Hogan, E., Jones, G. S., Knight, J. R., Kuhlbrodt, T., Misios, S., … Sutton, R. T. (2020). Historical Simulations With HadGEM3-GC3.1 for CMIP6. Journal of Advances in Modeling Earth Systems, 12(6). https://doi.org/10.1029/2019ms001995

Aramburo, D., Montoya, R. D., & Osorio, A. F. (2022). Impact of the ENSO phenomenon on wave variability in the Pacific Ocean for wind sea and swell waves. Dynamics of Atmospheres and Oceans, 100. https://doi.org/10.1016/j.dynatmoce.2022.101328

Bao, Y., Song, Z., & Qiao, F. (2020). FIO-ESM Version 2.0: Model Description and Evaluation. Journal of Geophysical Research: Oceans, 125(6), e2019JC016036. https://doi.org/10.1029/2019JC016036

Barbosa De Alencar, D., De Mattos Affonso, C., Limão De Oliveira, R., Moya Rodríguez, J., Leite, J., & Reston Filho, J. (2017). Different Models for Forecasting Wind Power Generation: Case Study. Energies, 10(12), 1976. https://doi.org/10.3390/en10121976

Bi, D., Dix, M., Marsland, S., O'Farrell, S., Sullivan, A., Bodman, R., Law, R., Harman, I., Srbinovsky, J., Rashid, H. A., Dobrohotoff, P., Mackallah, C., Yan, H., Hirst, A., Savita, A., Dias, F. B., Woodhouse, M., Fiedler, R., & Heerdegen, A. (2020). Configuration and spin-up of ACCESS-CM2, the new generation Australian Community Climate and Earth System Simulator Coupled Model. Journal of Southern Hemisphere Earth Systems Science, 70(1), 225–251. https://doi.org/10.1071/ES19040

Bianchi, E., Guozden, T., & Kozulj, R. (2022). Assessing low frequency variations in solar and wind power and their climatic teleconnections. Renewable Energy, 190, 560–571. https://doi.org/10.1016/j.renene.2022.03.080

Bianchi, E., Solarte, A., & Guozden, T. M. (2017). Large scale climate drivers for wind resource in Southern South America. Renewable Energy, 114, 708–715. https://doi.org/10.1016/j.renene.2017.07.075

Bjerknes, J. (1969). Atmospheric teleconnections from the equatorial pacific. Monthly Weather Review, 97 (3), 163–172. https://doi.org/10.1175/1520-0493(1969)097<0163:ATFTEP>2.3.CO;2

Brayshaw, D. J., Troccoli, A., Fordham, R., & Methven, J. (2011b). The impact of large scale atmospheric circulation patterns on wind power generation and its potential predictability: A case study over the UK. Renewable Energy, 36(8), 2087–2096. https://doi.org/10.1016/j.renene.2011.01.025

Cabos, W., Sein, D. V., Pinto, J. G., Fink, A. H., Koldunov, N. V., Alvarez, F., Izquierdo, A., Keenlyside, N., & Jacob, D. (2017). The South Atlantic Anticyclone as a key player for the representation of the tropical Atlantic climate in coupled climate models. Climate Dynamics, 48(11–12), 4051–4069. https://doi.org/10.1007/s00382-016-3319-9

Carvalho, D., Rocha, A., Costoya, X., deCastro, M., & Gómez-Gesteira, M. (2021). Wind energy resource over Europe under CMIP6 future climate projections: What changes from CMIP5 to CMIP6. Renewable and Sustainable Energy Reviews, 151, 111594. https://doi.org/10.1016/j.rser.2021.111594

Chen, L. (2020). Impacts of climate change on wind resources over North America based on NA-CORDEX. Renewable Energy, 153, 1428–1438. https://doi.org/10.1016/j.renene.2020.02.090

Cherchi, A., Fogli, P. G., Lovato, T., Peano, D., Iovino, D., Gualdi, S., Masina, S., Scoccimarro, E., Materia, S., Bellucci, A., & Navarra, A. (2019). Global Mean Climate and Main Patterns of Variability in the CMCC-CM2 Coupled Model. Journal of Advances in Modeling Earth Systems, 11(1), 185–209. https://doi.org/10.1029/2018MS001369

Codron, F. (2005). Relation between annular modes and the mean state: southern hemisphere summer. Journal of Climate, 18 (2), 320–330. https://doi.org/10.1175/JCLI-3255.1

Colberg, F., Reason, C. J. C., & Rodgers, K. (2004). South Atlantic response to El Niño-Southern Oscillation induced climate variability in an ocean general circulation model. Journal of Geophysical Research: Oceans, 109(12), 1–14. https://doi.org/10.1029/2004JC002301

Correia, J. M., Bastos, A., Brito, M. C., & Trigo, R. M. (2017). The influence of the main large-scale circulation patterns on wind power production in Portugal. Renewable Energy, 102, 214–223. https://doi.org/10.1016/j.renene.2016.10.002

Cradden, L. C., McDermott, F., Zubiate, L., Sweeney, C., & O'Malley, M. (2017). A 34-year simulation of wind generation potential for Ireland and the impact of large-scale atmospheric pressure patterns. Renewable Energy, 106, 165–176. https://doi.org/10.1016/j.renene.2016.12.079

Dalton, A., Bekker, B., & Koivisto, M. J. (2021). Simulation and detection of wind power ramps and identification of their causative atmospheric circulation patterns. Electric Power Systems Research, 192. https://doi.org/10.1016/j.epsr.2020.106936

Davy, R., Gnatiuk, N., Pettersson, L., & Bobylev, L. (2018). Climate change impacts on wind energy potential in the European domain with a focus on the Black Sea. Renewable and Sustainable Energy Reviews, 81, 1652–1659. https://doi.org/10.1016/j.rser.2017.05.253

De Araujo Lima, L., & Bezerra Filho, C. R. (2010). Wind energy assessment and wind farm simulation in Triunfo – Pernambuco, Brazil. Renewable Energy, 35(12), 2705–2713. https://doi.org/10.1016/j.renene.2010.04.019

De Jong, P., Barreto, T. B., Tanajura, C. A. S., Kouloukoui, D., Oliveira-Esquerre, K. P., Kiperstok, A., & Torres, E. A. (2019). Estimating the impact of climate change on wind and solar energy in Brazil using a South American regional climate model. Renewable Energy, 141, 390–401. https://doi.org/10.1016/j.renene.2019.03.086

De Souza Ferreira, G. W., Reboita, M. S., Ribeiro, J. G. M., Carvalho, V. S. B., Santiago, M. E. V., Silva, P. L. L. S., Baldoni, T. C., & De Souza, C. A. (2024). Assessment of the wind power density over South America simulated by CMIP6 models in the present and future climate. Climate Dynamics, 62(3), 1729–1763. https://doi.org/10.1007/s00382-023-06993-3

Deng, K., Azorin-Molina, C., Yang, S., Hu, C., Zhang, G., Minola, L., & Chen, D. (2022). Changes of Southern Hemisphere westerlies in the future warming climate. Atmospheric Research, 270, 106040. https://doi.org/10.1016/j.atmosres.2022.106040

Devis, A., Van Lipzig, N. P. M., & Demuzere, M. (2018). Should future wind speed changes be taken into account in wind farm development? Environmental Research Letters, 13(6), 064012. https://doi.org/10.1088/1748-9326/aabff7

Doddy Clarke, E., Sweeney, C., McDermott, F., Griffin, S., Correia, J. M., Nolan, P., & Cooke, L. (2022). Climate change impacts on wind energy generation in Ireland. Wind Energy, 25(2), 300–312. https://doi.org/10.1002/we.2673

Emodi, N. V., Chaiechi, T., & Beg, A. B. M. R. A. (2019). The impact of climate variability and change on the energy system: A systematic scoping review. Science of The Total Environment, 676, 545–563. https://doi.org/10.1016/j.scitotenv.2019.04.294

Esnaola, G., Ulazia, A., Sáenz, J., & Ibarra-Berastegi, G. (2024). Future changes of global Annual and Seasonal Wind-Energy Production in CMIP6 projections considering air density variation. Energy, 307, 132706. https://doi.org/10.1016/j.energy.2024.132706

Farjami, H., & Hesari, A. R. E. (2020). Assessment of sea surface wind field pattern over the Caspian Sea using EOF analysis. Regional Studies in Marine Science, 35. https://doi.org/10.1016/j.rsma.2020.101254

Feng, S., Wang, W., Wang, Z., Song, Z., Yang, Q., & Wang, B. (2024). Global Wind-Power Generation Capacity in the Context of Climate Change. Engineering, S2095809924005873. https://doi.org/10.1016/j.eng.2024.09.018

Filgueiras, A., & Silva, T. M. V. e. (2003). Wind energy in Brazil—Present and future. Renewable and Sustainable Energy Reviews, 7(5), 439–451. https://doi.org/10.1016/S1364-0321(03)00068-6

Foley, A. M., Leahy, P. G., Marvuglia, A., & McKeogh, E. J. (2012). Current methods and advances in forecasting of wind power generation. Renewable Energy, 37(1), 1–8. https://doi.org/10.1016/j.renene.2011.05.033

Fredriksen, H. B., Berner, J., Subramanian, A. C., & Capotondi, A. (2020). How Does El Niño–Southern Oscillation Change Under Global Warming—A First Look at CMIP6. Geophysical Research Letters, 47(22). https://doi.org/10.1029/2020GL090640

Ganea, D., Mereuta, E., & Rusu, L. (2018). Estimation of the Near Future Wind Power Potential in the Black Sea. Energies, 11(11), 3198. https://doi.org/10.3390/en11113198

Gao, Y., Ma, S., & Wang, T. (2019). The impact of climate change on wind power abundance and variability in China. Energy, 189, 116215. https://doi.org/10.1016/j.energy.2019.116215

Garreaud, R. D., Vuille, M., Compagnucci, R., & Marengo, J. (2009). Present-day South American climate. Palaeogeography, Palaeoclimatology, Palaeoecology, 281(3–4), 180–195. https://doi.org/10.1016/j.palaeo.2007.10.032

Garrido-Perez, J. M., Ordóñez, C., Barriopedro, D., García-Herrera, R., & Paredes, D. (2020). Impact of weather regimes on wind power variability in western Europe. Applied Energy, 264. https://doi.org/10.1016/j.apenergy.2020.114731

Gómez-Fontealba, C., Flores-Aqueveque, V., & Alfaro, S. C. (2022). Variability of the Southwestern Patagonia (51°S) Winds in the Recent (1980–2020) Period: Implications for Past Wind Reconstructions. Atmosphere, 13(2). https://doi.org/10.3390/atmos13020206

Greene, C. A., Thirumalai, K., Kearney, K. A., Delgado, J. M., Schwanghart, W., Wolfenbarger, N. S., Thyng, K. M., Gwyther, D. E., Gardner, A. S., & Blankenship, D. D. (2019). The Climate Data Toolbox for MATLAB. Geochemistry, Geophysics, Geosystems, 20(7), 3774–3781. https://doi.org/10.1029/2019GC008392

Gugliani, G. K., Sarkar, A., Ley, C., & Matsagar, V. (2021). Identification of optimum wind turbine parameters for varying wind climates using a novel month-based turbine performance index. Renewable Energy, 171, 902–914. https://doi.org/10.1016/j.renene.2021.02.141

Hajima, T., Watanabe, M., Yamamoto, A., Tatebe, H., Noguchi, M. A., Abe, M., Ohgaito, R., Ito, A., Yamazaki, D., Okajima, H., Ito, A., Takata, K., Ogochi, K., Watanabe, S., & Kawamiya, M. (2020). Development of the MIROC-ES2L Earth system model and the evaluation of biogeochemical processes and feedbacks. Geoscientific Model Development, 13(5), 2197–2244. https://doi.org/10.5194/gmd-13-2197-2020

Hayes, L., Stocks, M., & Blakers, A. (2021). Accurate long-term power generation model for offshore wind farms in Europe using ERA5 reanalysis. Energy, 229. https://doi.org/10.1016/j.energy.2021.120603

He, B., Yu, Y., Bao, Q., Lin, P., Liu, H., Li, J., Wang, L., Liu, Y., Wu, G., Chen, K., Guo, Y., Zhao, S., Zhang, X., Song, M., & Xie, J. (2020). CAS FGOALS-f3-L model dataset descriptions for CMIP6 DECK experiments. Atmospheric and Oceanic Science Letters, 13(6), 582–588. https://doi.org/10.1080/16742834.2020.1778419

Hou, M. & Tang, Y. (2022). Recent progress in simulating two types of ENSO – from CMIP5 to CMIP6. Frontiers in Marine Science, 9:986780. https://doi.org/10.3389/fmars.2022.986780

IRENA (2023), Renewable capacity statistics 2023, International Renewable Energy Agency, Abu Dhabi. ISBN: 978-92-9260-525-4

IRENA. (2025). Renewable capacity statistics 2025. International Renewable Energy Agency.

Islek, F., Yuksel, Y., & Sahin, C. (2020). Spatiotemporal long-term trends of extreme wind characteristics over the Black Sea. Dynamics of Atmospheres and Oceans, 90, 101132. https://doi.org/10.1016/j.dynatmoce.2020.101132

Jung, C., & Schindler, D. (2020). Introducing a new approach for wind energy potential assessment under climate change at the wind turbine scale. Energy Conversion and Management, 225. https://doi.org/10.1016/j.enconman.2020.113425

Jung, C., & Schindler, D. (2022). A review of recent studies on wind resource projections under climate change. Renewable and Sustainable Energy Reviews, 165, 112596. https://doi.org/10.1016/j.rser.2022.112596

Karnauskas, K. B., Lundquist, J. K., & Zhang, L. (2018). Southward shift of the global wind energy resource under high carbon dioxide emissions. Nature Geoscience, 11(1), 38–43. https://doi.org/10.1038/s41561-017-0029-9

Khasanzoda, N., Zicmane, I., Beryozkina, S., Safaraliev, M., Sultonov, S., & Kirgizov, A. (2022). Regression model for predicting the speed of wind flows for energy needs based on fuzzy logic. Renewable Energy, 191, 723-731. https://doi.org/10.1016/j.renene.2022.04.017

Kim, D.Y., Kim, Y. H., & Kim, B. S. (2021). Changes in wind turbine power characteristics and annual energy production due to atmospheric stability, turbulence intensity, and wind shear. Energy, 214, 119051. https://doi.org/10.1016/j.energy.2020.119051

Kim, Y. H., Pak, G., Noh, Y., Lee, M.-I., Yeh, S.-W., Kim, D., Kim, S.-Y., Lee, J.-L., Lee, H. J., Hyun, S.-H., Lee, K.-Y., & Lee, J.-H. (2020, March 23). Korea Institute of Ocean Science & Technology Earth System Model and its simulation characteristics. https://doi.org/10.5194/egusphere-egu2020-12907

Koletsis, I., Kotroni, V., Lagouvardos, K., & Soukissian, T. (2016). Assessment of offshore wind speed and power potential over the Mediterranean and the Black Seas under future climate changes. In Renewable and Sustainable Energy Reviews (Vol. 60, pp. 234–245). Elsevier Ltd. https://doi.org/10.1016/j.rser.2016.01.080

Li, X., Li, Q. P., Ding, Y. H., & Wang, M. (2022). Near-surface wind speed changes in eastern China during 1970–2019 winter and its possible causes. Advances in Climate Change Research, 13(2), 228–239. https://doi.org/10.1016/j.accre.2022.01.003

Liao, H., Wang, C., & Song, Z. (2021). ENSO phase-locking biases from the CMIP5 to CMIP6 models and a possible explanation. Deep-Sea Research Part II: Topical Studies in Oceanography, 189–190. https://doi.org/10.1016/j.dsr2.2021.104943

Llompart, O., Sepúlveda, H. H., Jacques-Coper, M., & Hernández, M. (2025). Evaluating Wind Speed Variability and Its Climate Modulators in South America Using CMIP6 Simulations (1980–2014). International Journal of Climatology, e8921. https://doi.org/10.1002/joc.8921

Lovato, T., Peano, D., Butenschön, M., Materia, S., Iovino, D., Scoccimarro, E., Fogli, P. G., Cherchi, A., Bellucci, A., Gualdi, S., Masina, S., & Navarra, A. (2022). CMIP6 Simulations With the CMCC Earth System Model (CMCC-ESM2). Journal of Advances in Modeling Earth Systems, 14(3), e2021MS002814. https://doi.org/10.1029/2021MS002814

Lübbecke, J. F., Burls, N. J., Reason, C. J. C., & Mcphaden, M. J. (2014). Variability in the South Atlantic anticyclone and the Atlantic Niño mode. Journal of Climate, 27(21), 8135–8150. https://doi.org/10.1175/JCLI-D-14-00202.1

Manwell, J. F., McGowan, J. G., & Rogers, A. L. (2010). Wind Energy Explained: Theory, Design and Application. John Wiley & Sons Ltd, The Atrium, Southern Gate, Chichester, West Sussex, PO19 8SQ, United Kingdom, 2010. ISBN 978-0-470-01500-1 (Hbk)

Marshall, G. J. (2003). Trends in the Southern Annular Mode from Observations and Reanalyses. Journal of Climate, 16(24), 4134–4143. https://doi.org/10.1175/1520-0442(2003)016<4134:TITSAM>2.0.CO;2

Martinez, A., & Iglesias, G. (2021). Wind resource evolution in Europe under different scenarios of climate change characterised by the novel Shared Socioeconomic Pathways. Energy Conversion and Management, 234, 113961. https://doi.org/10.1016/j.enconman.2021.113961

Martinez, A., & Iglesias, G. (2024). Climate change and wind energy potential in South America. Science of The Total Environment, 957, 177675. https://doi.org/10.1016/j.scitotenv.2024.177675

Mattar, C., & Borvarán, D. (2016). Offshore wind power simulation by using WRF in the central coast of Chile. Renewable Energy, 94, 22–31. https://doi.org/10.1016/j.renene.2016.03.005

Mattar, C., & Guzmán-Ibarra, M. C. (2017). A techno-economic assessment of offshore wind energy in Chile. Energy, 133, 191–205. https://doi.org/10.1016/j.energy.2017.05.099

Mattar, C., Cabello-Españon, F., & Alonso-de-Linaje, N. G. (2021). Towards a Future Scenario for Offshore Wind Energy in Chile: Breaking the Paradigm. Sustainability, 13(13), 7013. https://doi.org/10.3390/su13137013

Mendoza, V. M., Oda, B., Garduño, R., Villanueva, E. E., & Adem, J. (2014). Simulation of the PDO effect on the North America summer climate with emphasis on Mexico. Atmospheric Research, 137, 228–244. https://doi.org/10.1016/j.atmosres.2013.10.010

Mitchell, T. P., & Wallace, J. M. (1996). ENSO Seasonality: 1950–78 versus 1979–92. Journal of Climate, 9 (12), 3149–3161. https://doi.org/10.1175/1520-0442(1996)009<3149:ESV>2.0.CO;2

Miyasaka, T., & Nakamura, H. (2010). Structure and mechanisms of the Southern Hemisphere summertime subtropical anticyclones. Journal of Climate, 23(8), 2115–2130. https://doi.org/10.1175/2009JCLI3008.1

Moemken, J., Reyers, M., Feldmann, H., & Pinto, J. G. (2018). Future Changes of Wind Speed and Wind Energy Potentials in EURO-CORDEX Ensemble Simulations. Journal of Geophysical Research: Atmospheres, 123(12), 6373–6389. https://doi.org/10.1029/2018JD028473

Mortensen, E., Wu, S., Notaro, M., Vavrus, S., Montgomery, R., De Piérola J., Sánchez, C. & Block, P. (2018). Regression-based season-ahead drought prediction for southern Peru conditioned on large-scale climate variables. Hydrology and Earth System Sciences, 22, 287–303. https://doi.org/10.5194/hess-22-287-2018

Mulcahy, J. P., Jones, C. G., Rumbold, S. T., Kuhlbrodt, T., Dittus, A. J., Blockley, E. W., Yool, A., Walton, J., Hardacre, C., Andrews, T., Bodas-Salcedo, A., Stringer, M., De Mora, L., Harris, P., Hill, R., Kelley, D., Robertson, E., & Tang, Y. (2023). UKESM1.1: Development and evaluation of an updated configuration of the UK Earth System Model. Geoscientific Model Development, 16(6), 1569–1600. https://doi.org/10.5194/gmd-16-1569-2023

Neelin, J. D., Jin F. F., & Syu, H. H. (2000). Variations in ENSO Phase Locking. Journal of Climate, 13 (14), 2570–2590. https://doi.org/10.1175/1520-0442(2000)013<2570:VIEPL>2.0.CO;2

Ohba, M., Kadokura, S., & Nohara, D. (2016). Impacts of synoptic circulation patterns on wind power ramp events in East Japan. Renewable Energy, 96, 591–602. https://doi.org/10.1016/j.renene.2016.05.032

Olauson, J. (2018). ERA5: The new champion of wind power modelling? Renewable Energy, 126, 322–331. https://doi.org/10.1016/j.renene.2018.03.056

Patel, R. P., Nagababu, G., Kachhwaha, S. S., & Surisetty, V. V. A. K. (2022). A revised offshore wind resource assessment and site selection along the Indian coast using ERA5 near-hub-height wind products. Ocean Engineering, 254. https://doi.org/10.1016/j.oceaneng.2022.111341

Peiris, A. T., Jayasinghe, J., & Rathnayake, U. (2021). Forecasting Wind Power Generation Using Artificial Neural Network: "Pawan Danawi"—A Case Study from Sri Lanka. Journal of Electrical and Computer Engineering, 2021, 1–10. https://doi.org/10.1155/2021/5577547

Qian, H., & Zhang, R. (2021). Future changes in wind energy resource over the Northwest Passage based on the CMIP6 climate projections. International Journal of Energy Research, 45(1), 920–937. https://doi.org/10.1002/er.5997

Ravestein, P., van der Schrier, G., Haarsma, R., Scheele, R., & van den Broek, M. (2018). Vulnerability of European intermittent renewable energy supply to climate change and climate variability. Renewable and Sustainable Energy Reviews, 97, 497–508. https://doi.org/10.1016/j.rser.2018.08.057

Rodwell, M. J., & Hoskins, B. J. (2001). Subtropical anticyclones and summer monsoons. Journal of Climate, 14(15), 3192–3211. https://doi.org/10.1175/1520-0442(2001)014<3192:SAASM>2.0.CO;2

Russo, M. A., Carvalho, D., Martins, N., & Monteiro, A. (2023). Future perspectives for wind and solar electricity production under high-resolution climate change scenarios. Journal of Cleaner Production, 404, 136997. https://doi.org/10.1016/j.jclepro.2023.136997

Sakuru, S. K. V. S., & Ramana, M. V. (2023). Wind power potential over India using the ERA5 reanalysis. Sustainable Energy Technologies and Assessments, 56. https://doi.org/10.1016/j.seta.2023.103038

Sawadogo, W., Reboita, M. S., Faye, A., Da Rocha, R. P., Odoulami, R. C., Olusegun, C. F., Adeniyi, M. O., Abiodun, B. J., Sylla, M. B., Diallo, I., Coppola, E., & Giorgi, F. (2021). Current and future potential of solar and wind energy over Africa using the RegCM4 CORDEX-CORE ensemble. Climate Dynamics, 57(5–6), 1647–1672. https://doi.org/10.1007/s00382-020-05377-1

Séférian, R., Nabat, P., Michou, M., Saint-Martin, D., Voldoire, A., Colin, J., Decharme, B., Delire, C., Berthet, S., Chevallier, M., Sénési, S., Franchisteguy, L., Vial, J., Mallet, M., Joetzjer, E., Geoffroy, O., Guérémy, J., Moine, M., Msadek, R., … Madec, G. (2019). Evaluation of CNRM Earth System Model, CNRM-ESM2-1:

Role of Earth System Processes in Present-Day and Future Climate. Journal of Advances in Modeling Earth Systems, 11(12), 4182–4227. https://doi.org/10.1029/2019MS001791

Serykh, I.V., & Sonechkin, D.M. (2024). Global El Niño–Southern Oscillation teleconnections in CMIP6 models. Atmosphere, 15, 500. https:// doi.org/10.3390/atmos15040500

Shadman, M., Roldan-Carvajal, M., Pierart, F. G., Haim, P. A., Alonso, R., Silva, C., Osorio, A. F., Almonacid, N., Carreras, G., Maali Amiri, M., Arango-Aramburo, S., Rosas, M. A., Pelissero, M., Tula, R., Estefen, S. F., Pastor, M. L., & Saavedra, O. R. (2023). A Review of Offshore Renewable Energy in South America: Current Status and Future Perspectives. Sustainability, 15(2), 1740. https://doi.org/10.3390/su15021740

Shin, J.-Y., Jeong, C., & Heo, J.-H. (2018). A Novel Statistical Method to Temporally Downscale Wind Speed Weibull Distribution Using Scaling Property. Energies, 11(3), 633. https://doi.org/10.3390/en11030633

Shiogama, H., Tatebe, H., Hayashi, M., Abe, M., Arai, M., Koyama, H., Imada, Y., Kosaka, Y., Ogura, T., & Watanabe, M. (2023). MIROC6 Large Ensemble (MIROC6-LE): Experimental design and initial analyses. Earth System Dynamics, 14(6), 1107–1124. https://doi.org/10.5194/esd-14-1107-2023

Sinha, M., Jha, S., & Chakraborty, P. (2020). Indian Ocean wind speed variability and global teleconnection patterns. Oceanologia, 62(2), 126–138. https://doi.org/10.1016/j.oceano.2019.10.002

Soares, P. M. M., Lima, D. C. A., Cardoso, R. M., Nascimento, M. L., & Semedo, A. (2017). Western Iberian offshore wind resources: More or less in a global warming climate? Applied Energy, 203, 72–90. https://doi.org/10.1016/j.apenergy.2017.06.004

Solaun, K., & Cerdá, E. (2020). Impacts of climate change on wind energy power – Four wind farms in Spain. Renewable Energy, 145, 1306–1316. https://doi.org/10.1016/j.renene.2019.06.129

Soukissian, T. H., Karathanasi, F. E., & Zaragkas, D. K. (2021). Exploiting offshore wind and solar resources in the Mediterranean using ERA5 reanalysis data. Energy Conversion and Management, 237. https://doi.org/10.1016/j.enconman.2021.114092

Srinivas, G., Vialard, J., Liu, F., Voldoire, A., Izumo, T., Guilyardi, E., & Lengaigne, M. (2024). Dominant contribution of atmospheric nonlinearities to ENSO asymmetry and extreme El Niño events. Scientific Reports, 14, 8122. https://doi.org/10.1038/s41598-024-58803-3

Sterl, A., & Hazeleger, W. (2003). Coupled variability and air-sea interaction in the South Atlantic Ocean. Climate Dynamics, 21(7–8), 559–571. https://doi.org/10.1007/s00382-003-0348-y

Sulca, J., Takahashi, K., Espinoza, J. C., Tacza, J., Zubieta, R., Mosquera, K., & Apaestegui, J. (2024). A multiple linear regression model for the prediction of summer rainfall in the northwestern Peruvian Amazon using large-scale índices. Climate Dynamics, 62, 4431–4451. https://doi.org/10.1007/s00382-023-07044-7

Swart, N. C., Cole, J. N. S., Kharin, V. V., Lazare, M., Scinocca, J. F., Gillett, N. P., Anstey, J., Arora, V., Christian, J. R., Hanna, S., Jiao, Y., Lee, W. G., Majaess, F., Saenko, O. A., Seiler, C., Seinen, C., Shao, A., Sigmond, M., Solheim, L., … Winter, B. (2019). The Canadian Earth System Model version 5 (CanESM5.0.3). Geoscientific Model Development, 12(11), 4823–4873. https://doi.org/10.5194/gmd-12-4823-2019

Thompson, D. W. J., & Wallace, J. M. (2000). Annular modes in the extratropical circulation. Part I: month-to-month variability. Journal of Climate, 13 (5), 1000–1016. https://doi.org/10.1175/1520-0442(2000)013<1000:AMITEC>2.0.CO;2

Tian, Q., Huang, G., Hu, K., & Niyogi, D. (2019). Observed and global climate model based changes in wind power potential over the Northern Hemisphere during 1979–2016. Energy, 167, 1224–1235. https://doi.org/10.1016/j.energy.2018.11.027

Tobin, I., Jerez, S., Vautard, R., Thais, F., Van Meijgaard, E., Prein, A., Déqué, M., Kotlarski, S., Maule, C. F., Nikulin, G., Noël, T., & Teichmann, C. (2016). Climate change impacts on the power generation potential of a European mid-century wind farms scenario. In Environmental Research Letters (Vol. 11, Issue 3). Institute of Physics Publishing. https://doi.org/10.1088/1748-9326/11/3/034013

Tobin, I., Vautard, R., Balog, I., Bréon, F. M., Jerez, S., Ruti, P. M., Thais, F., Vrac, M., & Yiou, P. (2015). Assessing climate change impacts on European wind energy from ENSEMBLES high-resolution climate projections. Climatic Change, 128(1–2), 99–112. https://doi.org/10.1007/s10584-014-1291-0

Vaittinada Ayar, P., Battisti, D. S., Li, C., King, M., Vrac, M., & Tjiputra, J. (2023). A regime view of ENSO flavors through clustering in CMIP6 models. Earth's Future, 11, e2022EF003460. https://doi.org/10.1029/2022EF003460

Voldoire, A., Saint-Martin, D., Sénési, S., Decharme, B., Alias, A., Chevallier, M., Colin, J., Guérémy, J. -F., Michou, M., Moine, M. -P., Nabat, P., Roehrig, R., Salas Y Mélia, D., Séférian, R., Valcke, S., Beau, I., Belamari, S., Berthet, S., Cassou, C., … Waldman, R. (2019). Evaluation of CMIP6 DECK Experiments With CNRM-CM6-1. Journal of Advances in Modeling Earth Systems, 11(7), 2177–2213. https://doi.org/10.1029/2019MS001683

Volodin, E., & Gritsun, A. (2018). Simulation of observed climate changes in 1850–2014 with climate model INM-CM5. Earth System Dynamics, 9(4), 1235–1242. https://doi.org/10.5194/esd-9-1235-2018

Wang, K., Wu, D., Zhang, T., Yin, L., Wu, K., & Zheng, C. (2024). Spatial distribution and long-term trend of wind energy in the Northwest Pacific Ocean. Water-Energy Nexus. https://doi.org/10.1016/j.wen.2023.11.005

Watts, D., Durán, P., & Flores, Y. (2017). How does El Niño Southern Oscillation impact the wind resource in Chile? A techno-economical assessment of the influence of El Niño and La Niña on the wind power. Renewable Energy, 103, 128–142. https://doi.org/10.1016/j.renene.2016.10.031

Weber, J., Gotzens, F., & Witthaut, D. (2018). Impact of strong climate change on the statistics of wind power generation in Europe. Energy Procedia, 153, 22–28. https://doi.org/10.1016/j.egypro.2018.10.004

Wilkie, D., & Galasso, C. (2020). Impact of climate-change scenarios on offshore wind turbine structural performance. Renewable and Sustainable Energy Reviews, 134, 110323. https://doi.org/10.1016/j.rser.2020.110323

Wilks, D. S. (2006). Statistical methods in the atmospheric sciences, Second Edition (pp. 394–397). Volume 91 in the International Geophysics Series. Elsevier Inc. 30 Corporate Drive, Suite 400, Burlington, MA 01803, USA. ISBN 13: 978-0-12-751966-1, ISBN 10: 0-12-751966-1

Wu, J., Shi, Y., & Xu, Y. (2020). Evaluation and Projection of Surface Wind Speed Over China Based on CMIP6 GCMs. Journal of Geophysical Research: Atmospheres, 125(22). https://doi.org/10.1029/2020JD033611

Zhang, D., Xu, Z., Li, C., Yang, R., Shahidehpour, M., Wu, Q., & Yan, M. (2019). Economic and sustainability promises of wind energy considering the impacts of climate change and vulnerabilities to extreme conditions. The Electricity Journal, 32(6), 7–12. https://doi.org/10.1016/j.tej.2019.05.013

Zhou, F., Zhao, Z., Azorin-Molina, C., Jia, X., Zhang, G., Chen, D., Liu, J., Guijarro, J. A., Zhang, F., & Fang, K. (2022). Teleconnections between large-scale oceanic-atmospheric patterns and interannual surface wind speed variability across China: Regional and seasonal patterns. Science of the Total Environment, 838. https://doi.org/10.1016/j.scitotenv.2022.156023